THE HENRYK NIEWODNICZAŃSKI
INSTITUTE OF NUCLEAR PHYSICS
POLISH ACADEMY OF SCIENCES

Università
degli Studi
di Ferrara

Copernicus International Doctorate

The Henryk Niewodniczański Institute of Nuclear Physics
Polish Academy of Sciences
and
The University of Ferrara

Search for the $\Lambda_c^+ \to p\mu^+\mu^-$ Decay at the LHCb Experiment

Maciej Dudek

Supervisor
prof. dr hab. Mariusz Witek

Auxiliary supervisor
dr Jolanta Brodzicka

Supervisor
prof. Roberto Calabrese

Auxiliary supervisor
prof. Eleonora Luppi

A thesis presented for the degree of
Doctor of Philosophy in Physics

Kraków, June 2023

Acknowledgments

I would like to sincerely thank all the people without whom the preparation of the following thesis would not have been possible. In particular, I would like to thank:

My supervisor from the IFJ PAN Prof. dr hab. Mariusz Witek, for his support throughout the course of my studies and guidance in writing my thesis. I would also like to thank my auxiliary supervisor Dr Jolanta Brodzicka and Dr hab. Marcin Chrząszcz for their help and advices.

My supervisor from the University of Ferrara Prof. Roberto Calabrese and my auxiliary supervisor Prof. Eleonora Luppi for their assistance and kindness.

The LHCb group at Cern for the opportunity to work with you and for your insight during the course of my analysis.

Last but not least, I would like to thank my family for their constant support and love.

Abstract

The main goal of this PhD thesis is to search for new physics in the rare baryon decay $\Lambda_c^+ \to p\mu^+\mu^-$. Charm hadrons are abundantly produced by the LHC accelerator in proton-proton collisions and their decay products are recorded by the LHCb detector. The analysis was carried out for data collected in the Run2 phase in the years 2016-2018 at the center of mass energy of 13 TeV. The decay of $\Lambda_c^+ \to p\mu^+\mu^-$ is strongly suppressed as it occurs through FCNC (Flavour-Changing Neutral Currents) processes. This creates the potential for observing small effects from processes beyond the Standard Model that may cause differences in predicted and observed decay rates or angular distributions of decay products.

In this thesis, an analysis of two ranges of the invariant mass of the muon system $m(\mu^+\mu^-)$ was performed. The region of the signal corresponding to a decay in short-distance processes included the ranges $m_{\mu^+\mu^-} < 507.86$ MeV/c^2 and $m_{\mu^+\mu^-} > 1059.45$ MeV/c^2. The region of long-distance decays involving resonances was divided into ranges including η, ρ, ω and ϕ. The resonant decay $\Lambda_c^+ \to p\phi(\mu^+\mu^-)$ served as both a normalization and control channel. The same final state for the signal and the normalization channel ensured the cancellation of many systematic effects. The results on the upper limit of the signal decay and the decay ratios of the resonant channels with respect to the normalization channel are presented. In the upper range of the signal $m_{\mu^+\mu^-} > 1059.45$ MeV/c^2 the statistical significance exceeded two standard deviations. Interpretation of this result other than the occurrence of statistical fluctuation would require collecting more events and performing an angular analysis. In the resonant region, the decay of $\Lambda_c^+ \to p\rho(\mu^+\mu^-)$ was observed for the first time and its branching ratio was measured.

Streszczenie

Głównym celem niniejszej pracy doktorskiej jest poszukiwanie nowej fizyki w rzadkim rozpadzie barionu $\Lambda_c^+ \to p\mu^+\mu^-$. Hadrony powabne są obficie produkowane przez akcelerator LHC w zderzeniach proton-proton a ich produkty rozpadu są następnie rejestrowane przez detektor LHCb. Analiza przeprowadzona została dla danych zebranych w fazie Run2 w latach 2016-2018 przy energii w środku masy 13 TeV. Rozpad $\Lambda_c^+ \to p\mu^+\mu^-$ jest silnie tłumiony gdyż zachodzi poprzez procesy FCNC (Flavour-Changing Neutral Currents). Stwarza to potencjał dla obserwacji niewielkich efektów od procesow spoza Modelu Standardowego, ktore moga spowodować różnice przewidywanych i zaobserwowanych czestości rozpadu lub rozkladow katowych produktow rozpadu.

W pracy przeprowadzono analize dwóch zakresów masy inwariantnej systemu mionów $m(\mu^+\mu^-)$. Obszar sygnału odpowiadający rozpadowi w procesach krótko-zasiegowych obejmował zakresy $m_{\mu^+\mu^-} < 507.86$ MeV/c^2 i $m_{\mu^+\mu^-} > 1059.45$ MeV/c^2. Obszar rozpadów długo-zasięgowych z udziałem rezonansów podzielony został na zakresy obejmujące η, ρ, ω i ϕ. Rozpad rezonansowy $\Lambda_c^+ \to p\phi(\mu^+\mu^-)$ posłużył jako kanał jednocześnie normalizacyjny i kontrolny. Ten sam stan końcowy dla sygnału i kanału normalizacyjnego zapewnił znoszenie się wielu efektów systematycznych. Przedstawiono wyniki na górną granice rozpadu sygnałowego oraz na stosunki rozpadu kanałow rezonansowych względem kanału normalizacyjnego. W górnym zakresie sygnału $m_{\mu^+\mu^-} > 1059.45$ MeV/c^2 znaczącość statystyczna przekroczyła dwa odchylenia standardowe. Interpretacja tego wyniku różna od zajscia fluktuacji statystycznej wymagałaby zebrania większej liczby przypadków i przeprowadzenia analizy kątowej. W obszarze rezonansowym zaobserwowano po raz pierwszy rozpad $\Lambda_c^+ \to p\rho(\mu^+\mu^-)$ i zmierzono jego rozgałęzienie rozpadu.

Contents

Acronyms

AUC Area Under the Curve

BDT Boosted Decision Tree
BF Branching Fraction
BKGCAT Background Category
BR Branching Ratio

CB Crystal Ball
CERN European Organisation for Nuclear Research
CKM Cabibbo-Kobayashi-Maskawa
CLs Confidence Level on Signal

DST Data Summary Tape

ECAL Electromagnetic Calorimeter

FCNC Flavour-Changing Neutral Currents
FOM Figure of Merit

GIM Glashow-Iliopulus-Maiani

HCAL Hadronic Calorimeter
HLT High Level Trigger

IT Inner Tracker

L0 Level-0
LHC Large Hadron Collider
LHCb Large Hadron Collider beauty

MC Monte Carlo
MVA Multivariate Analysis

NP New Physics

OT Outer Tracker

PDF Probability Density Function
PID Particle Identification
PV Primary Vertex

QCD Quantum chromodynamics
QFT Quantum Field Theory

RICH Ring Imaging Cherenkov
ROC Receiver Operating Characteristic

SM Standard Model
SPD Scintillating Pad Detector
ST Silicon Tracker

TT Trigger Tracker

UL Upper Limit

VELO VErtex LOcator

1 Introduction

The Standard Model [1–3] was formulated in the sixties of the last century to describe the fundamental particles and their interactions. Except for the observation of non-zero neutrino masses and the resulting phenomenon of neutrino oscillations, all existing laboratory measurements agree with the predictions of the Standard Model within the uncertainty of experimental measurements. The observation of the Higgs boson [4, 5] in 2012 by the ATLAS and CMS experiments carried out at CERN was the final confirmation of its great success. However, there are observations indicating that the Standard Model is only an effective theory at the scale of the currently available collision energy. Some astrophysical and laboratory observations (dark matter, the domination of matter over antimatter in the Universe, non-zero mass of neutrinos) cannot be explained. Many new theories have been proposed to extend the SM, introducing the so-called New Physics phenomena. Most of them predict the existence of new heavy particles that would solve the experimental and theoretical problems of the SM. The measured mass of the Higgs boson and the direct search for the production of particles from outside the Standard Model on the LHC collider suggest that the direct energy scale of observation of New Physics particles is much higher than expected. For this reason, the importance of indirect measurements, such as those carried out in the LHCb experiment, has increased significantly. Precise indirect measurements allow one to search for effects from particles with masses significantly exceeding the available energy in proton-proton collisions at the LHC. These hypothetical phenomena are expected to be very rare and therefore extremely difficult to observe in the predominant background of already known processes.

Charm physics provides an opportunity for a unique test of the SM. Rare charm processes are complementary to the ones in strange and beauty sectors. One of such decays is $\Lambda_c^+ \to p\mu^+\mu^-$ [1], the analysis of which is the subject of this thesis. The observation of such rare decays require sophisticated machinery, such as accelerators. The world's largest accelerator is the Large Hadron Collider (LHC) [6] located at CERN. One of the main experiments operating there is the Large Hadron Collider beauty (LHCb) experiment. The LHCb experiment designed its detector to study CP violation phenomena and to search for NP in charm and bottom hadron decays. The LHC accelerator operated during 2011 and 2012 (Run 1), while the second data taking period took place between 2015 and 2018 (Run 2). The analysis in this thesis is based on data collected by LHCb detector during Run 2 period.

Chapters 2 and 3 contain a brief introduction into the theory and LHCb experiment. The next part of this thesis describes the subsequent stages of the analysis. A brief explanation of the analysis strategy is presented in Chapter 4 and the details of the event selection are described in Chapter 5. The following Chapters 6 to 9 explain corrections applied to the simulation samples, study of the background and systematic uncertainties. The final results are presented in Chapter 10.

[1] Inclusion of charge-conjugated modes is implied unless explicitly stated.

2 Theory overview

2.1 The Standard Model of Particle Physics

Throughout the history of physics, there have been numerous attempts to unify seemingly disparate theories and concepts. One such example is the unification of magnetic and electric forces into a single unified force of electromagnetism [7, 8]. This theory was first proposed by James Clerk Maxwell in the 19th century, and has since been shown to be a fundamental aspect of the natural world.

In the 20th century, physicists continued to seek a grand unified theory that would unite all of the known forces of the universe. One of the most successful examples of this effort is the Standard Model, which unifies the electromagnetic force with the weak force. This unification is known as the electroweak theory and was formulated in the present form by Sheldon Glashow, Abdus Salam, and Steven Weinberg in the 1970s [9]. The Standard Model has since become a cornerstone of modern physics, providing a comprehensive framework for understanding the behavior of subatomic particles and their interactions. These elementary particles can be divided into two general groups: fermions and bosons [10] (Fig. 1) .

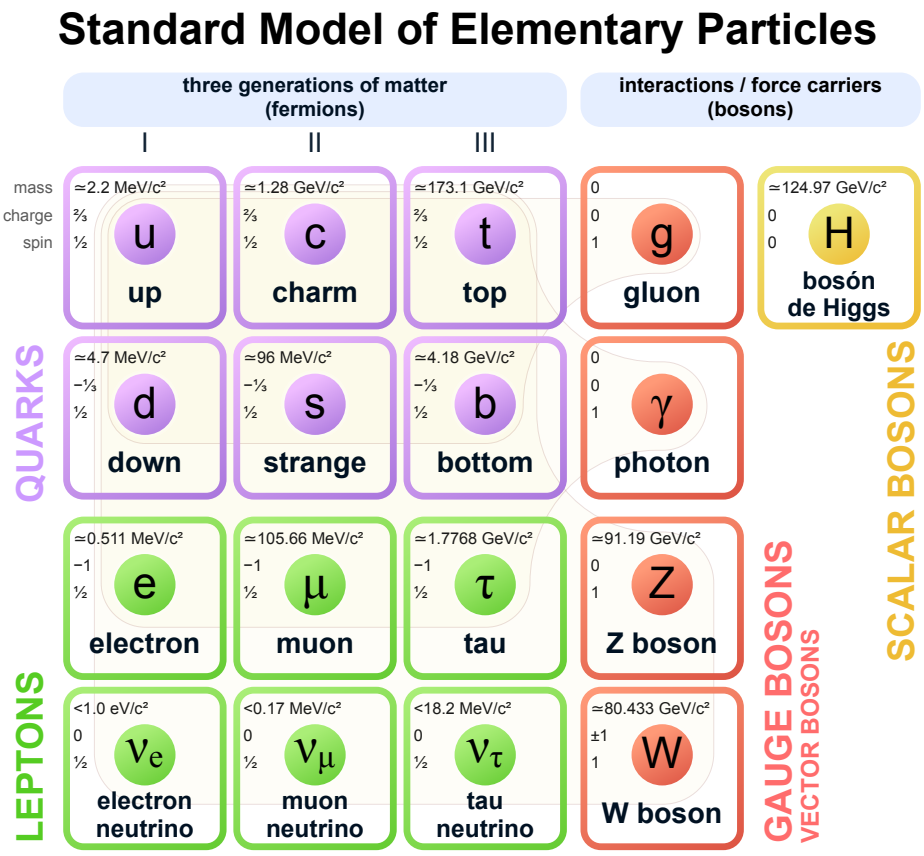

Figure 1: Overview of Elementary particles in SM.

Fermions can be simply described as the elementary constituents of matter. Each of them has 1/2 spin and has its own antiparticle. Fermions are divided in two subgroups: quarks and leptons, each group consisting of 6 particles. Both groups are arranged in three generations each having a pair of quarks, lepton and its neutrino. The quarks names are: *up, down, charm, strange, top* and *bottom* (u, d, c, s, t, b). They carry electrical charge; u, c, t

have +2/3 and d, s, t -1/3 of elementary charge and can interact via electromagnetic and weak forces. Additionally, quarks possess color charge (red, blue and green) allowing them to interact via strong force. They do not appear as free particles and instead form hadrons, e.g. a proton (u, u, d). Leptons consist of an electron, muon, tau and their corresponding neutrinos (e,ν_e,μ,ν_μ,τ,ν_τ). The electron, muon and tau have electrical charge of -1. Neutrinos are neutral and can interact via weak force only.

Fundamental bosons have an integer spin quantum number where four out of five form a gauge boson group. Gauge bosons in the SM are described as force carriers, that are exchanged between fermions. Electromagnetic force is carried by a massless and neutral photon (γ), strong force is carried by massless and color charged gluons (g) and weak force is carried by massive $W^{\pm}$ and Z^0 bosons. The only scalar (spin 0) is the Higgs boson which is the latest discovered fundamental particle. By interacting with the Higgs field [11, 12], massless gauge bosons acquire mass via a spontaneous symmetry breaking mechanism. Fermions get their masses from Yukawa-interactions with the Higgs field after the symmetry breaking.

The SM is mathematically formulated in the form of quantum field gauge theory (QFT) [13] that combines special relativity and quantum mechanics. Its structure is based on $SU(3)_C \times SU(2)_L \times U(1)_Y$ group, where symmetries of strong interactions are described by $SU(3)_C$ (C - color charge) that consist of 8 gauge bosons (gluons) and electroweak interactions are described by $SU(2)_L \times U(1)_Y$ (L - left handed doublets, Y - weak hypercharge). Fields plays fundamental role in QFT, where each of the fermions and also the Higgs boson has its own field. Lagrangian formalism describes the dynamics of these fields as well as quantum states that they act on. The general form of SM Lagrangian is given by the following formula:

$$L_{SM} = L_{QCD} + L_{EW} + L_{YU} + L_H \tag{1}$$

where L_{QCD} is QCD Lagrangian that describes the interaction of color charged particles, L_{EW} is electroweak part related to leptons and quarks and their interactions, L_{YU} describes Yukawa interaction determining fermion masses and the last term L_H is the Higgs part that provides a mechanism to generate masses of fundamental gauge bosons. The details of the SM formalism can be found in [14, 15].

Despite its many successes, the Standard Model remains incomplete, and physicists continue to work towards a more complete theory. The main arguments indicating that SM has to be extended are the following:

- Incomplete description of gravity. The Standard Model does not incorporate the gravitational force, which is described by Einstein's theory of general relativity. This makes it an incomplete description of the universe, as it cannot explain the behavior of objects on a large scale.

- Dark matter and dark energy. The Standard Model cannot explain the existence of dark matter and dark energy, which are thought to make up a significant fraction of the universe's total mass-energy. These components of the universe do not interact with the electromagnetic, strong and weak forces, and are therefore not accounted for in the Standard Model.

- Neutrino mass [16, 17]. The Standard Model originally assumed that neutrinos were massless particles, but experimental evidence has shown that they do in fact have a small mass. The mechanism for generating these masses is not fully understood within the framework of the Standard Model.

- CP violation [18]. The Standard Model predicts a small amount of CP (charge-parity) violation in the behavior of certain particles, but this amount is not sufficient to explain the observed imbalance between matter and antimatter in the universe. This is known as the CP problem.

- Hierarchy problem. The Standard Model predicts that the Higgs boson, which gives particles mass, should have a much larger mass than is observed. This is known as the hierarchy problem.

2.2 Quantum chromodynamics

Quantum chromodynamics (QCD) [19,20] describes strong interactions between particles with color charge. It is based on a gauge symmetry group SU(3) [21, 22]. There are three color charges: red, blue and green, and their anti variants. The total color charge for hadrons has to be neutral (white in analogy to visible light). Each of the three quarks forming baryons has to have a different color. In the case of mesons it simply can occur in a pair of quark and antiquark of its corresponding color. A gluon is the carrier strong force with its own color charge. Gluons can carry one color charge and one anti-color charge. With all this combinations they form a color octet.

One of the properties of QCD is color confinement. It explains why quarks and gluons are never observed in isolation. As the force between two color charged particles is increasing with distance they stay grouped as hadrons until enough energy is produced to turn one hadron into a pair of new hadrons instead of producing free quarks (Fig. 2). This process is called hadronization and the only exception to it is *top* quark that decays faster than it can hadronize.

Another property of QCD is asymptotic freedom. Asymptotic freedom refers to the fact that the strong force between quarks and gluons becomes weaker at high energies and short distances. In other words, as quarks and gluons are brought closer together, they become less strongly bound to each other, and the force between them becomes weaker. This is the opposite of what happens with the electromagnetic force, which becomes stronger at shorter distances.

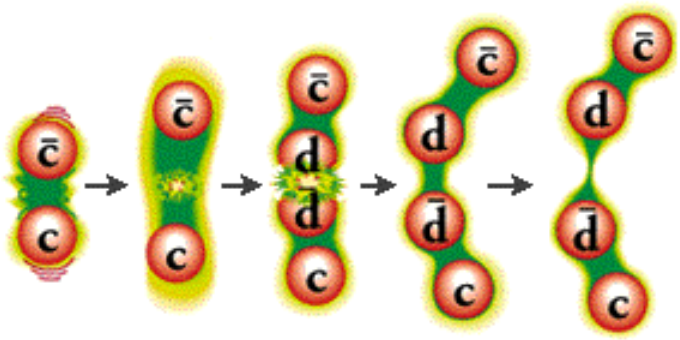

Figure 2: The illustration of quark pair transition into two new quark pairs.

2.3 Flavor Physics

Flavor is a property assigned to leptons and quarks as one of their quantum number. In the SM there are six flavors for leptons and six flavors for quarks. The quarks can change its flavor via weak interactions using a $W^{\pm}$ boson as a carrier in its exchange. The result of this is that the up-type quark changes into down-type state and vice-versa. The strength of transitions is governed by the CKM matrix [23, 24] which defines the amplitude of transitions between quark flavors. The CKM matrix is 3×3 matrix that contains 9 elements that represent transition between the quarks:

$$V_{CKM} \equiv V_L^u V_L^\dagger = \begin{bmatrix} V_{ud} & V_{us} & V_{ub} \\ V_{cd} & V_{cs} & V_{cb} \\ V_{td} & V_{ts} & V_{tb} \end{bmatrix} \tag{2}$$

This unitary matrix can be parametrized using 3 mixing angles (θ_{12},θ_{13},θ_{23}) and CP-violating Kobayashi-Maskawa (KM) phase (δ) [24]. This phase is the only known CP-violation source in the SM. The matrix in its standard parametrization has the following form:

$$V_{CKM} = \begin{bmatrix} c_{12}c_{13} & s_{12}c_{13} & s_{13}e^{-i\delta} \\ -s_{12}c_{23} - c_{12}s_{23}s_{13}e^{i\delta} & c_{12}c_{23} - s_{12}s_{23}s_{13}e^{i\delta} & s_{23}c_{13} \\ s_{12}s_{23} - c_{12}c_{23}s_{13}e^{i\delta} & -c_{12}s_{23} - s_{12}c_{23}s_{13}e^{i\delta} & c_{23}c_{13} \end{bmatrix} \tag{3}$$

where $s_{ij} = \sin(\theta_{ij})$ and $c_{ij} = \cos(\theta_{ij})$. Another popular method is the Wolfenstein parametrization motivated by the relations between mixing angles observed experimentally. Using approximations $s_{13} \ll s_{23} \ll s_{12} \ll 1$ and $c_{13} = c_{23} = 1$ the CKM matrix can be rewritten to [25]

$$V_{CKM} = \begin{bmatrix} 1 - \frac{\lambda^2}{2} & \lambda & A\lambda^3(\rho - i\eta) \\ -\lambda & 1 - \frac{\lambda^2}{2} & A\lambda^2 \\ A\lambda^3(1 - \rho - i\eta) & -A\lambda^2 & 1 \end{bmatrix} \tag{4}$$

where λ, A, ρ and η are the parameters to be determined from experiments.

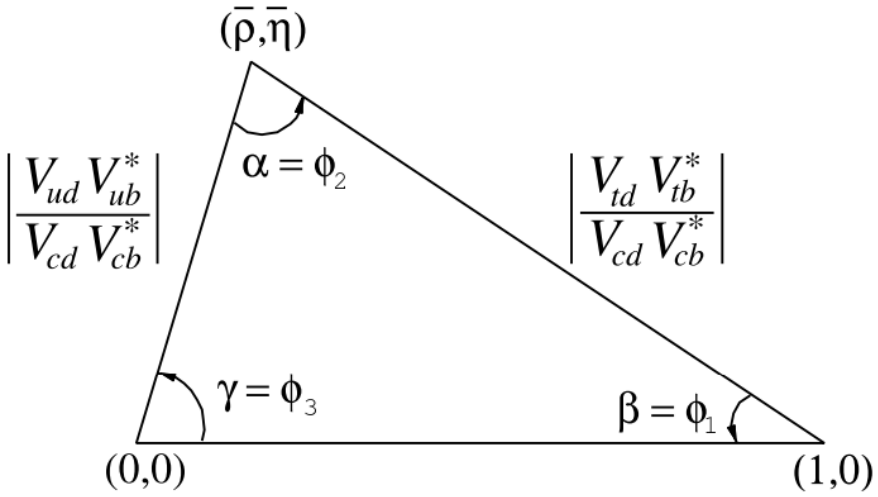

Figure 3: Unitary triangle scheme

The unitary conditions can be represented as triangles in the complex plane. The most common unitary triangle corresponds to the following condition:

$$V_{ud}V_{ub}^* + V_{cd}V_{cb}^* + V_{td}V_{tb}^* = 0 \tag{5}$$

that can be obtained by dividing each side by $V_{cd}V_{cb}^*$ (Fig. 3).

As the CKM matrix parameters are fundamental in the SM it is important to determine theirs precise values. One of the most important goal in flavor physics is to overconstrain the CKM matrix by measuring the CP symmetry breaking parameters using a variety of weak decays. Any inconsistency with the predictions of the Standard Model could be a sign of New Physics. In particular the inconsistency between measurements for the decays occurring at a tree level and via higher order loop diagrams can be interpreted as the influence of propagation of new massive particles inside the loop diagrams.

Using recent results from many experiments the values of all nine CKM [26] elements are determined to be

$$|V_{CKM}| = \begin{bmatrix} 0.97435 \pm 0.00016 & 0.22500 \pm 0.00067 & 0.00369 \pm 0.00011 \\ 0.22486 \pm 0.00067 & 0.97349 \pm 0.00016 & 0.04182^{+0.00085}_{-0.00074} \\ 0.0.00857^{+0.00020}_{-0.00018} & 0.04110^{+0.00083}_{-0.00072} & 0.999118^{+0.000036}_{-0.000031} \end{bmatrix} \tag{6}$$

The illustration of the current status of the experimental results is shown in Fig. 4

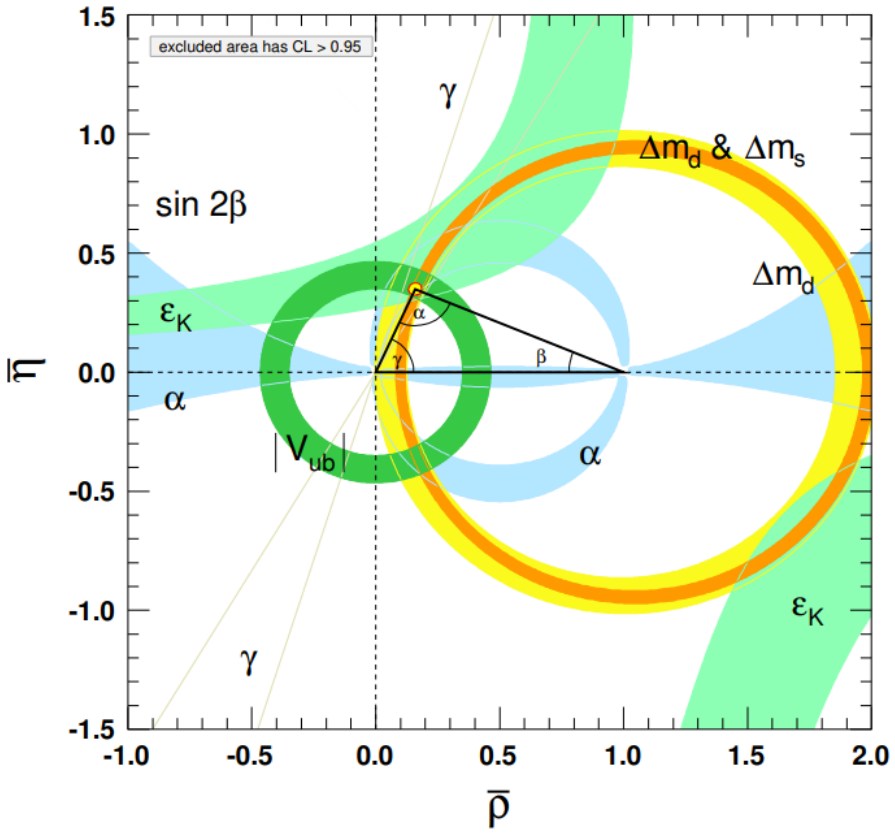

Figure 4: Visualisation of unitary triangle (summer 2022). The shaded regions corresponds to 95% C.L. [26].

2.4 Flavor-changing neutral current and GIM mechanism

The flavor-changing neutral currents (FCNC) are processes in which the flavor of a fermion changes but the electric charge stays the same. In the SM such processes are forbidden at tree level. They can still occur via loop diagrams (see Fig. 5). The FCNC processes are further

suppressed by GIM [27] mechanism (Glashow-Iliopoulos-Maiani) through the interference between diagrams involving a charm quark and an up quark as shown in Fig. 6. This mechanism involving a charm quark (hypothetical at that time) was proposed to explain the measurement of a much smaller branching fraction of $K_L^0 \to \mu^+\mu^-$ decays than predicted for the case of three quarks only. This indirect indication of the existence of a charm quark was later confirmed through direct experimental evidence. The charm quark was discovered in 1974 by a team of researchers led by Samuel Ting and Burton Richter at the Stanford Linear Accelerator Center (SLAC) in California [28, 29].

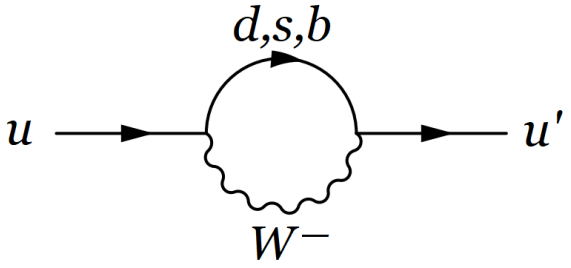

Figure 5: Feynman diagram [30] at one loop level of FCNC transition of u quark to different flavor up-type u' quark.

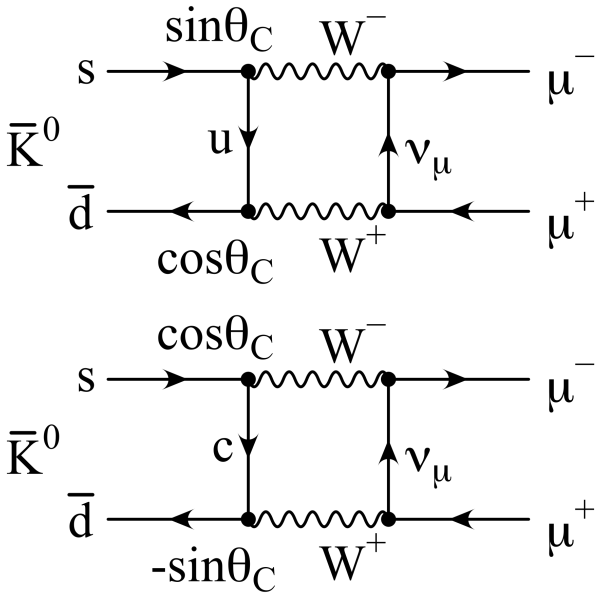

Figure 6: Feynman diagrams for rare leptonic neutral $\overline{K^0}$ decay.

2.5 Lambda Baryons

Lambda baryons (Λ) are hadrons made out of one up quark, one down quark and one quark from other generations. They possess either elementary change +1 or are neutral, and all of them have a total isospin of 0. In 1950 using the data from the observation of cosmic rays in

a balloon experiment at 21,000 meters the lambda baryon Λ^0 was discovered by V.D. Hopper and S. Biswas [31]. The Expected particle was supposed to live for about 10^{-23} s while it managed to survive for about 10^{-10} s. This puzzle was solved later by introducing the concept of quarks which led to the discovery of a strange quark. There are only 3 variants of a Λ baryon observed out of 4 possible ones.

Figure 7: Structure of a Λ^0 baryon.

The notation of a Λ baryon is Λ_f^q, where q indicates the charge (+1 or 0) and f indicates the flavor of a third quark (c, b, t or s if absent). The parameters of possible Λ particle variants are listed in Table 1. The Λ_t^+ baryon cannot be observed as the top quark lifetime is about 1/20 of time needed for hadronization.

Table 1: List of all lambda baryons in Standard Model [32].

Name	Symbol	Quark combination	Charge	Mean lifetime [s]	Invariant mass [MeV/c^2]
lambda	Λ^0	uds	0	$(2.632 \pm 0.020) \times 10^{-10}$	1115.683 ± 0.0006
charm lambda	Λ_c^+	udc	+1	$(201.5 \pm 2.7) \times 10^{-15}$	2286.46 ± 0.14
bottom lambda	Λ_b^0	udb	0	$(1.471 \pm 0.009) \times 10^{-12}$	5619.60 ± 0.17
top lambda	Λ_t^+	udt	+1	—	—

2.6 $\Lambda_c^+ \to p\mu^+\mu^-$ decay

The FCNC decay $\Lambda_c^+ \to p\mu^+\mu^-$ is expected to be heavily suppressed in the SM through the GIM mechanism. The dominant Feynman diagrams of the decay are shown in Fig. 8.

The branching ratios for short-distance (non-resonant) contributions to the transition $c \to ul^+l^-$ are expected to be below 10^{-8} in the SM with the enhancement up to 10^{-6} due to long-distance contributions from intermediate vector meson resonances decaying to a l^+l^- pair [33, 34]. The SM predictions for differential Branching Fraction (BF)s are shown in Fig. 9, taken from Ref. [35]. The resonant SM estimation is based on the measured BFs, and on the isospin relation between the ρ and ω states, to overcome the lack of any experimental information on BF($\Lambda_c^+ \to p\rho$). Strong phases between the resonances, and thus also their interferences, are a priori unknown. Hence, this SM estimation is obtained by

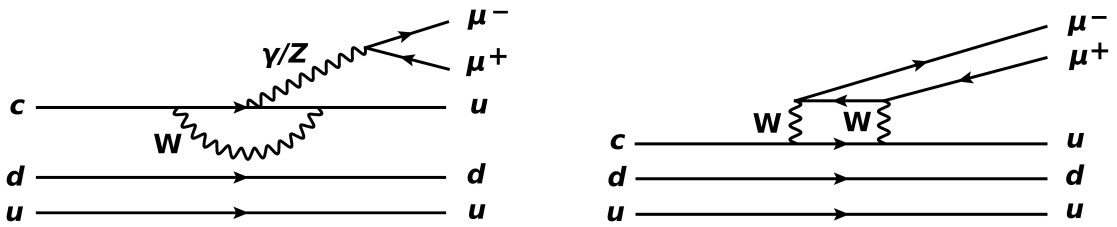

Figure 8: Feynman diagrams for short distance contribution to $\Lambda_c^+ \to p\mu^+\mu^-$ decay.

averaging strong phases of the omega and phi states within $[-\pi, +\pi]$ range. The bands of the estimations illustrate uncertainties coming mainly from hadronic form factors.

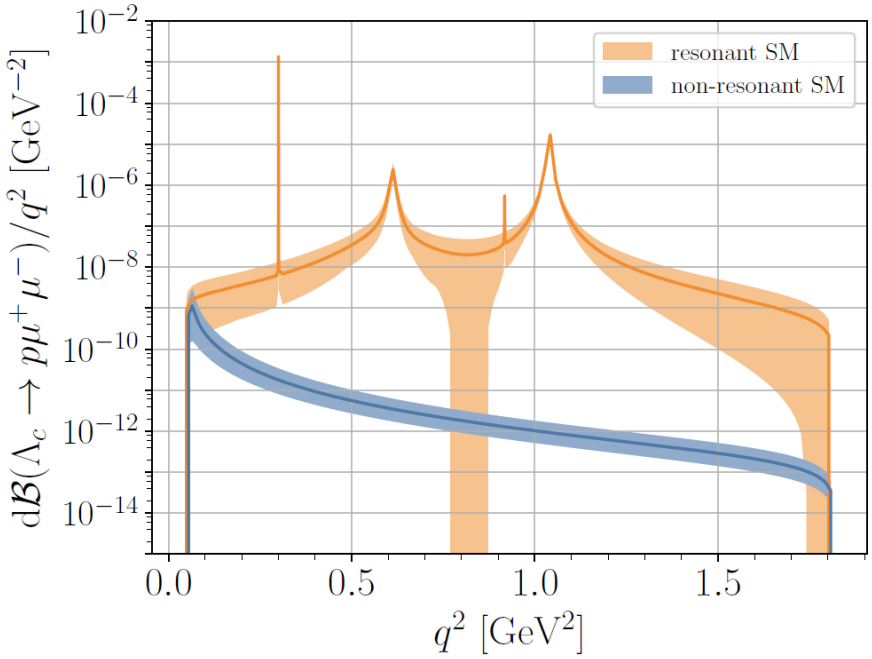

Figure 9: The SM predictions for differential BF of $\Lambda_c^+ \to p\mu^+\mu^-$ [35].

It is worth pointing out that the same type of transitions in the b system $b \to sl^+l^-$ exhibited interesting deviations from the SM predictions in particular in angular observables [36]. The observed anomalies stimulate this search in the charm sector. The charm system is far less explored at both the experimental and theoretical level. The $\Lambda_c^+ \to p\mu^+\mu^-$ decay was studied by the BaBar collaboration [37] yielding $11.1 \pm 5.0 \pm 2.5$ events and an upper limit on the BF of 44×10^{-6} (90 % C.L.). The same study resulted also in the upper limits for the branching fractions on the similar decay: 5.5×10^{-6} for $\Lambda_c \to pe^+e^-$. The LHCb searched for $\Lambda_c^+ \to p\mu^+\mu^-$ in Run 1 data [38] and determined the upper limit for that decay to be 7.7×10^{-8} (90 % C.L.), improving the previous result from BaBar by two orders of magnitude.

3 The LHCb experiment at CERN

3.1 The Large Hadron Collider

One of the most famous research centers for high energy physicists is the European Organisation for Nuclear Research (CERN) [39]. Since its foundation in 1954, many scientists have contributed to a number of discoveries that have led to a breakthrough in the understanding of the laws of the micro-world. One of the most significant revelation was the discovery made in 1983 by the researchers from UA1 and UA2 (Underground area 1 and 2) experiment using the Super Proton Synchrotron (SPS) accelerator. The observation of the $W^{\pm}$ and Z^0 bosons [40] confirmed the foundation of the Standard Model formulated about a decade earlier. It is worth noting that the research conducted at CERN has also wider impact outside the science. A good example is the invention of the World Wide Web (WWW) that almost all of us use on an everyday basis [41]. The LHC is the world's largest and most powerful particle accelerator. The length of the LHC is about 27 km and it is located in an underground tunnel at the depth raging from 50 m to 175 m [42]. It was built in the same tunnel as the previous Large Electron-Positron collider [43] that successfully operated for 11 years up to 2000. The first LHC beam collision took place in 2010. Inside the LHC the two high energy

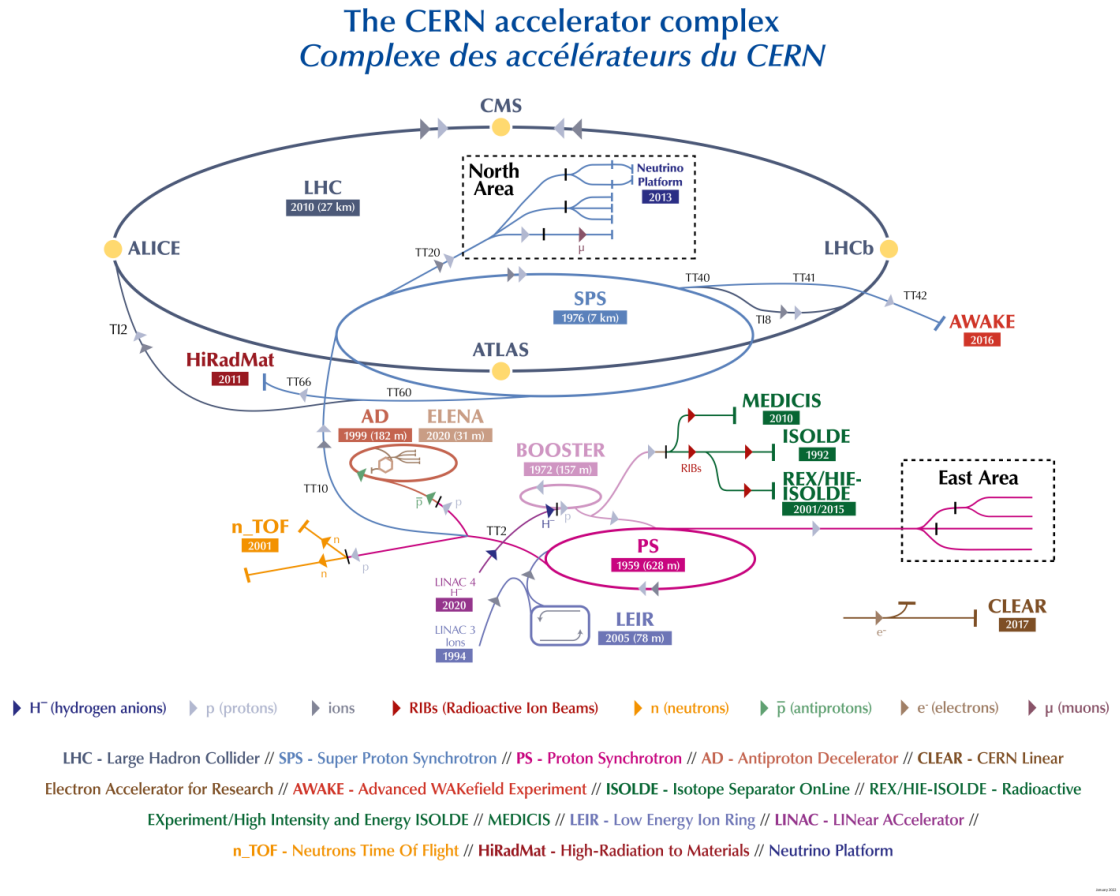

Figure 10: Schematic view of CERN accelerator complex for 2022 [44].

beam lines accelerate particles in opposite directions and collide them at the center of mass energy up to 14 TeV. A schematic view of the entire CERN accelerator complex can be seen in Fig. 10. The primary beam composition for collisions is proton-proton, but collisions of heavy

ions (e.g. lead-lead or proton-lead) are also performed. The acceleration process consists of several steps as shown in Fig. 10. It requires other smaller accelerators to achieve sufficient energy for particles to be injected to the main LHC beam line. The first accelerator that the particles need to go through is LINAC 4 (upgraded from LINAC 2) [45], then the so called BOOSTER, followed by the Proton Synchrotron (PS) [46], and lastly they traverse through the Super Proton Synchrotron (SPS) [47], where the particles are accelerated to an energy of 450 GeV. After reaching the required energy, the beam is injected into the LHC in two opposite directions. Then the beam is accelerated in ultra high vacuum up to 7 TeV. Finally, the beams are set to collide and the data acquisition starts. The LHC program of data taking is divided in the so called "Runs" separated by "Long Shutdowns". Runs are periods when the LHC provides beam collisions to the experiments. As of now there were two runs completed. Run 1 took place in 2011 to 2012 at the center of mass energy of 7 TeV in 2011 and 8 TeV in 2012. Subsequently during Run 2 the data were collected between 2015 and 2018, where the energy at the center of mass was increased to 13 TeV. Right now Run3 is ongoing with the energy of center of mass collision reaching 14 TeV. Run3 phase is planned to continue until the end of 2025. The Long Shutdown which occurs between the consecutive Run phases, is devoted to repairments or improvements of various components of the LHC. The collision energy at the center of mass system is crucial for observations of new massive particles. The aim of ATLAS and CMS is to search directly for the production of new particles, which is possible if the energy available in a collision is high enough to make it possible. Therefore the energy of the LHC was gradually increased from its start and eventually reached nominal 14 TeV in Run3. Another parameter of an accelerator the discovery potential depends on is luminosity, which can generally be described as the ability of an accelerator to produce the necessary number of collisions. The New Physics phenomena are very rare and the probability of their observation is proportional to the number of collisions delivered by an accelerator. The instantaneous luminosity L is defined as

$$\frac{dN}{dt} = L\sigma \tag{7}$$

where dN/dt is the number of collisions per second and σ indicates the cross-section of the process leading to this collision type. Therefore the units of instantaneous luminosity is $cm^{-2}s^{-1}$ The luminosity can be calculated from the parameters of the beam according to the formula:

$$L = \frac{N_a N_b f}{4\pi\sigma_x\sigma_y} \tag{8}$$

where N_a and N_b are the number of protons in colliding bunches, $f = 11.245$ kHz is the revolution frequency of the LHC, and both σ_x and σ_y are the RMS size of the beams in horizontal and vertical trajectory. The LHC goal was to reach the $L = 10^{34}cm^{-2}s^{-1}$ and in 2018 the maximum value reached $L = 2.1 \times 10^{34}cm^{-2}s^{-1}$, which is more than twice the nominal value.

In order to express the number of collisions in a given period of time the integrated luminosity is used which is an integral of instantaneous luminosity over a given period of time. Integrated luminosity relates cross section for a given process and the total number of events that occurred in a given period of time according to the formula:

$$\mathcal{L} = \frac{N}{\sigma} \tag{9}$$

where N indicate the number of events and σ is the cross-section of that process. Reports usually state the value of integrated luminosity in units of inverted cross-section unit e.g. fb^{-1} (inverse femtobarn).

There are four big experiments operating at the LHC:

- ALICE [48] - A Large Ion Collider Experiment.
- ATLAS [49] - A Toroidal Lhc ApparatuS.
- CMS [50] - Compact Muon Solenoid.
- LHCb [51] - Large Hadron Collider beauty.

ALICE is focused on measurements in heavy ion collisions and production of high density matter e.g. quark gluon plasma. ATLAS and CMS are general-purpose detectors used for precise tests of the Standard Model and for searches of New Physics. The advantage of having two experiments is to increase the sensitivity of discoveries and to cross check the results. In 2012 both ATLAS and CMS announced the discovery of the speculated Higgs boson [52, 53]. The LHCb experiment is dedicated to studies in the domain of flavour physics focusing on b-hadrons and c-hadrons.

Besides these main four experiments there are a few smaller ones at the LHC. TOTEM (TOTal Elastic and diffractive cross-section Measurement) [54] located near CMS is an experiment focused on measurements of pp cross-section and serves also as a monitor of the LHC luminosity. The LHCf (Large Hadron Collider forward) [55] placed next to the ATLAS detector is used to study the phenomena related to cosmic rays which can be reproduced in LHC collisions in the available energy range. The MoEDAL (Monopole and Exotics Detector at the LHC) [56] experiment located near the LHCb is mostly focused on physics beyond the Standard Model looking into magnetic monopole or other exotic particles. FASER (ForwArd Seatch ExpeRiment) [57] and SND (Scattering and Neutrino Detector) [58] are both the newest detectors taking data in Run3, for the first time looking into colliding neutrinos and for a physics beyond the Standard Model.

3.2 LHCb detector

The LHCb detector was designed to study CP symmetry violation phenomena and to search for New Physics in rare decays of charm and beauty hadrons. Contrary to other three main experiments where the detectors cover almost full 4π region, the LHCb detector is a single-arm spectrometer with forward pseudorapidity, η, covering the range $2 < \eta < 5$. The pseudorapidity η is defined as

$$\eta \equiv -ln\left[\tan\left(\frac{\theta}{2}\right)\right] \tag{10}$$

where θ is the angle measured from the positive z axis along the beam direction in which the y axis points vertically and x axis point towards the center of the LHC ring. This corresponds to angular acceptance of [10,250] mrad in its horizontal (bending) plane and [10,300] mrad in vertical (non-bending) plane. Thanks to that coverage, about 27% of b quark and $\bar{b}$ antiquark production at LHC can fall inside the LHCb acceptance. Fig. 11 shows a schematic view of the LHCb detector. The beams are colliding close to the VELO. Part of the particles produced at the interaction point enters the LHCb acceptance and propagate from left to right (positive z axis direction). They pass trough the VELO, where the primary vertex is reconstructed. Then they traverse RICH1 (particle identification), TT (tracking for low momentum tracks), the magnet, T1-T3 (track reconstruction), RICH2, ECAL (electromagnetic calorimetry), HCAL (hadron calorimetry) and M1-M5 (muon stations for muon identification).

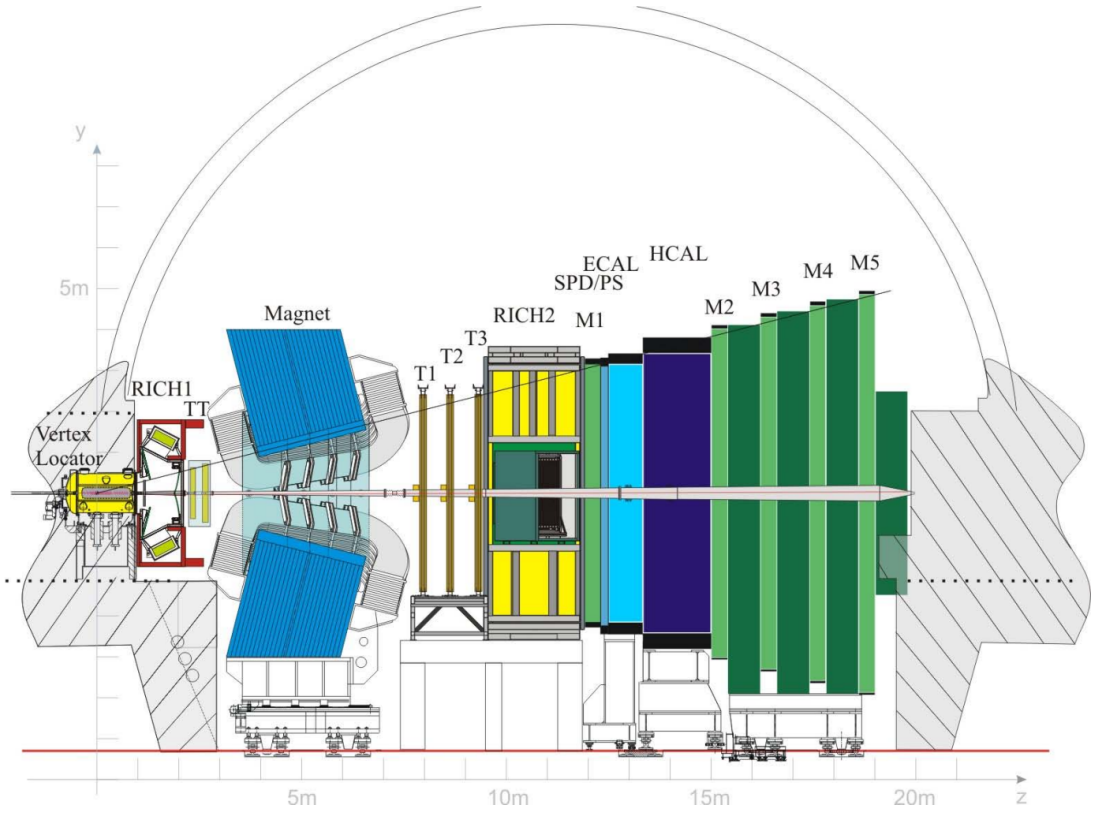

Figure 11: Side view of the LHCb detector [51].

To cope with the high density of tracks in the forward region, the LHCb experiment works at the lowered luminosity compared to ATLAS and CMS. In Run2 the maximum luminosity tuned at the LHCb collision point was $4 \times 10^{32} cm^{-2} s^{-1}$.

3.2.1 Magnet

The LHCb dipole magnet [59] is covering forward acceptance of about 300 mrad horizontally and 250 vertically and is located between the tracking stations TT and T1-T3. Both top and bottom components weigh about 160 tons and are made out of 100 mm thick laminated low carbon steel plates. The coils are allocated in the magnet yoke mirror-sympathetically to each other and each of them is made out of 15 the so called "pancakes" divided in 3×5 groups. The magnetic field produced by coils is about 4 Tm along 10 m that enables bending of charged particles to measure their momentum. In order to avoid some systematic effects and to obtain precise CP violation measurements, the polarity of magnets is reversed a couple of times during a year. The measurements of events can be divided into two groups, each having either its polarity Up or Down (commonly referred to as MagUp and MagDown), where each polarity contains about half of the data. For this analysis the magnet polarity is not relevant and both types are merged together.

3.2.2 Tracking

The purpose of the tracking system is to reconstruct the trajectory of passing particles as well as their momenta. The system includes VELO [60] and four tracking stations (TT and T1-T3). As a good reconstruction of primary and secondary vertices is required for the study of b- and c-hadrons decays, the VELO was located as close as possible to the interaction point of

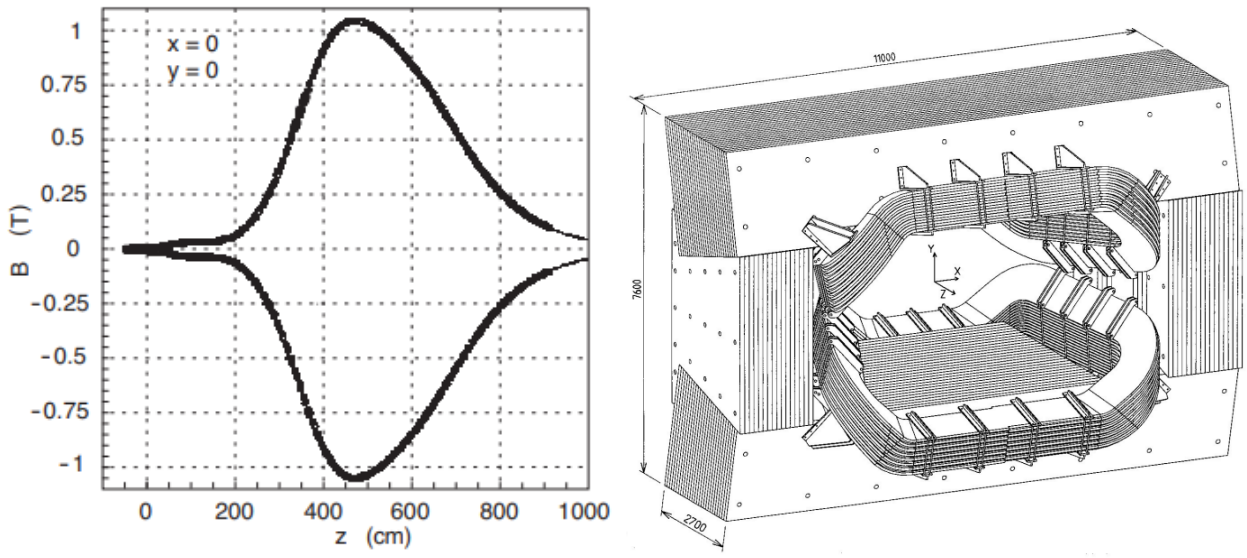

(a) (b)

Figure 12: Magnetic field along the z axis (a) and design sketch of dipole magnet (b).

two proton beams. Each of two VELO halves consists of 21 modules and produces information about both the ϕ and r coordinates, giving one $\phi - R$ point used in the reconstruction. The sensors are located in a vacuum vessel (10^{-4} mbar) separated from the LHC ultra high vacuum (10^{-8} mbar) by a thin aluminum sheet. The replacing beam pipe by aluminum foil enabled one to reduce the material traversed by particles and at the same time allowing two halves of the detector to overlap. A sketch of VELO cross section is shown in Fig. 13 (a).

Based on the information from VELO, one is able to calculate the decay lifetime and impact parameter (IP) of decaying hadrons, the information helpful to identify their flavour. The two halves are located about 8 mm near the beam line during stable conditions. They are, however, too close during the injection of the beams by the LHC as they could interact with the beam and produce too much radiation. To prevent such situations, the two parts are retracted during a beam injection or unstable beam conditions and are joined again once stable beams are announced (Fig. 13 (b)). The small distance between the beam and the sensors requires the detector to be kept cooled to a temperature below $-5°$ C at all times. The cooling system is composed of stainless steel pipes with circulating CO_2. The performance of the sensor depends on a signal to noise ratio (S/N) that is aimed to be at least 14. The spatial resolution of the clusters for a 100 mrad track in the smallest strip pitch region is 4 μm. The satisfactory impact parameter resolution is achieved approaching asymptotically 12 μm for the highest transverse momentum particles.

The second part of the tracking system, the tracking stations, is divided into two locations. The TT is located upstream of the magnet while the T1-T3 stations are placed downstream the magnet. The tracking stations T1-T3 consist of two parts: the inner part, IT [61], based on silicon strip technology which are located close to the beam line, and the outer part, OT [62], covering larger angles. Fig. 14 shows the arrangement of the tracking stations. Both TT and IT are made out of silicon microstrip sensors, with a strip pitch of about 200 μm. The OT is a drift chamber detector in the form of an array of gas-tight straw tubes. The mixture of argon (70%) and CO_2 (30%) is used to guarantee drift time below 50 ns resulting in about 200 μm drift-coordinate resolution. Every tracking station has four detection layers, which are positioned in so-called x-u-v-x views where vertical strips are placed as the first

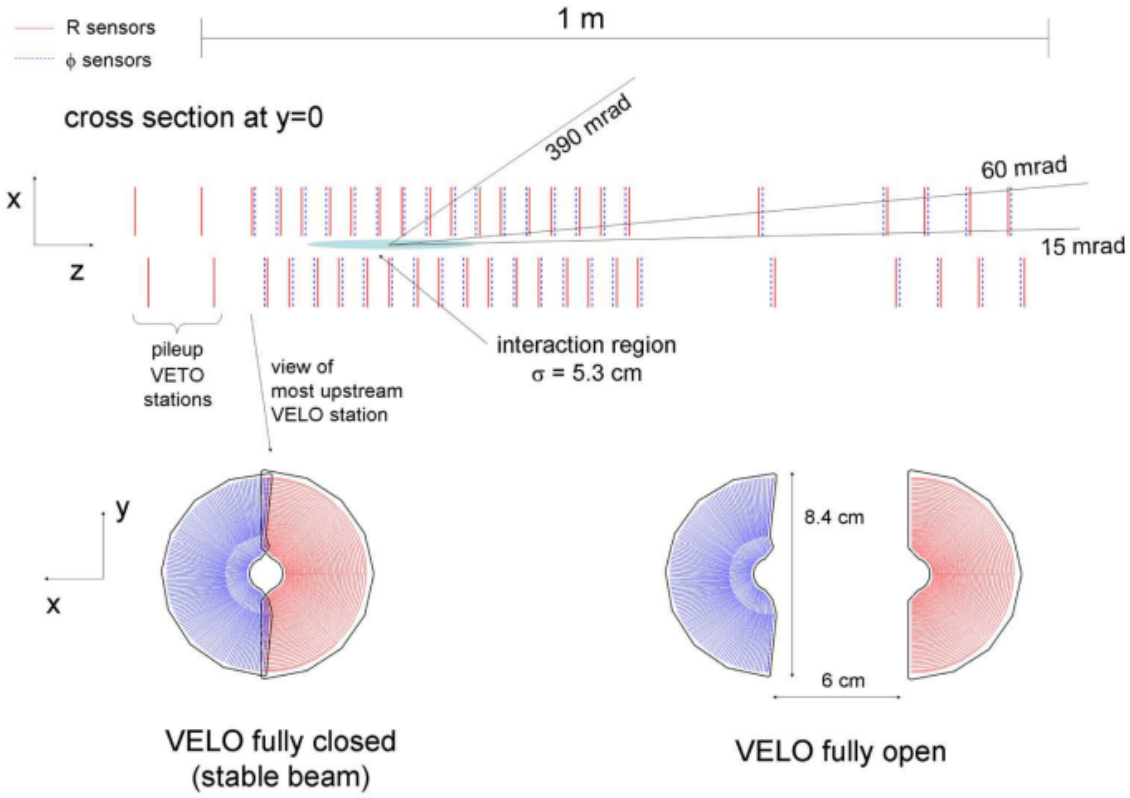

Figure 13: VELO cross section in x,z plane at $y = 0$ for closed situation. Bottom half illustrates closed and open positions of the detector.

and last layer, and the inner ones are rotated by a stereo angle of $-5°$ and $5°$.

Depending on the composition of the detectors the particle track has been reconstructed in, one can distinguish various types of the tracks (Fig. 15).

- Long track - starting from VELO, it crosses the entire tracking system, hitting all the tracking stations. Such tracks provide the most accurate momentum measurement and therefore are used in most LHCb analyses.

- Upstream track - produced by a charged particle that passes through the upstream tracking detectors VELO and TT. These tracks are mostly low momentum tracks which are bent in the magnet and do not reach the downstream tracking detectors.

- Downstream track - produced by a charged particle that is not reconstructed in VELO and passes through the TT station and the downstream tracking detectors T1-T3. These tracks mostly correspond to the secondaries of neutral particles with a relatively long lifetime like K_S^0 or Λ^0.

- VELO track - produced by charged particles that pass through the VELO detector. They provide precise information about the position and trajectory of the particles at the point of collision. They are mostly used for PV reconstruction.

- T track - leaving only hits in T stations, mostly by long lived secondary decays.

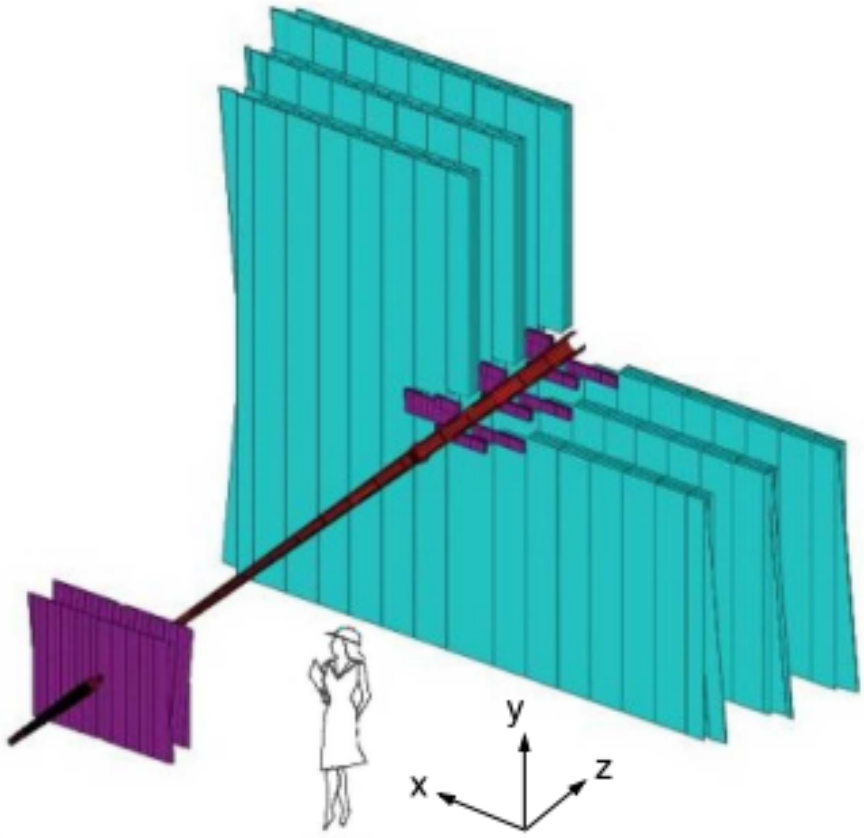

Figure 14: Arrangements of tracking stations with TT on the left and T1-T3 on the right. The ST part is highlighted in purple while OT in turquoise.

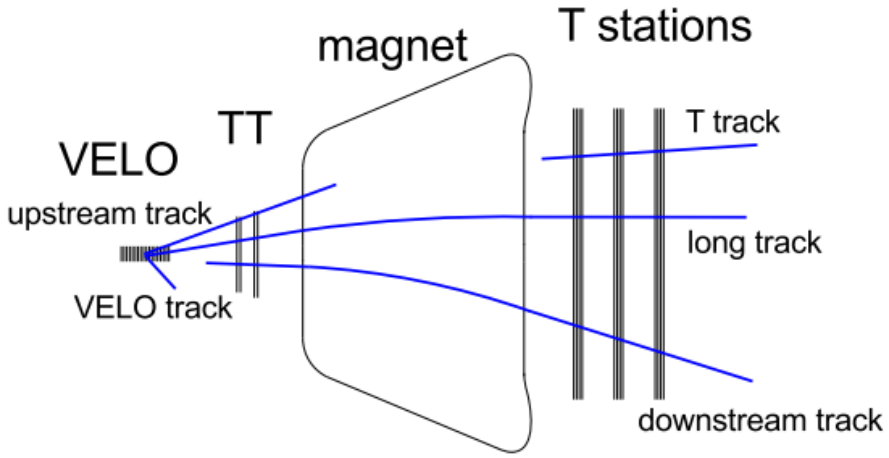

Figure 15: Track types in LHCb detector [63].

3.2.3 Particle Identification

The Particle Identification (PID) system uses data gathered from the dedicated subsystems, including both the RICH1 and RICH2 detectors [64], two calorimeters and the muon stations M1-M5. Two RICH detectors provides a wide range of momentum for particle identification.

The RICH1 detector covers the lower ranges of about 1-60 GeV/c using a C_4F_{10} radiator and special aerogel, while RICH2 covers the higher range of about 15-100 GeV/c using CF_4 radiator (Fig. 16). The detection process in both RICH1 and RICH2 uses Cherenkov radia-

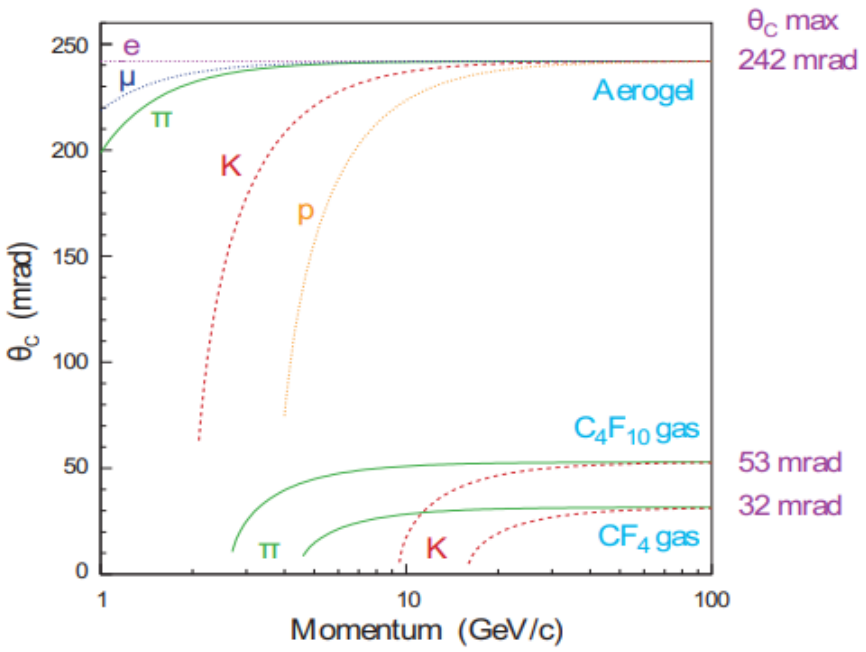

Figure 16: Cherenkov angle versus particle momentum for different radiators and particles.

tion [65] emitted by charged particles going through medium with the speed higher than the speed of light in that medium. These radiation photons are emitted in the form of cone. The angle of that cone, the Cherenkov angle, can be written as

$$\cos\theta_c = \frac{1}{n\beta} \tag{11}$$

where $\beta = v/c$. Combining the information from the tracking detectors and knowing the Cherenkov angle, the particle mass can be estimated (thus particle identification). The emitted light produced by moving particles is reflected by a special spherical mirror system into tubes that redirect it into the Hybrid Photo Detectors (HPD), where signals induced by photons are detected. Figure 17 shows a schematic view of both the RICH1 and RICH2 detector.

After leaving the RICH2 detector, the particles travel through the calorimeters. The calorimeter system is composed of the electromagnetic (ECAL) and hadronic (HCAL) one as well as the Scintillating Pad Detector (SPD) and preshower (PS) [66] components. The purpose of the system is to identify electrons, photons and hadrons by measuring the patterns of their deposits.

The muon stations M1-M5 [67] are located at the end of the LHCb detector. The entire system has 1380 chambers covering about 435 m^2. The measurement of muons p_T is done in the first 3 stations leaving the fourth and fifth one mainly for the identification. To remove any hadrons that managed to pass through HCAL, a 80 cm thick iron-absorber is placed between the M2-M5 stations. Thanks to the information provided by the muon stations, the

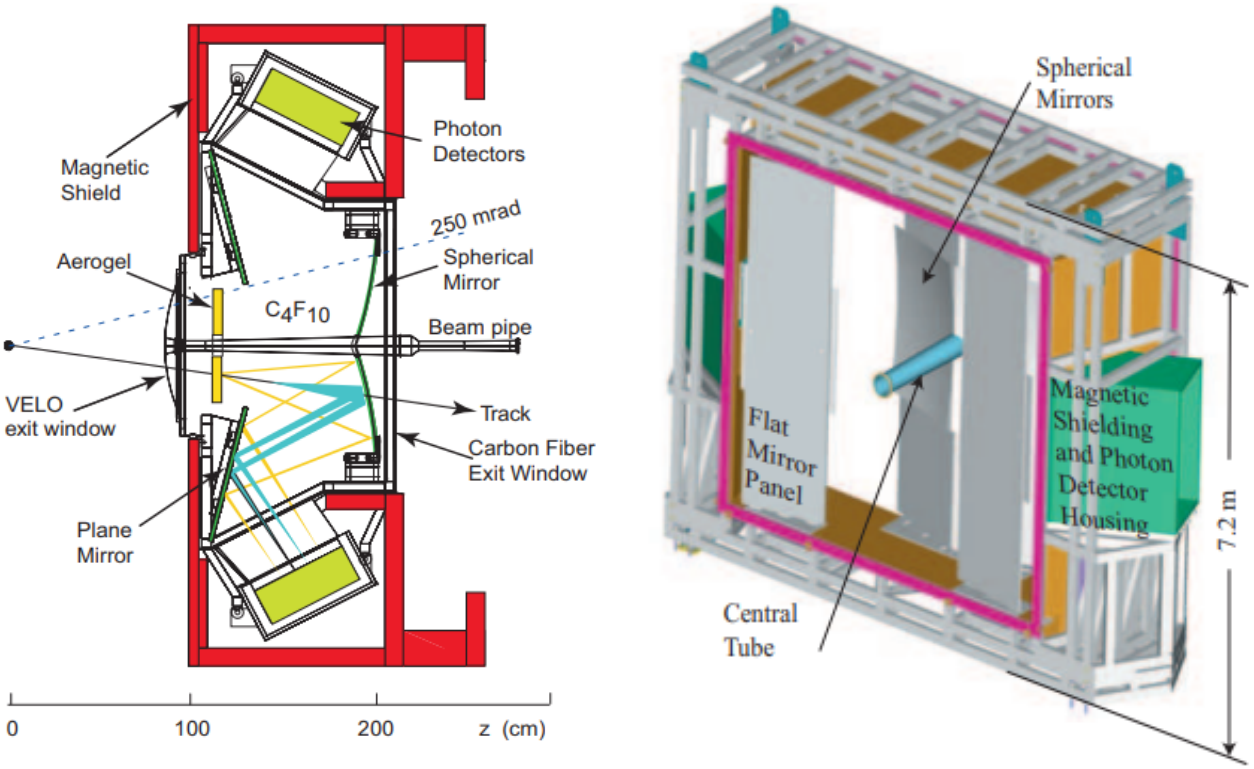

(a) (b)

Figure 17: Schematic view of RICH1 (a) and RICH2 (b) detectors.

momentum resolution of muons used in the later stages of the selection improves by about 30% compared to only using the tracking stations [68].

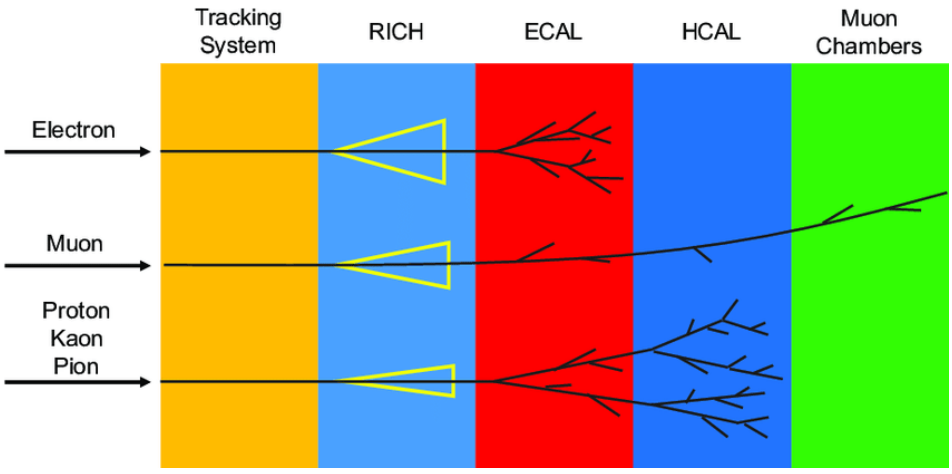

Figure 18: Illustration of particle detection response by LHCb detector [69].

Using data from the RICH detectors, calorimeters and muon chambers, the LHCb framework can start particle identification. One of the methods is called DLL (Delta Log Likelihood), which estimates the likelihood probability using the mass hypothesis with respect to a π particle. The difference in logarithmic likelihood is calculated as $DLL(A-B) = \ln \mathcal{L}_{\mathcal{A}} - \ln \mathcal{L}_{\mathcal{B}}$ where $\mathcal{L}_{\mathcal{A}}$ and $\mathcal{L}_{\mathcal{B}}$ are the likelihoods for particle identification for A or B type. Another method that can be used is ProbNN [70]. It combines the information from various compo-

nents via Multivariate Analysis (MVA). The value of ProbNN gives the probability that a track corresponds to a given particle: proton, kaon, pion, electron or photon. In this analysis the ProbNN probabilities for a proton and for a muon are used: $ProbNNp$ and $ProbNNmu$.

3.2.4 Trigger system

The full amount of data generated in the LHCb detector is far too excessive to be kept for offline analysis. The main limitation is the size of the available disk storage. Most of the collisions correspond to well know processes. The main purpose of the trigger is to reject uninteresting events as soon as possible while keeping high efficiency for processes which are to be studied. The trigger system reduces the information received from the detector from about 40 MHz rate to 12.5 kHz (Fig. 19) This trigger system is divided into 3 parts:

- Level-0 (L0), hardware trigger reduces the rate of events from 40 MHz to about 1 MHz.
- High Level Trigger I (HLT1), first level of software trigger reduces the rate of events further down to 110 kHz.
- High Level Trigger II (HLT2), second level of software trigger giving the final rate of events of about 12.5 kHz.

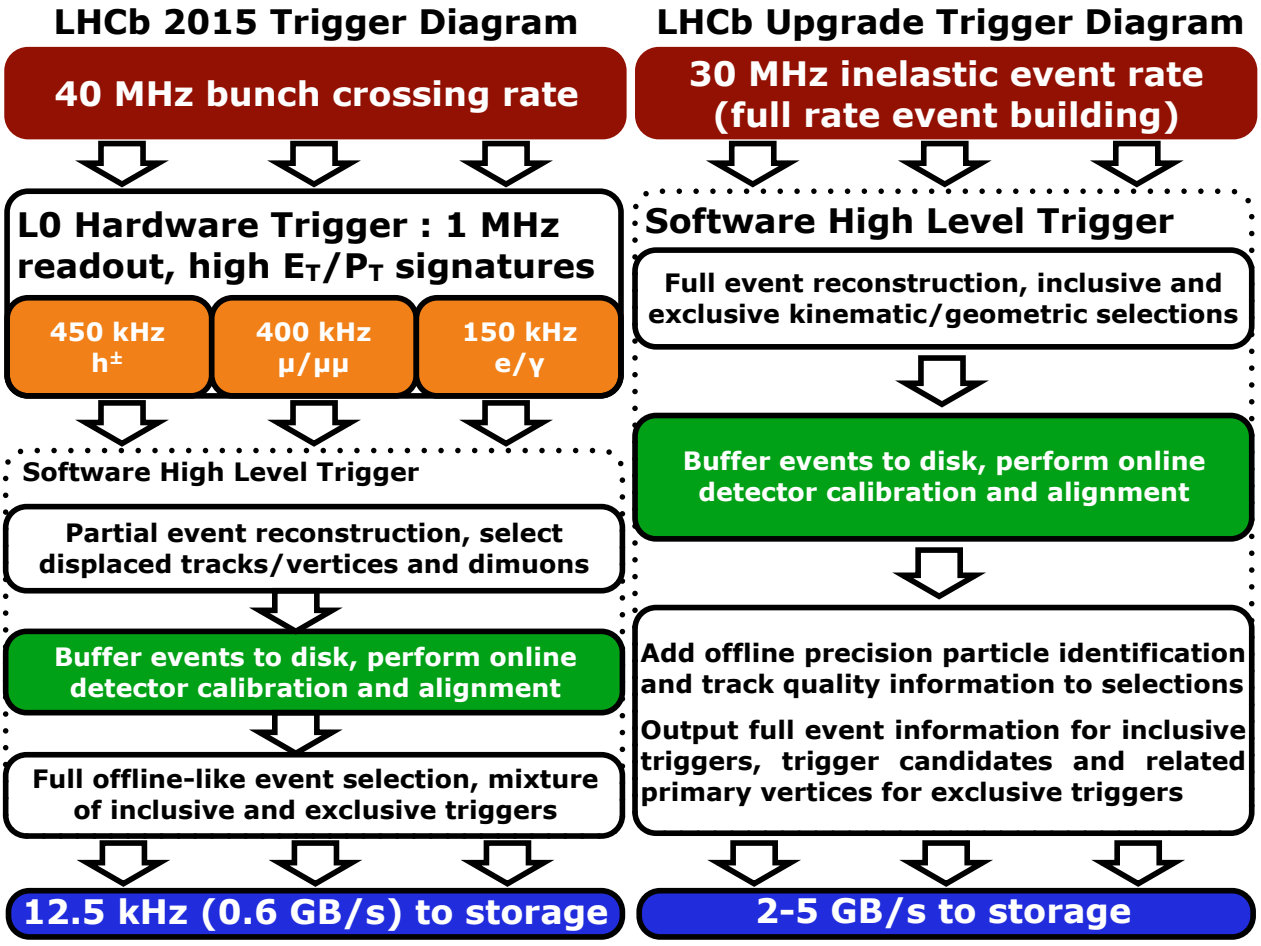

(a) (b)

Figure 19: Schematic view of Trigger system in LHCb for Run2 (2015-2018) (a) and Run3 (2022+) (b) [71].

The L0 hardware trigger is the first step in reducing the background data before it goes through the software stage. The three components can be recognized. The first one is the pile-up system that measures if the event had one or more (and how many) visible interactions by looking at the data from the VELO detector. The other component of L0 uses information from the calorimeter system. The signatures of high transverse energy (E_T) particles: photons, electrons and hadrons are searched for. The corresponding L0 objects are defined as: Electron trigger (L0Electron), Photon trigger (L0Photon), Hadron trigger (L0Hadron) each of them satisfying different conditions. The last part of the L0 is the L0

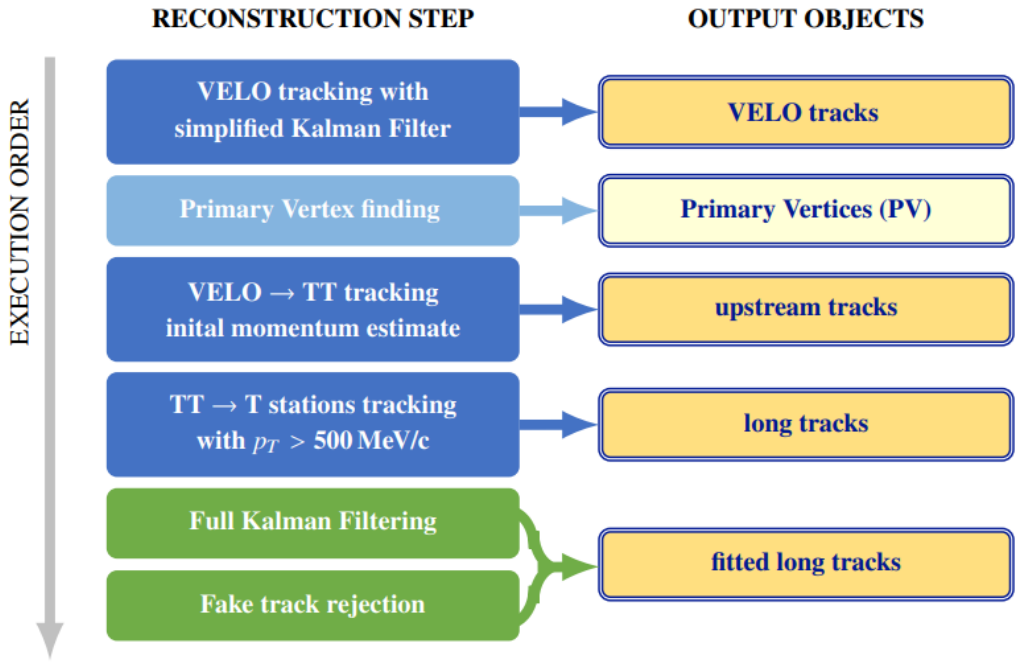

Figure 20: HLT1 scheme of primary vertex and track reconstruction.

muon trigger that searches for muons using data from the five muon stations M1-M5 by looking at the transverse momentum greater than the required threshold. The muon stations are connected to a special L0 muon processor which looks at the highest and second highest p_t muon candidates. The entire system is divided into 192 towers (48 each per station) that work in parallel with the processing unit flagging the particles as muon with Muon trigger(L0Muon) or as a dimuon using Di-Muon trigger (L0DiMuon).

After the hardware part the events go through two levels of software triggers called HLT1 and HLT2. The algorithms written in C++ are running on dedicated computing cluster called the Event Filter Farm (EFF). The HLT1 performs selection for events based on one or two track signatures, the presence of a muon track displaced from primary vertices or on a dimuon combination [72]. For calibration or further testing the events are saved on the storage before they can enter the HLT2 stage. Fig. 20 shows a simplified sketch of the HLT1 output.

A special Kalman filtering algorithm [73] is used to increase the quality of track reconstruction taking into account effects such as ionisation energy loss or multiple scattering. The last step of the trigger system is HLT2, where information is taken from the previous step, the RICH and the calorimeters. In the trigger system, specific algorithms called trigger lines are prepared containing a set of cuts, used different selections. Where in the HLT1 number of lines was about 20, the HLT2 line number is above 500. This is due to a variation in the

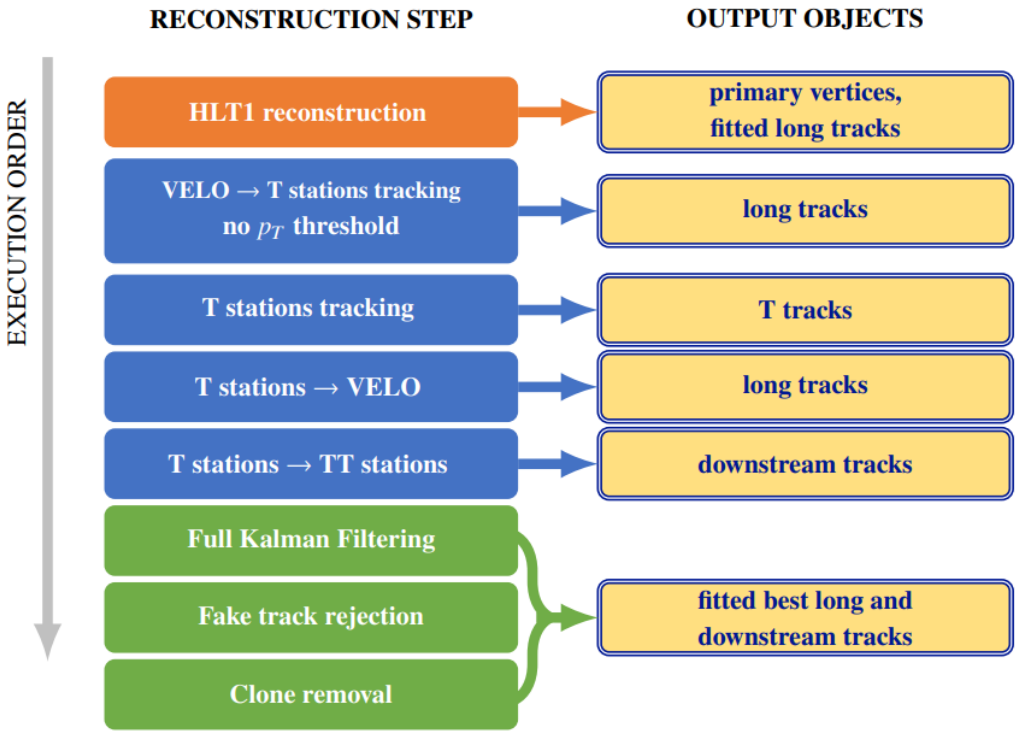

Figure 21: HLT2 scheme of vertex and track reconstruction.

parameters of each recorded event where specific cased are then taken for personal analysis. Most of the HLT2 lines look for either specific final state (exclusive) or partially reconstructed decays (inclusive).

The selection of particular trigger lines can lead to the categorization of events into three groups:

- TOS - Trigger On Signal where the trigger reacts to a signal candidate,
- TIS - Trigger Independent of Signal where the trigger reacts to an underlying event (all tracks excluding signal tracks).
- TOB - Trigger on Both, when the event cannot be categorized into one of the first two.

It is worth mentioning that both TOS and TIS can occur at the same time. Events having the TOB type of trigger are usually rejected as they exhibit a complicated correlation pattern which is hard to reproduce correctly in the simulation.

3.3 Software and Datasets

3.3.1 Software

The LHCb computing framework is composed of different applications mostly based on software architecture Gaudi [74] developed in C++. The purpose of this is to have the common ground to work on each other's results but at the same time to keep them separated for their design job. The Gaudi software architecture emphasizes the use of well-established software engineering principles such as modularity, extensibility, and reusability. Gaudi incorporates a sophisticated event data model that enables the representation, manipulation, and storage of particle collision data. It provides a comprehensive framework for managing event reconstruction, simulation, and calibration processes.

The events selected by a trigger are saved on a disk and wait for the reconstruction by the Brunel application [75]. The Brunel output is saved as Data Summary Tape (DST) with information about the reconstructed objects. Although the data is significantly reduced by the previous steps, it is still not enough to go through a specific analysis. The central selection step is introduced which is called *data stripping*. For that special selection algorithms that contain relatively loose cuts are prepared. These dedicated selections are referred to as *stripping lines* and are performed centrally using the Worldwide LHC Computing Grid (WLCG) [76]. Only the data after *stripping* is placed on the WLCG storage disc and is made available to the users. Further reduction of data is performed by means of the DaVinci application [77] based on Gaudi framework. The distributed computing system called DIRAC [78] is used to submit a large number of DaVinci jobs to WLCG and to collect the output in the form of *ntuples* in ROOT [79] format. Fig. 22 shows the whole data precessing stages for real data and for simulated data. Samples of MC events are generated to resample the data as much

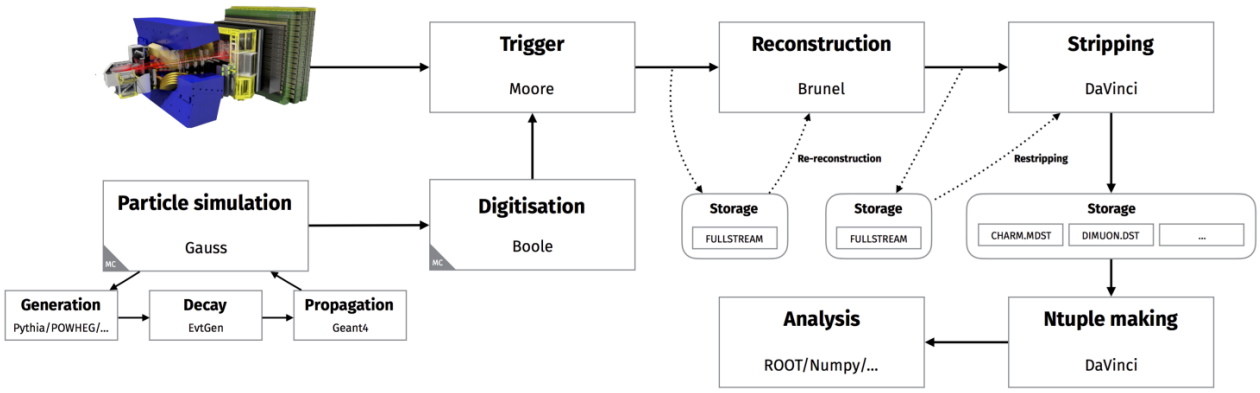

Figure 22: The LHCb data flow and data processing applications used in each stages [80].

as possible. The two high level applications to prepare the simulated events are Gauss and Boole. The first stage of simulation is to generate a proton-proton collision using the event generator PYTHIA [81]. The time evolution of outgoing particles and their decay is done by EvtGen [82]. Then the particles are propagated through the detector and the material interactions of the particles with the detector are simulated using GEANT4 [83]. The whole process is followed by the digitization performed by BOOLE [84]. The response of the detector readout electronics is emulated and the output data is produced in exactly the same format as if they came from the real LHCb detector.

Many other applications are available for data analysis. One of them is PIDCalib [85], widely used inside the LHCb. The PIDCalib package is a set of tools developed to help

analysts determine the efficiency of the PID selection requirements. Another example is GammaCommbo [86], a statistical framework to combine results and set confidence intervals and limits on measured parameters.

3.3.2 Data samples

The results are obtained using the datasets collected at a center-of-mass energy of $\sqrt{s} =$ 13 TeV in 2016-2018, corresponding to a total of 5.4 fb^{-1} of integrated luminosity. The integrated luminosities for various periods of data taking are shown in Fig. 23.

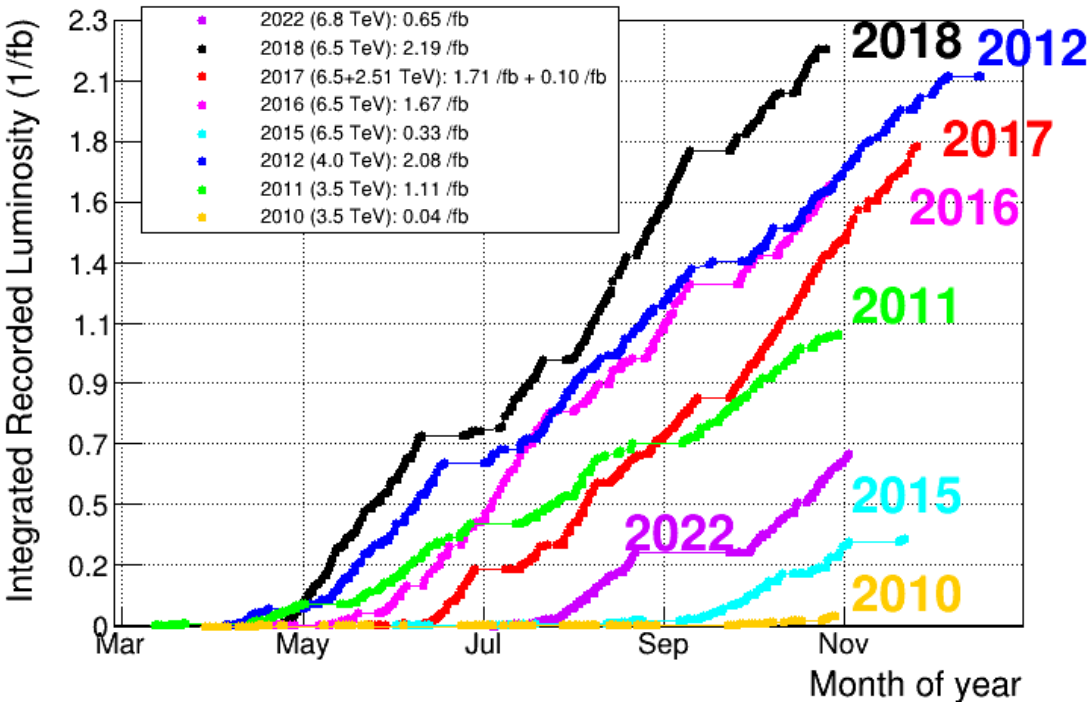

Figure 23: Integrated luminosity recorded by LHCb detector for various years of Run1 and Run2.

3.3.3 Simulation samples

The signal samples are simulated separately for each year using Pythia8 at the generation stage and the phase space model for the decay. The samples corresponding to the normalization channel, $\Lambda_c^+ \to p\phi(\mu^+\mu^-)$, are generated using a phase space model for $p\phi$ decay and the PHOTOS VLL model for $\phi \to \mu^+\mu^-$. Similar samples are produced for $\Lambda_c^+ \to p\omega(\mu^+\mu^-)$. The efficiencies of cuts at the generation stage are taken into account in the analysis. They are listed in Table 2.

Standard ntuples are produced using the DaVinci application. The statistics of simulation samples used in the analysis are listed in Table 3. They contain the standard mixture of prompt Λ_c^+ production and secondary Λ_c^+ production via a b-hadrons decay generated in proportions according to $b\bar{b}$ and $c\bar{c}$ cross-sections. In the following analysis the simulation samples correspond to the standard mixture unless explicitly stated otherwise.

Table 2: The efficiencies of the cuts at the generation phase.

Channel	Generator efficiency (Gauss factor)
$\Lambda_c^+ \to p(\mu^+\mu^-)$ (PhaseSpace)	0.1842 ± 0.0023
$\Lambda_c^+ \to p\phi(\mu^+\mu^-)$	0.1910 ± 0.0024
$\Lambda_c^+ \to p\omega(\mu^+\mu^-)$	0.1742 ± 0.0022
$\Lambda_c^+ \to p\pi^+\pi^-$	0.07948 ± 0.00108

Table 3: Main simulation samples used in the analysis.

Channel	Number of events	Year
$\Lambda_c^+ \to p(\mu^+\mu^-)$	1 004 000	2016
$\Lambda_c^+ \to p(\mu^+\mu^-)$	1 006 997	2017
$\Lambda_c^+ \to p(\mu^+\mu^-)$	1 005 599	2018
$\Lambda_c^+ \to p\phi(\mu^+\mu^-)$	1 007 472	2016
$\Lambda_c^+ \to p\phi(\mu^+\mu^-)$	1 003 271	2017
$\Lambda_c^+ \to p\phi(\mu^+\mu^-)$	1 004 677	2018
$\Lambda_c^+ \to p\omega(\mu^+\mu^-)$	1 004 000	2016
$\Lambda_c^+ \to p\omega(\mu^+\mu^-)$	1 002 000	2017
$\Lambda_c^+ \to p\omega(\mu^+\mu^-)$	1 013 200	2018
$\Lambda_c^+ \to p\rho(\mu^+\mu^-)$	1 003 797	2016
$\Lambda_c^+ \to p\rho(\mu^+\mu^-)$	1 005 399	2017
$\Lambda_c^+ \to p\rho(\mu^+\mu^-)$	1 013 600	2018

4 Analysis Strategy

The aim of the analysis is to search for NP in the $\Lambda_c^+ \to p\mu^+\mu^-$ decay or to set an Upper Limit (UL) on $\Lambda_c^+ \to p\mu^+\mu^-$ branching fraction in various regions of dimuon mass if no significant signal is observed. The signature of the NP would be a disagreement with the prediction of the SM for short distance transitions i.e. the higher branching fraction measured in the non-resonant regions of dimuon mass. The non resonant region, referred to also as the *signal* region in the following analysis, includes a kinematically available range of dimuon mass excluding regions around four resonances: ϕ, ρ, ω and η. It results in a sum of two ranges listed in Table 4.

Table 4: The definition of *signal* region being the sum of two dimuon mass ranges. Central values for particle masses are taken from PDG2022 [87].

Name	Range [MeV/c^2]	Additional informations
low q^2	$211.32 < m_{\mu^+\mu^-} < 507.86$	[min phase space, $m_\eta - 40$ MeV/c^2]
high q^2	$1059.45 < m_{\mu^+\mu^-} < 1348.13$	[$m_\phi + 40$ MeV/c^2, max phase space]
signal	low q^2 range or high q^2 range	sum of *low* q^2 and *high* q^2 ranges

The remaining region containing the resonances is divided as specified in Table 5. It is called a resonant region. The definitions of various q^2 ranges are given in Fig. 24.

Table 5: The definition of regions in the resonant part of the dimuon mass range. For the lower and upper bound of ρ region, the $\pm 3\sigma_\rho$ is taken, where the $\sigma_\rho = 63.31$ MeV/c^2 is calculated as FWHM$_\rho$/2.355. The lower bound for ρ region is taken as maximum of $m_\eta + 40$ MeV/c^2 (587.86 MeV/c^2) and $m_\rho - 3\sigma_\rho$ (585.32 MeV/c^2) to avoid a small overlap with η region.

Name	Range [MeV/c^2]	Additional informations
η region	$507.86 < m_{\mu^+\mu^-} < 587.86$	$m_\eta \pm 40$ MeV/c^2
ω/ρ region	$742.65 < m_{\mu^+\mu^-} < 822.65$	$m_\omega \pm 40$ MeV/c^2
ρ region	$587.86 < m_{\mu^+\mu^-} < 965.20$ excluding ω/ρ region	$m_\rho \pm 3\sigma_\rho$ excluding overlap with ω
ϕ region	$979.46 < m_{\mu^+\mu^-} < 1059.46$	$m_\phi \pm 40$ MeV/c^2

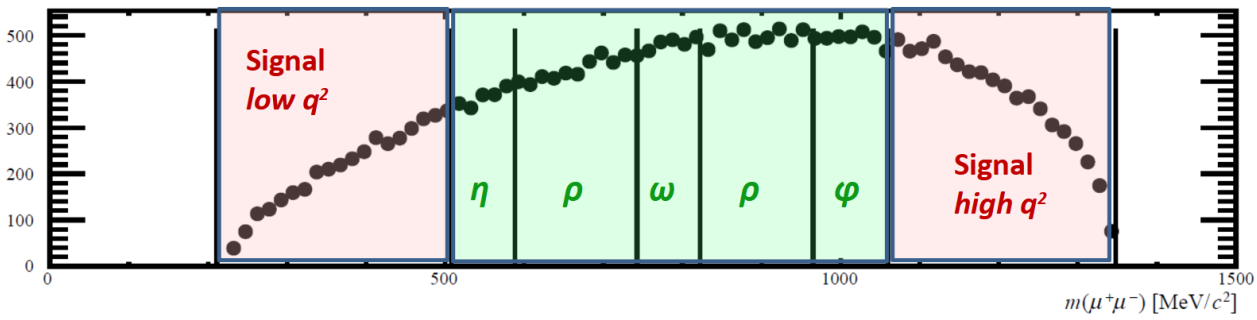

Figure 24: Illustration of different q^2 regions used in analysis.

The events are preselected by the stripping line Lc23MuLc2pmumuLine, where relatively loose topological cuts are imposed (Sec. 5.1) and IsMuon flag for muon tracks is required to be true. The MC samples for the *signal* are produced for each data taking year separately and processed in the same way as the data. The ROOT ntuples are created with entries for every candidate found in the stripping step.

The BF is to be determined with respect to another decay channel with known BF (normalization channel). The $\Lambda_c^+ \to p\phi(\mu^+\mu^-)$ was taken for normalization. The BFs $B(\Lambda_c^+ \to p\phi)$ and $B(\phi \to \mu^+\mu^-)$ are taken from PDG2022 [87]. The advantage is that the final state is the same as for the *signal* and most of the systematic uncertainties cancel in the ratio because of various efficiencies and particle identification. The following formula is used:

$$\frac{B(\Lambda_c^+ \to p\mu^+\mu^-)}{B(\Lambda_c^+ \to p\phi(\mu^+\mu^-))} = \frac{\epsilon_{\text{norm}}{}^{\text{TOT}}}{\epsilon_{\text{sig}}{}^{\text{TOT}}} \times \frac{N_{\text{sig}}}{N_{\text{norm}}}, \tag{12}$$

where N_{sig} is the number of observed *signal* events and N_{norm} is the number of observed $\Lambda_c^+ \to p\phi(\mu^+\mu^-)$ events. The $\epsilon_{\text{sig}}^{\text{TOT}}$ and $\epsilon_{\text{norm}}^{\text{TOT}}$ indicate the corresponding total efficiencies for the *signal* and normalization channels, respectively.

The combinatorial background is reduced by a topological selection using the BDT method provided within the TMVA package [88]. The BDT discrimination is done in two steps. The initial BDT employs topological variables of Λ_c^+ only. It is used as one of the preselection requirements to obtain a good signal to background ratio for $\Lambda_c^+ \to p\phi(\mu^+\mu^-)$ to check data-MC agreement and correct incompatibilities seen in distributions of variables used in the selection (such as Λ_c^+ transverse momentum or the number of tracks in an event). The correction is done using adaptive reweighting applied to MC samples. In addition, the samples after this preselection are used to construct the Probability Density Function (PDF) for the optimization of final cuts using the method of pseudo experiments. The final BDT stage, contains a full set of variables from the initial BDT and additional variables related to the decay products.

The Confidence Level on Signal (CLs) method is chosen for the determination of the upper limits. The confidence level is determined using an extended fit to signal plus background hypothesis in the full Λ_c^+ mass range. The expected upper limit from CLs method at 90% CL for a branching ratio with respect to the normalization channel is used as a figure of merit during the final cut optimization phase. This final optimization is based on three variables: a BDT discriminant, a proton identification probability for a proton and a minimum of muon identification probabilities for the two muons.

Apart from the combinatorial background which is estimated by the fit to signal sidebands, the peaking background falling in the *signal* region has to be taken into account. The two main types of peaking backgrounds are expected. One source comes from the resonant decays of Λ_c^+ with the same final state as the signal. The second source is from the decays with a proton and two other particles misidentified as muons. The only relevant source of the latter is the $\Lambda_c^+ \to p\pi^+\pi^-$ decay. Other contributions from channels with misidentified particles are estimated to be negligible.

A blind analysis method was employed. The *signal* region in $p\mu^+\mu^-$ invariant mass $\pm 30\,\text{MeV}/c^2$ around the nominal Λ_c^+ mass was excluded from the initial stage of the analysis. Only candidates with dimuon mass $\pm 40\,\text{MeV}/c^2$ around nominal ϕ mass were unblinded irrespective of the $p\mu^+\mu^-$ invariant mass value.

5 Selection

5.1 Preselection and Stripping

The preselection consists of four sets of requirements: the trigger, stripping, rectangular cuts and initial MVA discrimination referred to as BDT1. They are described in the following chapters.

5.1.1 Trigger and stripping

An optimization of the trigger lines compositions for L0, HLT1 and HLT2 is performed. We consider all physics lines used during a given year (excluding technical lines, prescaled lines etc.). First, the L0 trigger is optimized. The most efficient L0 lines are chosen. Selecting the two most efficient trigger lines (L0MuonDecision and L0DiMuonDecision) is saturating the L0 efficiency, i.e. the inclusion of other trigger lines has only a few percent effect on the total L0 efficiency. The advantage of limiting a set of L0 to muonic lines is that they are very well simulated ensuring good Data/MC agreement.

The same strategy is applied to the selection of HLT1 and HLT2 lines, where only the minimal number of lines with the highest efficiency is kept. This way one can make a full use of the same final state of signal and normalization channel. The final lists of the selected lines are collected in Table 6 and the resulting efficiencies for trigger levels are presented in Table 7. More details of the trgigger optimization can be found in Sec. A. The two lines Hlt2RareCharmD2KMuMuOSDecision and Hlt2RareCharmD2PiMuMuOSDecision with the lower mass hypothesis are used. Their distortions are shown in Sec. B.

The possible biases introduced by the trigger are checked for three variables: Λ_c^+ invariant mass, dimuon invariant mass and proton angle in the rest frame of Λ_c^+ . The efficiency curves show that the chosen composition of trigger lines does not cut out any range of the three variables considered.

Table 6: Summary of trigger lines chosen for the analysis. This common set of trigger lines is found to be optimal for all datasets: 2016, 2017 and 2018.

Level	Lines
L0	`L0MuonDecision`
	`L0DiMuonDecision`
Hlt1	`Hlt1TwoTrackMVALooseDecision`
	`Hlt1TrackMVADecision`
	`Hlt1TrackMuonDecision`
Hlt2	`Hlt2RareCharmD2KMuMuOSDecision`
	`Hlt2ExoticaDisplDiMuonNoPointDecision`
	`Hlt2RareCharmD2PiMuMuOSDecision`
	`Hlt2ExoticaDisplDiMuonDecision`

The candidates are selected by the stripping line named Lc23MuLc2pmumuLine. The requirements of that line are listed in Table 8.

Table 7: The efficiencies of signal at L0, HLT1 and HLT2 levels for trigger lines selected for the analysis. The efficiencies are determined for MC offline-like selected (slightly relaxed selection criteria compared to final optimized selection) signal sample for a mixture of prompt and secondary Λ_c^+ production.

Level	Efficiency [%]		
	2016	2017	2018
L0	61.3 ± 0.7	71.9 ± 0.7	64.2 ± 0.7
HLT1	93.9 ± 0.4	93.7 ± 0.4	94.2 ± 0.3
HLT2	56.0 ± 0.8	95.6 ± 0.3	95.2 ± 0.3
Total	32.2 ± 0.6	64.4 ± 0.7	57.6 ± 0.7

Table 8: The requirements of the stripping line Lc23MuLc2pmumuLine. Muon candidates (StdLooseMuons) are required to satisfy the $IsMuon$ requirement.

Condition	$\mu^\pm$ and p
p_T	> 300 MeV/c
Track χ^2/ndf	< 4
IP χ^2/ndf	> 9
Ghost probability	< 0.4
PID $\mu^\pm$	(PIDmu - PIDpi)> -5 and (PIDmu - PIDK) > -5
PID p	(PIDp - PIDpi)> 5 and (PIDp - PIDK) > 0
Condition	Λ_c^+
$\lvert m_{\Lambda_c^+} - m(p\mu^+\mu^-)\rvert$	< 200 MeV/c
Vertex χ^2	< 15
IP χ^2	< 100
$c\tau$	> 70 μm

5.1.2 Rectangular cuts and initial MVA discrimination

Apart from the trigger and stripping requirements, the preselection consists of two types of cuts: i) the rectangular cuts for signal and normalization channel listed in Table 9 and ii) a cut on initial BDT (BDT1) described in Sec. 5.2.1.

In the case of the rectangular cuts, the $m_{\mu^+\mu^-} > 211.32$ and $m_{\mu^+\mu^-} > 1348.13$ MeV/c^2 cut for dimuon mass is set according to the kinematical limit of phase space. The simulated distribution of dimuon invariant mass after stripping is shown in Fig.25. The restriction on

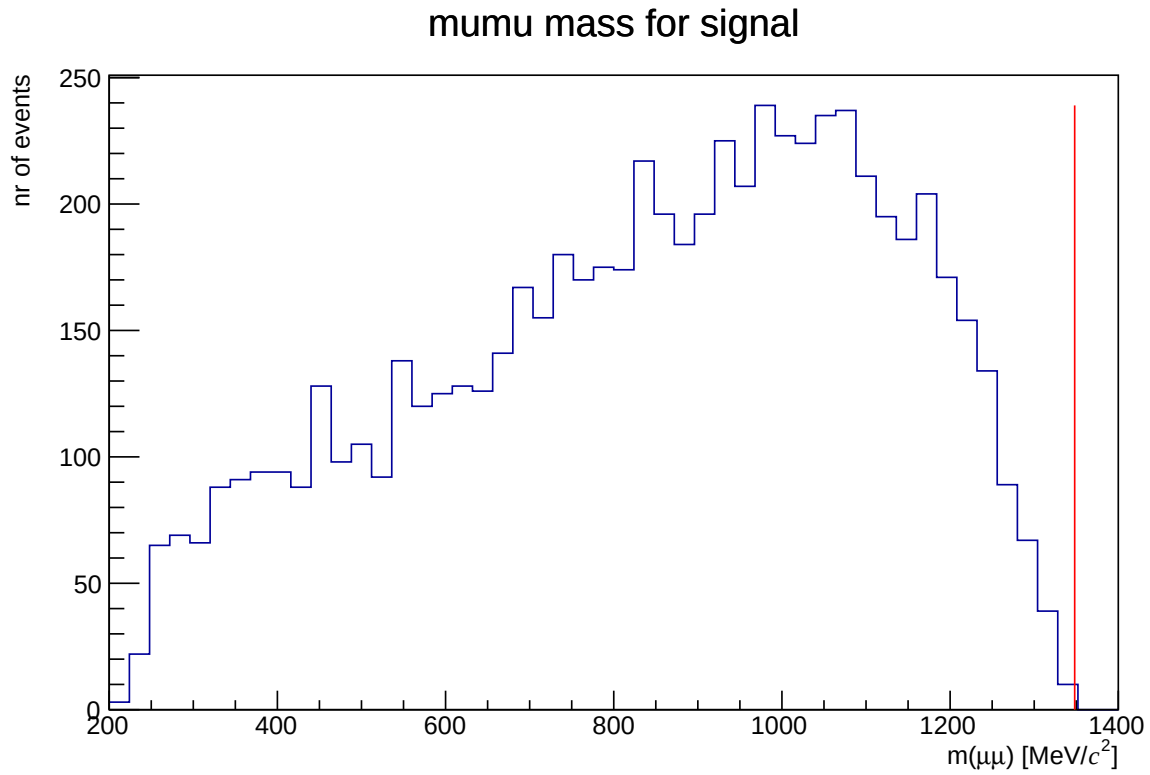

Figure 25: The simulated distributions of dimuon mass for the signal after stripping. The red line indicates the 1348.13 MeV/c^2 cut.

proton momentum is to match the RICH identification momentum range. In the case of signal selection the resonant region between 507.86 MeV/c^2 and 1059.45 MeV/c^2 of dimuon mass is removed as indicated in Table 4. In the case of normalization channel the dimuon mass is required to fall into ± 40 MeV/c^2 around ϕ mass (Fig. 26). The efficiency of ϕ mass window cut for the normalization channel after stripping is 97 %.

5.2 Multi-Variate Analysis

For the BDT training the TMVA package is employed. Simulation is used as the proxy for the signal while background is taken from the sidebands of the data. The definition of sidebands ranges are listed in Table 10 and illustrated in Fig. 27. The optimized internal parameters of BDT method are listed in Table 11.

For the training of the classifiers a k-Folding technique is used [89]. This technique allows us to use the full data set in an unbiased way. To cancel any influence of varying running conditions (e.g. different trigger conditions, magnet polarities) the ordering of the data set is

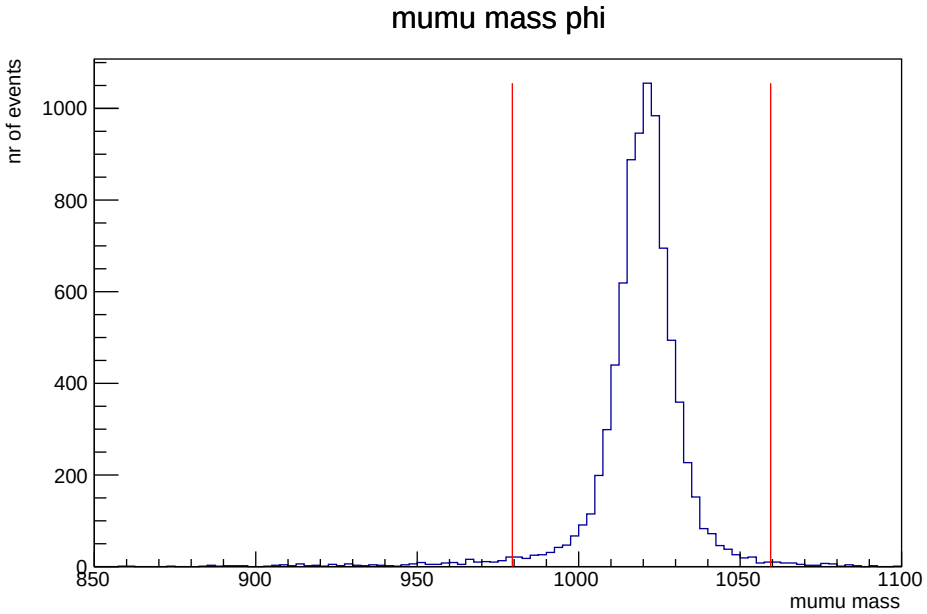

Figure 26: The simulated distributions of dimuon mass for the normalization channel after stripping. The red lines indicate $\pm 40\,\mathrm{MeV}/c^2$ around the ϕ mass.

Table 9: The rectangular cuts of the preselection.

Common cuts
$m_{\mu^+\mu^-} > 211.32$ MeV/c^2
$m_{\mu^+\mu^-} < 1348.13$ MeV/c^2
5 GeV/c^2 $< p_{proton} <$ 150 GeV/c^2
Signal channel
$m_{\mu^+\mu^-} < 507.86$ MeV/c^2 or $m_{\mu^+\mu^-} > 1059.45$ MeV/c^2
Normalization channel
$\lvert m_{\mu^+\mu^-} - m_\phi \rvert < 40$ MeV/c^2

Table 10: The definition of lower and upper limit of invariant mass distributions around Λ_c^+ mass as well as ranges of left and right signal sideband. The sidebands are used to estimate the combinatorial background in the signal region needed for optimization of selection cuts. Final results i.e. upper limits are determined by the extended fit to the full invariant mass.

Range	Low [MeV]	High [MeV]
full range	m_{Λ_c} - 140	m_{Λ_c} + 140
left sideband	m_{Λ_c} - 140	m_{Λ_c} - 35
right sideband	m_{Λ_c} + 35	m_{Λ_c} + 140

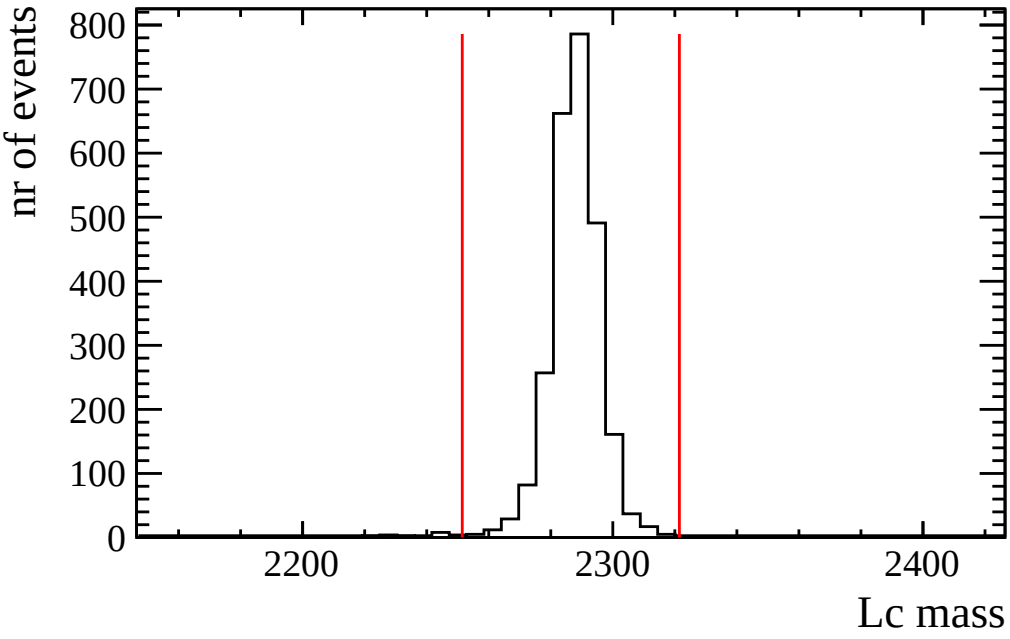

Figure 27: The illustration of the choice of sideband regions. The distribution of Λ_c^+ invariant mass for simulated signal after stripping is shown as histogram.

randomized and divided in $k = 10$ samples of equal size, both for the full background sample and for the full MC signal.

The BDT discrimination is done in two steps. The initial BDT (BDT1) employed variables of Λ_c^+ only. The BDT1 discrimination is applied to the data and to all simulated samples as one of the preselection cuts as described in Sec. 5.1.2. The aim is twofold: i) to obtain a good signal to combinatorial background ratio for normalization channel, followed by checking the agreement between MC and DATA and to determine appropriate reweighting for application to all MC samples, and ii) to construct PDF distributions to perform final optimization by means of pseudoexperiments.

The second BDT (BDT2) includes a full set of BDT variables and is trained using the preselected and reweighted MC sample of $\Lambda_c^+ \to p(\mu^+\mu^-)$ as signal proxy with an extended set of input variables by the ones of the decay products. Owing to the selection of the same set of trigger lines for all years 2016-2018, the distributions of input variables used in BDT are satisfactorily similar, as can be seen in Fig. 68 for MC signal and Fig. 69 for data. Therefore a common BDT training is applied by merging samples from all years to form a single MC sample representing signal and a single sideband sample representing background. An alternative approach with separate BDT trainings for individual years was checked as well. It turned out that the common training gives a slightly better performance.

5.2.1 Initial MVA discrimination

After passing the stripping phase, trigger and rectangular preselection cuts, the mass peak region of normalization channel is still dominated by the background. To suppress the background further down, the BDT1 discrimination based on a limited set of variables is employed. The following seven variables related to Λ_c^+ are chosen for initial BDT1 discrimination:

- $\log(FD)$- flight distance between the production and decay points (log_Lc_FD_OWNPV),

Table 11: The internal parameters of the BDT method used for the training.

Parameter	Value
NTrees	850
MaxDepth	3
MinNodeSize	2.5%
nCuts	20
BoostType	AdaBoost
PruneMethod	nopruning

- $\log(\chi^2)$ of flight distance (log_Lc_FDCHI2_OWNPV),
- transformed decay time - $T = \exp(-1000 \cdot \tau/\text{ns})$ (Lc_Transformed_TAU),
- $\log(IP)$ - impact parameter with respect to PV (log_Lc_IP_OWNPV),
- $\log(\chi^2_{IP} - \chi^2)$ of IP defined as the difference in χ^2 when the $Lambda_c^+$ candidate is included and excluded from the PV fit (log_Lc_IPCHI2_OWNPV),
- $\log(\chi^2_{DTF})$: the χ^2 of the DecayTreeFitter vertex fit (log_Lc_ENDVERTEX_CHI2),
- p_T - transverse momentum of Λ_c^+ (Lc_PT).

The names in the bracket correspond to the names in ntuples that are presented in figures and tables.

The Run1 analysis showed that the prompt Λ_c^+ production is more efficient for BDT discrimination, the secondary Λ_c^+ production being more similar to background as Λ_c^+ does not point back to primary vertex. The MVA training using a mixture of prompt and secondary components for signal ends up with the suppression of the secondary component and with an overall signal to background ratio worse compared to training on prompt component only. Therefore the simulated sample representing a signal during the BDT training is restricted to prompt Λ_c^+'s. The rate of the secondary production of various steps of the selection is shown in Appendix C.

The background is taken from the data sidebands, [2140, $m_{\Lambda_c} - 35$] MeV^2 and [$m_{\Lambda_c} + 35$, 2430] MeV^2, where $m_{\Lambda_c} = 2286.46$ MeV^2. The BDT distributions for training and test subsamples for the 10 folds are similar. They are presented in Fig. 28 for one of the folds. The ranking of BDT1 input variables are listed in Table 12. The Receiver Operating Characteristic (ROC) curves for 10 folds are shown in Fig. 29. They are nearly identical with AUC$\cong$ 0.92. The distributions of the BDT discriminant for the simulated signal (prompt and secondary contributions included) are presented in Fig. 30. The preselection cut is set at BDT1>-0.1. It accepts the majority of prompt Λ_c^+'s.

5.2.2 Final MVA discrimination

For the second BDT (BDT2) training the samples used for BDT1 training are reduced further by BDT1> -0.1 cut. The set of input parameters is extended to include the parameters of Λ_c^+ decay products. The final multivariate variable is constructed using the following fifteen input variables:

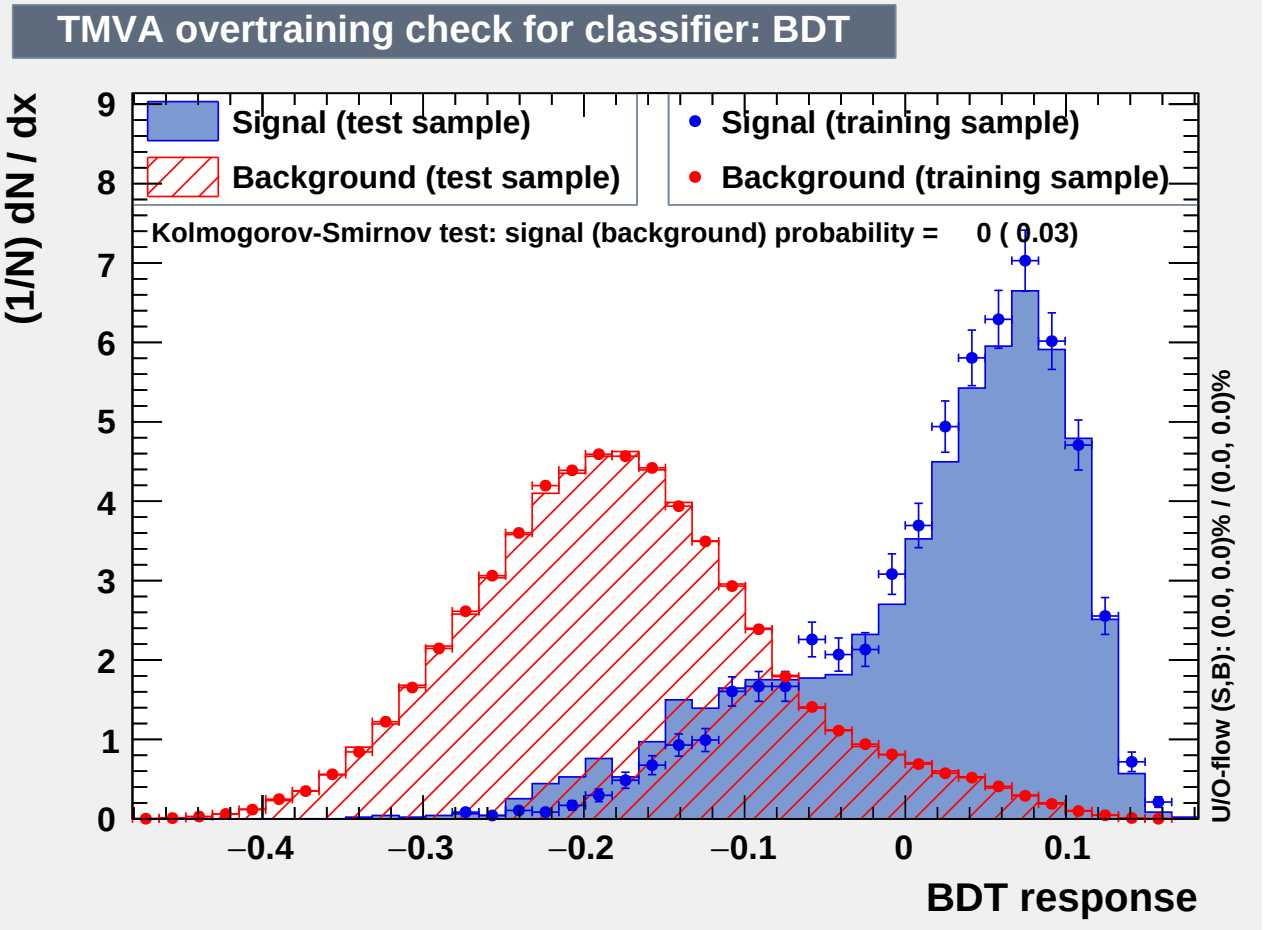

Figure 28: The distributions of BDT1 variable for one of the folds. The signal distribution corresponds to MC prompt production which is used for signal proxy in training.

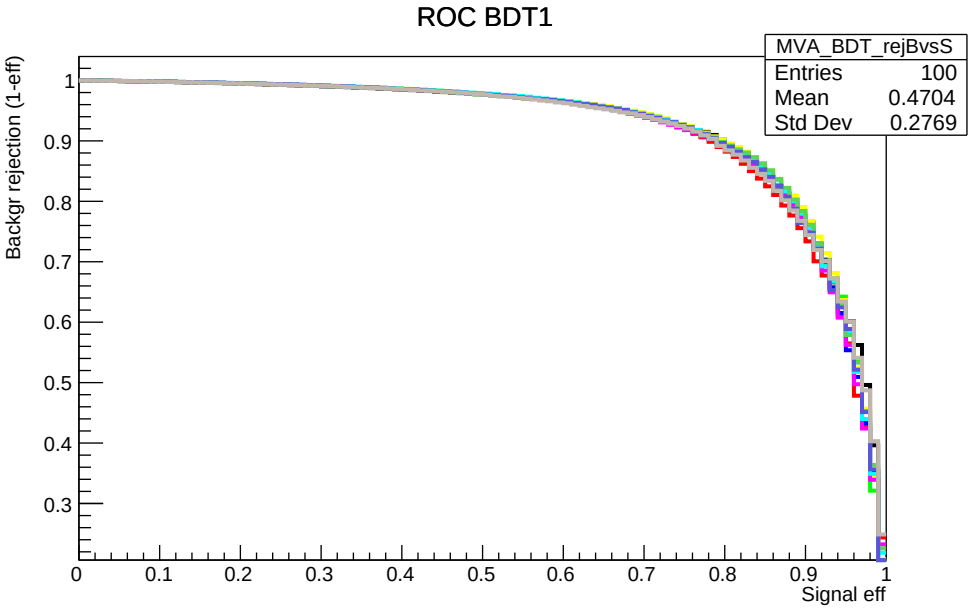

Figure 29: The comparison of ROC curves for BDT1 variable for ten folds.

Table 12: The ranking of the BDT1 variables.

Rank	Variable	Separation
1	log_Lc_IP_OWNPV	4.139e-01
2	log_Lc_IPCHI2_OWNPV	3.904e-01
3	Lc_Transformed_TAU	2.609e-01
4	Lc_PT	1.909e-01
5	log_Lc_FD_OWNPV	9.038e-02
6	log_Lc_ENDVERTEX_CHI2	7.424e-02
7	log_Lc_FDCHI2_OWNPV	5.228e-02

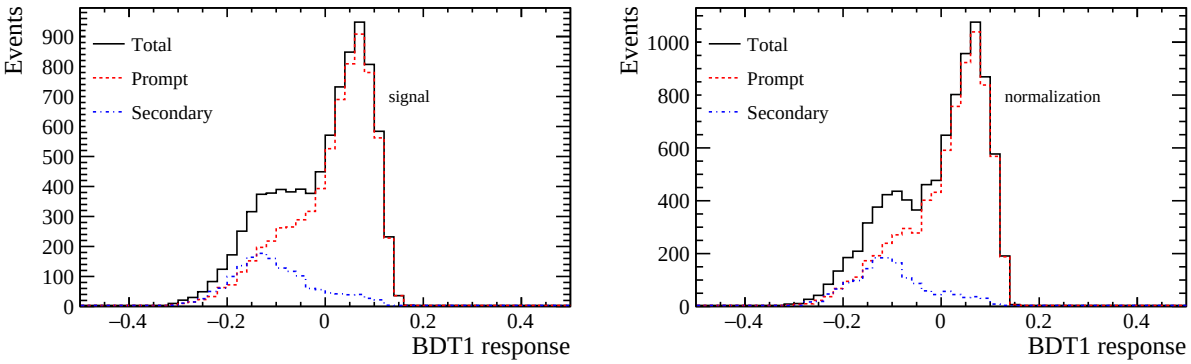

Figure 30: The distribution of BDT1 variable for simulated samples after stripping: signal (left) and normalization channel (right). The components corresponding to various production types of Λ_c^+ are shown.

- the seven variables for Λ_c^+ baryon used in BDT1 as described in Sec.5.2.1.
- variables for decay products: $p/\mu^+/\mu^-$
  - minimum of χ^2_{IP} of p, μ^+, μ^- with respect to PV (1 variable) (log_minimum_IPCHI2_OWNPV),
  - transverse momenta (3 variables) (p_PT, mu1_PT, mu2_PT),
- isolation variables
  - Λ_c^+ isolation - CDF isolation (1 variable, Ref. [90]) (Lc_relinfo_BSMUMUCDFISO),
  - isolations for p, μ^+ and μ^- (3 variables) (Lc_relinfo_BsMuMuTrackIsomu1_BSMUMUTRACKPLUSISO, Lc_relinfo_BsMuMuTrackIsomu2_BSMUMUTRACKPLUSISO, Lc_relinfo_BsMuMuTrackIsop_BSMUMUTRACKPLUSISO).

The names in the bracket correspond to the names in ntuples that are presented in figures and tables. The track isolation variables are described in Appendix. F. The CDF isolation variable was first introduced by CDF Collaboration in Ref. [90]. The distributions of the BDT input variables for signal and background events after passing stripping, trigger and preselection are shown in Fig. 67 in Appendix D. The comparison of input variables for 2016,

2017 and 2018 data are shown in Fig. 68 for signal and in Fig. 69 for background. The ranking of the BDT2 input variables are listed in Table 13. The isolation variables are high in the ranking. The result of training for one of the folds (the distributions for 10 folds are similar)

Table 13: The ranking of the BDT2 variables.

Rank	Variable	Separation
1	log_Lc_IPCHI2_OWNPV	1.610e-01
2	log_Lc_IP_OWNPV	1.601e-01
3	Lc_relinfo_BsMuMuTrackIsomu2_BSMUMUTRACKPLUSISO	1.470e-01
4	Lc_relinfo_BsMuMuTrackIsomu1_BSMUMUTRACKPLUSISO	1.454e-01
5	Lc_relinfo_BsMuMuTrackIsop_BSMUMUTRACKPLUSISO	1.426e-01
6	p_PT	8.030e-02
7	Lc_Transformed_TAU	7.435e-02
8	Lc_relinfo_BSMUMUCDFISO	7.334e-02
9	Lc_PT	3.489e-02
10	log_Lc_FDCHI2_OWNPV	2.530e-02
11	log_Lc_FD_OWNPV	1.636e-02
12	log_Lc_ENDVERTEX_CHI2	1.541e-02
13	mu1_PT	1.398e-02
14	log_minimum_IPCHI2_OWNPV	1.362e-02
15	mu2_PT	8.710e-03

are presented in Fig. 31. The training and test samples do not match perfectly however such small overtraining should not lead to significant suboptimal behavior. In any case, the k-folding technique ensures that no bias is introduced. The corresponding ROC curves are shown in Fig. 32. The are similar with average AUC$\cong=$ 0.88.

To compare the performance of individual folds the efficiencies for cuts used in the preselection, BDT1> -0.1 and for BDT2> -0.03 cut are presented in Fig. 33 for signal samples and in Fig. 34 for background (data sidebands). One can see that they agree well within the statistical uncertainties.

5.3 Optimization of final selection

The final selection is performed by cutting in 3 variables: BDT2 discriminant, $ProbNNp(p)$ and minimum of $ProbNNmu(\mu^{\pm})$. The three-dimensional optimization in these variables is performed using the ToyMC technique and by taking an expected upper limit for a branching ratio at 90% C.L. as a Figure of Merit (FOM), where the minimum FOM point is searched for. To calculate the value of FOM for the cuts in the three variables one needs to determine the corresponding yield for background (combinatorial and peaking background) and yield for normalization channel. The following procedure is used: the three dimensional PDF in BDT2, $ProbNNp(p)$ and minimum of $ProbNNmu(\mu^{\pm})$ is prepared for the sidebands using the data samples after preselection. Using this PDF a large dataset of 100 thousand events is generated. For each set of cuts the expected number of sideband events in data is estimated by scaling the initial number of events according to the reduction factor after the application of cuts to the generated dataset. In the case of the normalization channel the initial yield is determined from data after the preselection and the expected number of events after applying cuts is estimated

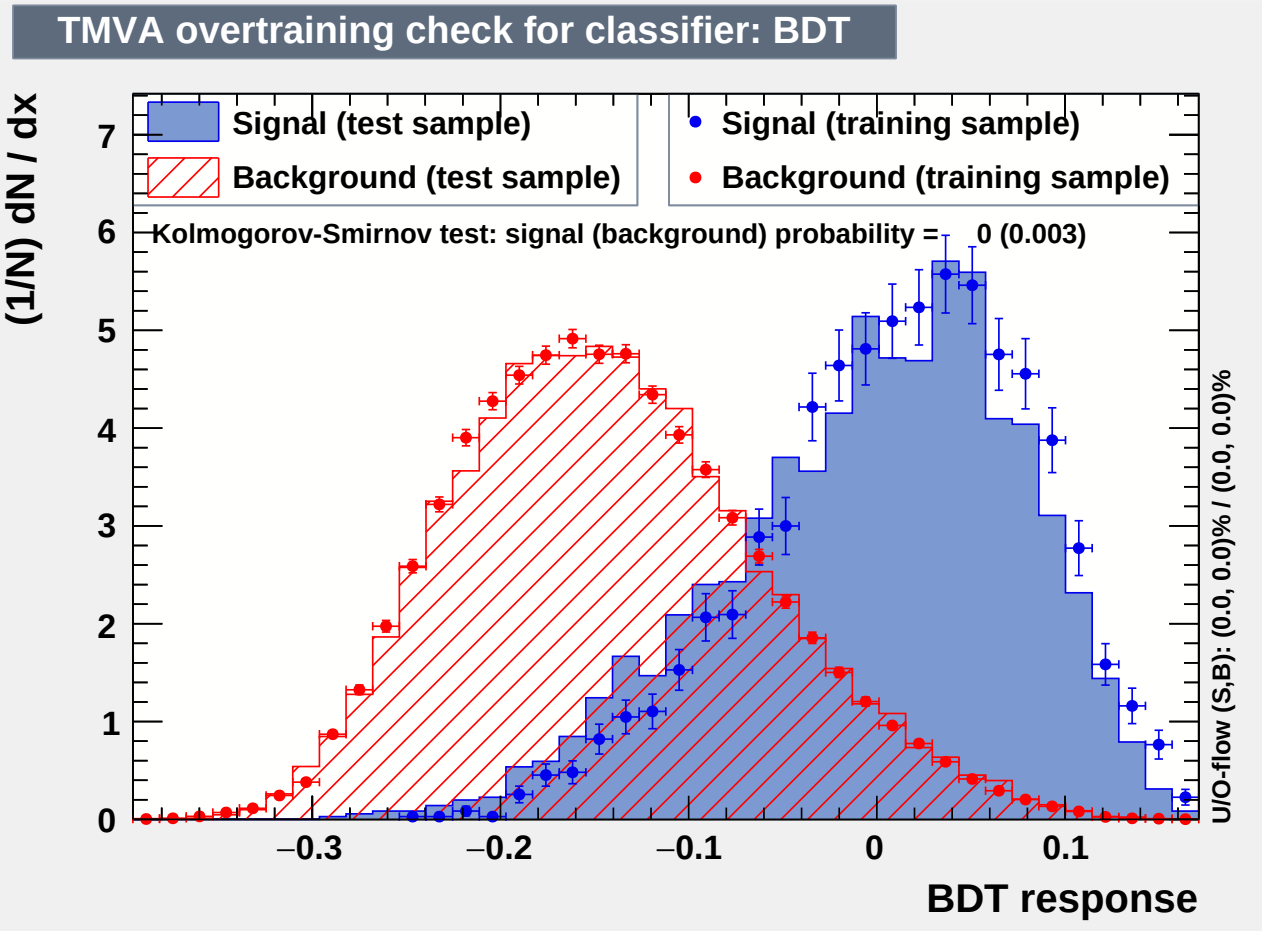

Figure 31: The distributions of BDT2 variable for one of the folds. The signal distribution corresponds to MC prompt production.

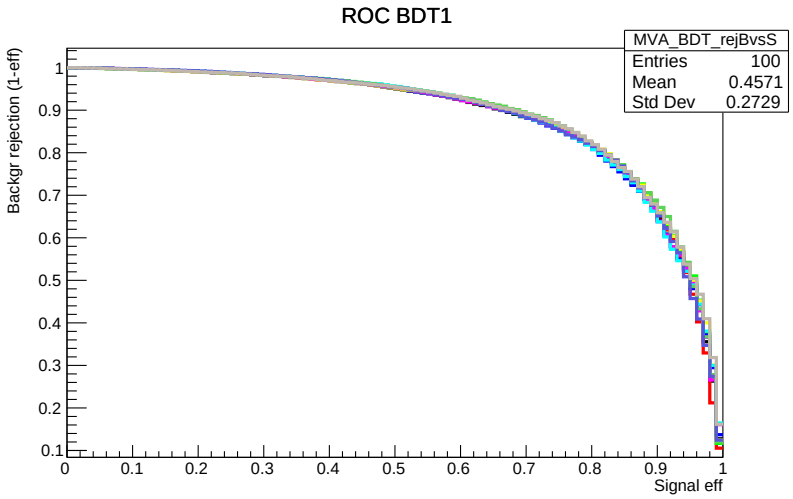

Figure 32: The comparison of ROC curves for BDT2 variable for ten folds.

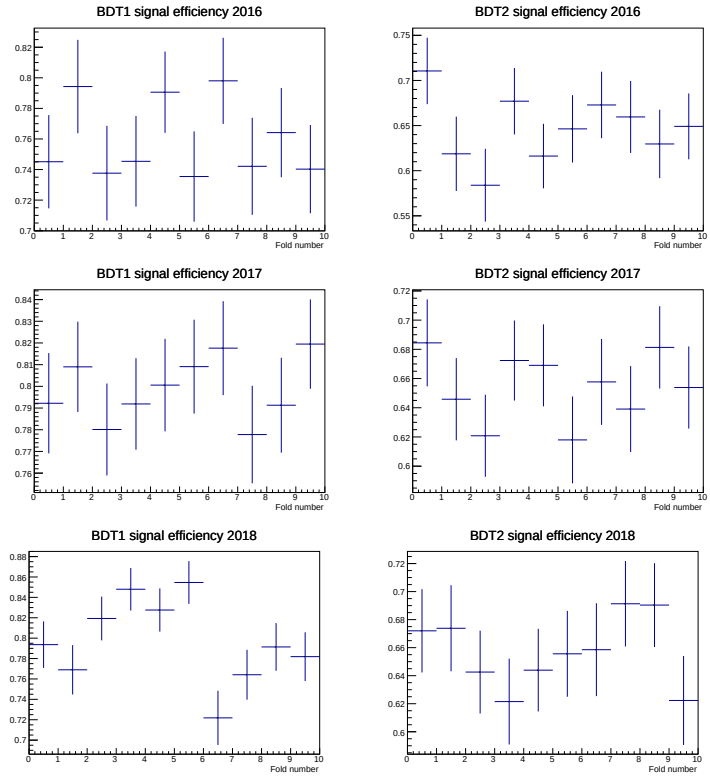

Figure 33: The efficiencies of ten folds for signal prompt Λ_c^+ production for individual years of data taking. Left plots correspond to BDT1> -0.1 cut, right plots correspond to BDT2> -0.03 cut. No PID requirements are imposed.

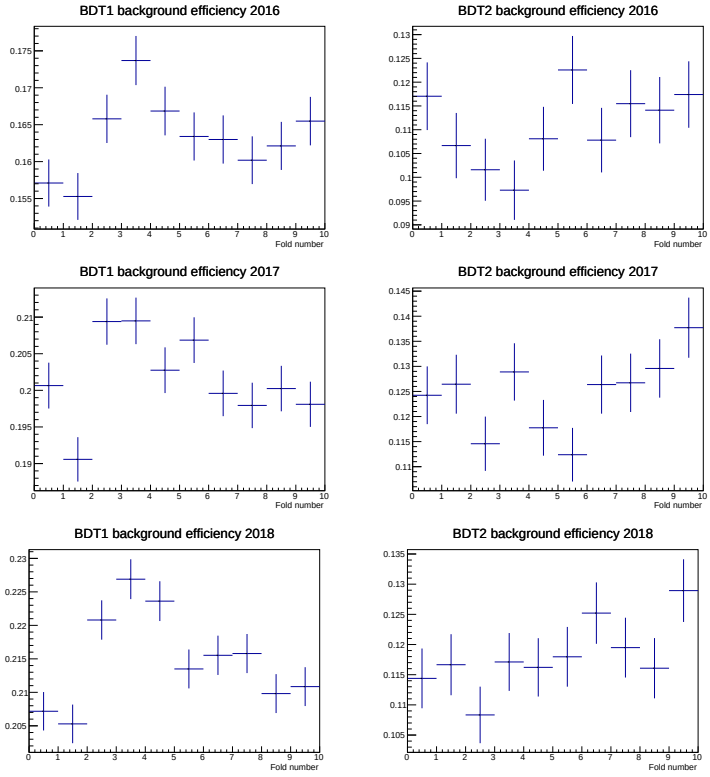

Figure 34: The efficiencies of ten folds for background (data sidebands) for individual years of data taking. Left plots correspond to BDT1> -0.1 cut, right plots correspond to BDT2> -0.03 cut. No PID requirements are imposed.

using PID resampled and reweighted MC samples. This initial yield determined from the data is scaled down according to the reduction factor determined for the MC sample i.e. scaled by the ratio of events passing the selection for the given (BDT2, ProbNNp, ProbNNmu) cuts to the number of events after the preselection. Finally the number of $\Lambda_c^+ \to p\pi^+\pi^-$ background is estimated relative to the number of normalization channel events as described in Sec. 7.3. The ratios of efficiencies needed for FOM calculation: normalization channel to signal and normalization channel to $\Lambda_c^+ \to p\pi^+\pi^-$ background are recalculated for each set of the three cuts.

For each set of cuts, 400 toy experiments are performed. In each pseudo-experiment the upper limit on branching ratio with respect to normalization channel is determined using the binned CLs method (six mass bins). The average upper limit of BR over 400 toy experiments is taken as the FOM value.

The FOM minimum is determined scanning on a large computing cluster over the 3D grid of rectangular cuts. The first wide bins are used to approximately locate the position of the minimum. Then in the area of the minimum, a finer grid is used to precisely determine the minimum. For the scan in a finer grid area the ratio of efficiencies is fixed to reduce the influence of additional fluctuations and limit the computing power needs. The value is fixed at the approximate minimum found in the wide scan. This is justified as the variation of the efficiency ratio in this region is relatively small (Fig. 35).

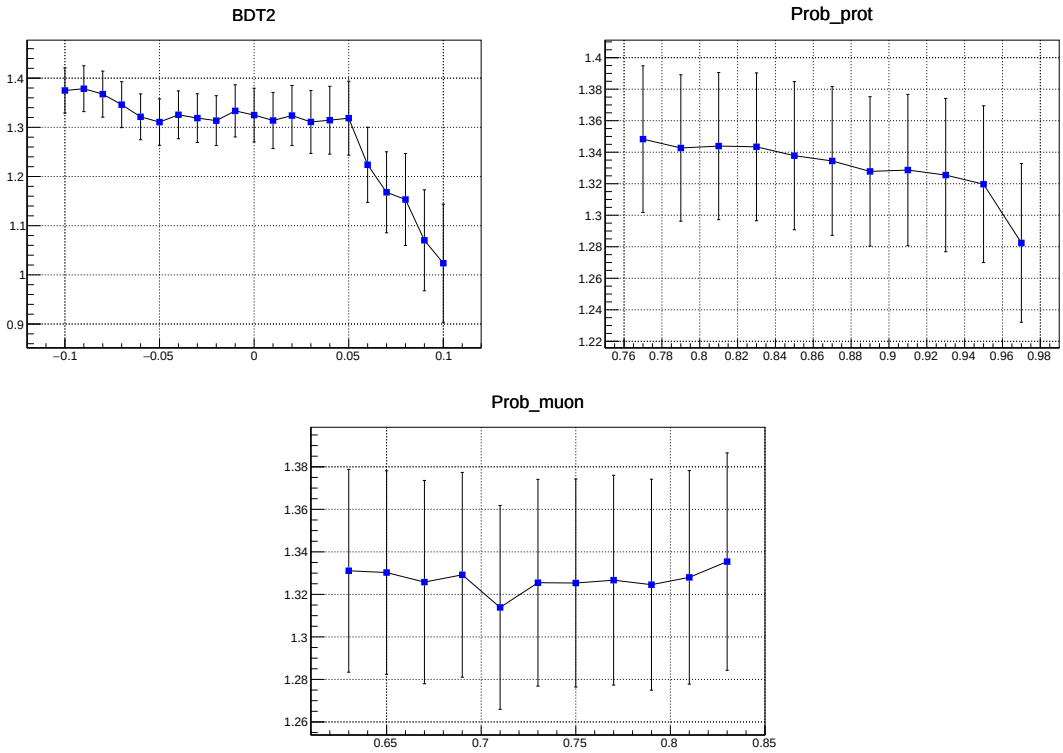

Figure 35: Variation of the efficiency ratio of normalization channel to signal channel with the BDT2, ProbNNp and ProbNNmu cuts.

The optimal cuts are listed in Table 14. The 2D projections for ProbNNp and ProbNNmu at optimal BDT2 value are shown in Fig. 36 for the wide bin scan and in Fig. 37 for the narrow bin scan. One can see that the variation of the FOM around minimum is relatively small.

Table 14: Optimal values of cuts for upper limit determination

Variable	Condition
BDT2	> -0.03
$ProbNNp(p)$	> 0.91
minimum $ProbNNmu(\mu^{\pm})$	> 0.68

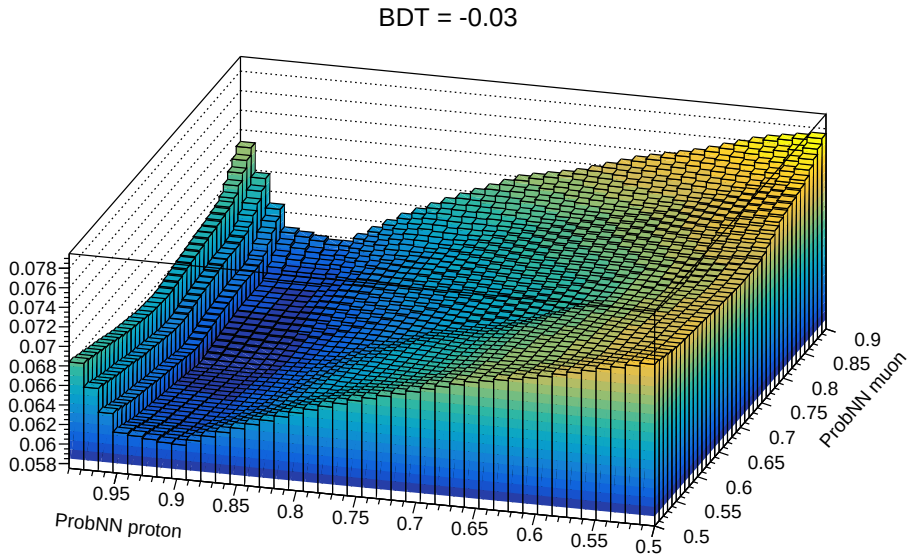

Figure 36: Result from scan over wide bins. The two-dimensional projections ($ProbNNp(p)$, $ProbNNmu(\mu^{\pm})$ around the FOM minimum for BDT2>-0.03 cut.

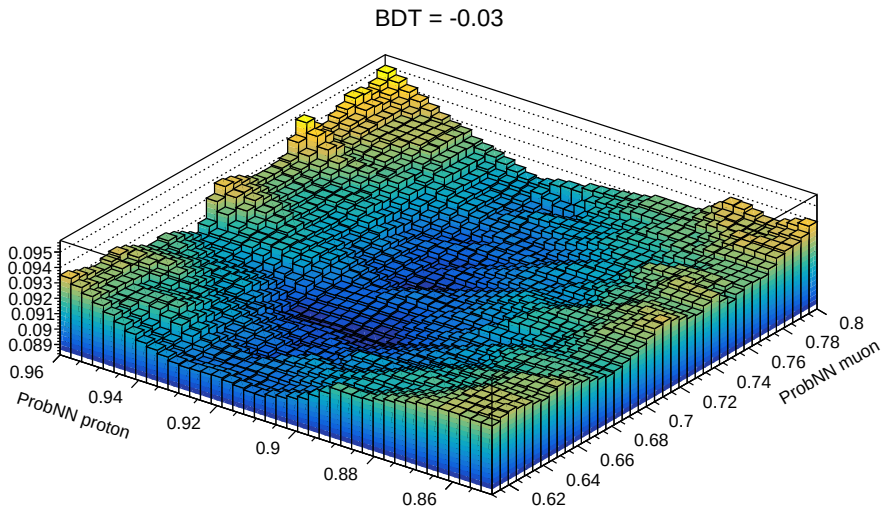

Figure 37: Result from scan over narrow bins in the area of minimum. The two-dimensional projections ($ProbNNp(p)$, $ProbNNmu(\mu^{\pm})$ around the FOM minimum for BDT2>-0.03 cut.

6 Simulation corrections

6.1 MC matching

For the MC truth matching the Background Category (BKGCAT) is required to be 0 or 50 for the signal channel and 10 or 50 for the normalization channel. The events with BKGCAT=50 correspond to a relatively hard radiation in the final state. Invariant mass distribution for both 10 and 50 BKGCAT for signal channel is illustrated in Fig. 38. The radiation effects

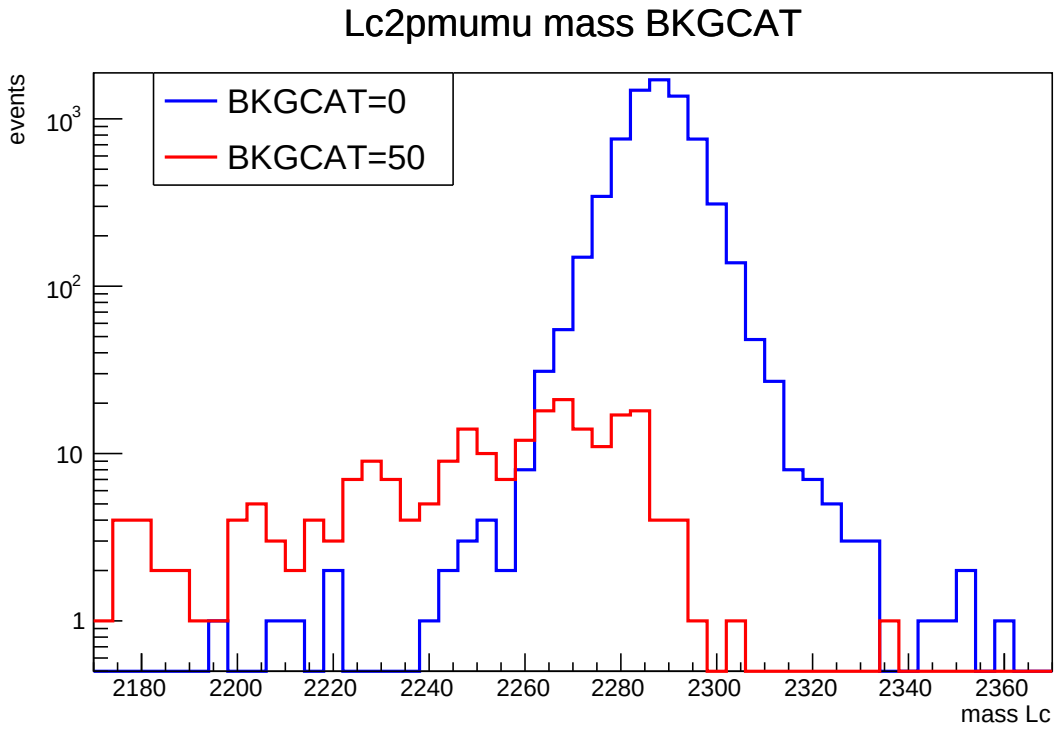

Figure 38: Invariant mass distributions after stripping for simulated signal for BKGCAT=0 and BKGCAT=50.

originates from the dimuon system. The distributions of dimuon mass and Λ_c^+ mass for the normalization channel are shown in Fig. 39.

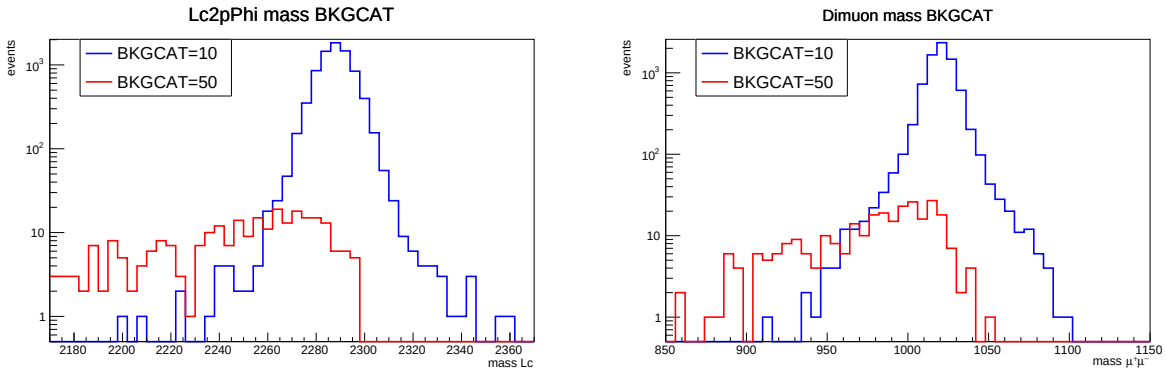

Figure 39: Invariant mass distributions after stripping for BKGCAT=10 and BKGCAT=50 for normalization channel for Λ_c^+ mass (left) and for ϕ mass (right).

6.2 Reweighting

To ensure a proper agreement between the data and simulation, MC samples are reweigthed. The adaptive reweigthing method is used. The weights to correct for the observed differences between the data and MC are derived sequentially because of potential correlations between the variables, with the $(N-1)^{th}$ weight being applied before deriving the N^{th} weight.

The reweighting is determined for the normalization channel using distributions for the preselected MC samples and for the data from the sPlot method [91]. The invariant mass plot used in sPlot for the normalization channel after the preselection including BDT1>-0.1 cut is shown in Fig. 40. The comparison of BDT2 distributions between the simulation and

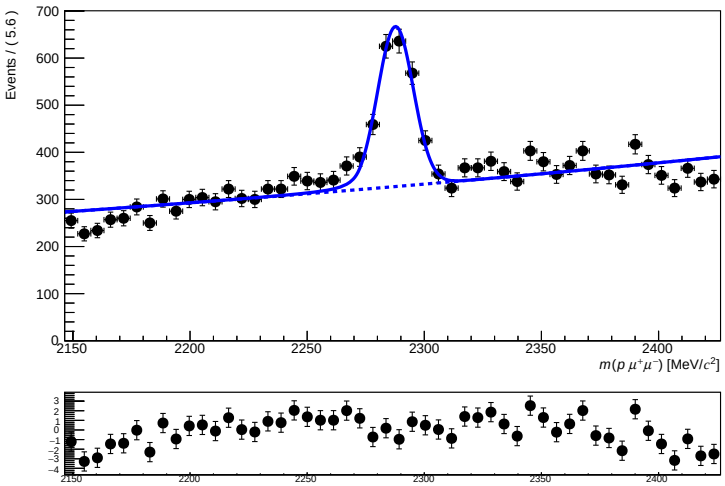

Figure 40: The invariant mass distributions for data after preselection of normalization channel. Solid line is the result of the fit to Crystal Ball (CB) shape on exponential background. The dashed line represents the background component.

data is presented in Fig. 42. A small shift between the data and MC is observed (unweighted MC distribution being shifted right with respect to the data). This difference comes from non perfect matching of BDT input variables between the data and MC. To correct for this shift, the two variables showing the largest differences are chosen for reweighting, the detector track occupancy, n_{Tracks}, and the Λ_c^+ transverse momentum p_T. Their distributions before and after the reweighting are shown in Fig. 41. One can see that after the reweighting the systematic shift in BDT2 distributions is corrected (Fig. 42). The result of the reweighting for all BDT2 input variables is shown in Appendix E and for PID variables in Fig. 44.

It can be concluded that by correcting MC using the reweighting method, a satisfactory agreement is achieved for all variables crucial for the analysis i.e. BDT2 input variables, BDT2 response and PID variables. The event weights determined for the normalization channel are then used to weight all other MC samples.

It can be noted that the efficiencies estimated with MC for a given cut on BDT2 are not used directly for the branching ratio estimation or upper limit determination. Only the ratios of efficiencies are used where most effects which result from non-perfect modelling in the simulation cancel out to a large extent. It can be seen in Fig 43 (right) that the MC distributions of BDT2 for the signal and normalization channel are very similar. This indicates that the same behavior is expected for the data ensuring that the ratios determined for MC give reliable values for the data.

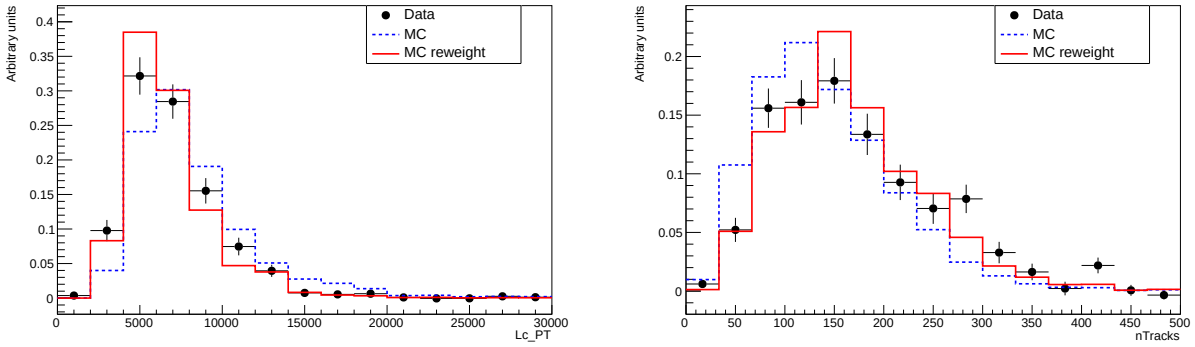

Figure 41: The comparison of simulated distributions (before and after reweighting) to data for normalization channel after preselection for two variables used for Adaptive Reweighting: transverse momentum of Λ_c^+ (left) and nTracks (right). The distributions for data are obtained using sPlot method.

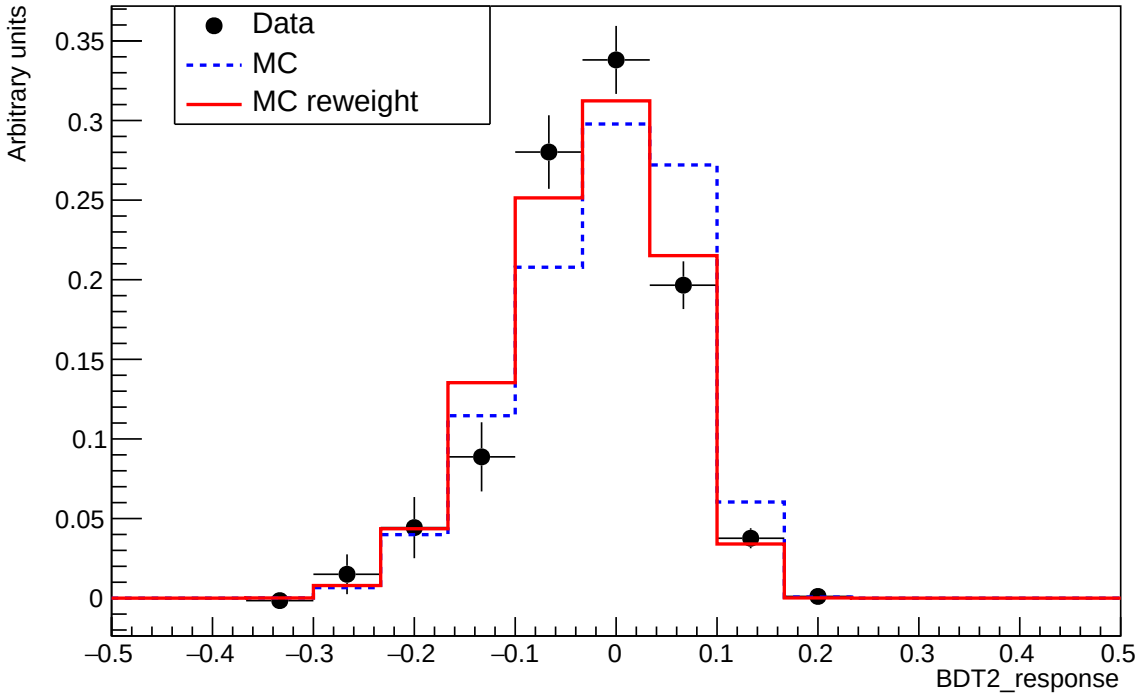

Figure 42: The comparison of BDT2 distributions for data and MC before and after reweighting for the normalization channel after preselection. The distribution for data is obtained using sPlot method.

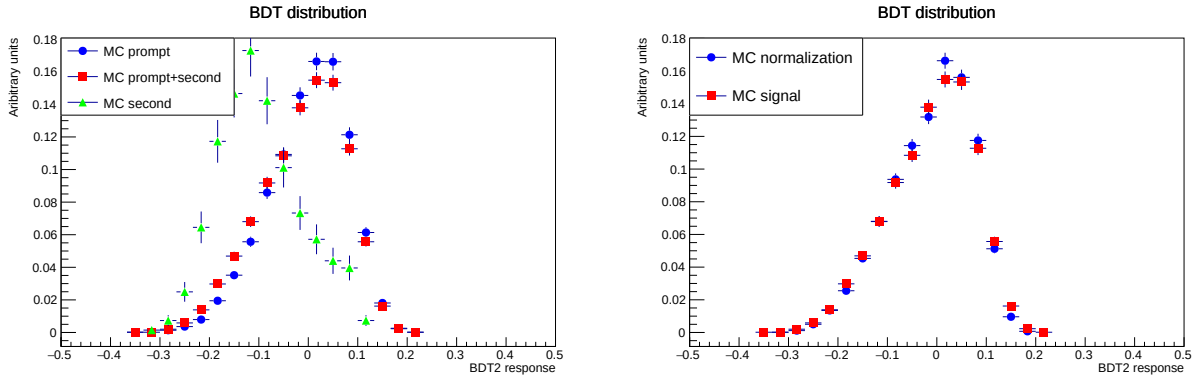

Figure 43: The comparison of BDT2 distributions for MC samples after preselection and trigger. Left figure corresponds to signal. The prompt and secondary production components are shown. In right figure the comparison between the signal and normalization channels is shown. All distributions are normalized to unity.

6.3 PID calibration

The PID probabilities $ProbNN$'s are not modeled perfectly in the simulation. Therefore a calibration procedure using PIDCalib package is employed for all simulated samples. The MC resampling method is chosen. The corrected $ProbNN$ for proton and muons are drawn from the distributions determined from the data using dedicated tuning. The distributions depend on p_T and η of the particle and on charged track multiplicity in an event.

The corrected $ProbNNp$ and $ProbNNmu$ values for Λ_c^+ secondaries are consequently used in the analysis instead of the originally simulated ones. The corrected $ProbNN$ distributions for the simulation are compared to data in Fig. 44.

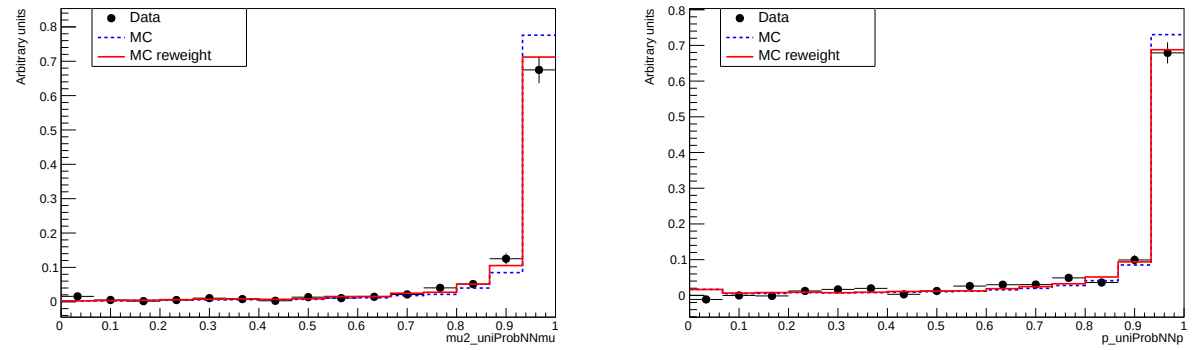

Figure 44: The $ProbNN$ distributions of normalization channel for data (black dots), for reweighted MC (red line) and for MC before reweighting (dashed blue line): $ProbNN$ for muon (left) and $ProbNN$ for proton (right). The distribution for data is obtained using sPlot method for the sum of 2016, 2017 and 2018 samples. The MC corresponds to prompt+secondary mixture of Λ_c^+ production. The $ProbNN$ distributions for MC are resampled.

6.4 Decay model correction for background decay $\Lambda_c^+ \to p\pi^+\pi^-$

The sample for $\Lambda_c^+ \to p\pi^+\pi^-$ was generated according to the phase space model. The actual decay model was determined in another LHCb analysis [92]. Using the corrected distribution from Dalitz plot, the sample simulated according to phase space is weighed to reflect the

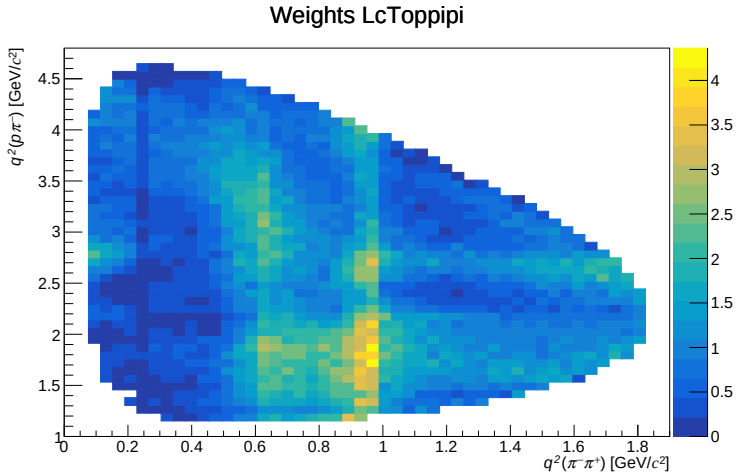

Figure 45: The distribution of weights used to correct simulated sample of $\Lambda_c^+ \to p\pi^+\pi^-$.

measured distribution. The weights applied to the $\Lambda_c^+ \to p\pi^+\pi^-$ samples are shown in Fig. 45. They are used to determine the invariant mass shape of $\Lambda_c^+ \to p\pi^+\pi^-$ background only and are applied after the dedicated selection (without trigger and without muon PID). The mass shapes of $\Lambda_c^+ \to p\pi^+\pi^-$ misidentified background for two models are shown in Fig. 46

6.5 Correction to uncertainty of efficiency due to MC redecay method

In order to speed up the simulation, the redecay method is used. Typically the 100 signal events share the same underlying event. These repeating events introduces the correlation which increases the probability of selecting the events if one event out of a set of one hundred has been accepted. Therefore, the effective number of independent events is reduced and the uncertainty is larger than calculated assuming no correlation.

To determine the correction factor, a ToyMC model is used based on selected signal events in the simulated samples. The total of 2964 events were selected out of 3 million events. This corresponds to efficiency of 0.9×10^{-3}. The distributions of the number of selected events in the redecay set of 100 events are shown in Fig. 47 for simulation and for the case without correlation. The tail in the distribution for simulation indicates that the events are not independent. To reproduce that distribution a simple model is defined. The separate probabilities to select a given number of events in one redecay set are introduced. The sets of 100 events are drawn starting with the probability of single event selection. If an event is drawn, the selection probability is set accordingly (to probability of selecting two events in the set of 100 events) and 99 subsequent events are drawn. If the second event is not drawn, the set is completed and the next set of 100 events is considered. If the second event is drawn, 98 events are drawn with modified probability. This is continued up to potentially 8 events to be drawn in one set.The corresponding eight probabilities are determined by the χ^2 fit to minimize the difference to simulated distribution. The results of the modelling are shown in Fig. 47 (red line).

The uncertainty of the efficiency for the model is determined by repeating 1000 pseudo experiments. The distribution of the efficiency is presented in Fig. 48. The sigma of that distribution is taken as the uncertainty of the efficiency. It corresponds to relative uncertainty of 2.86 %. For the case without the correlation, the uncertainty is 1.84 %. Hence the

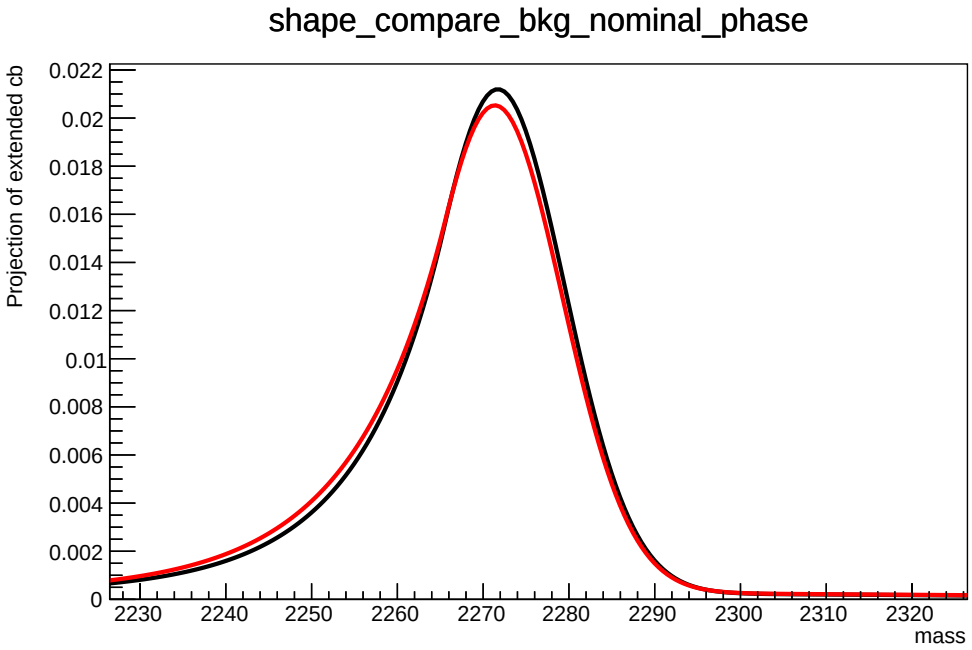

Figure 46: The mass shapes of $\Lambda_c^+ \to p\pi^+\pi^-$ misidentified background for two models: model measured in Ref. [92] (black line) and the phase space model (red line).

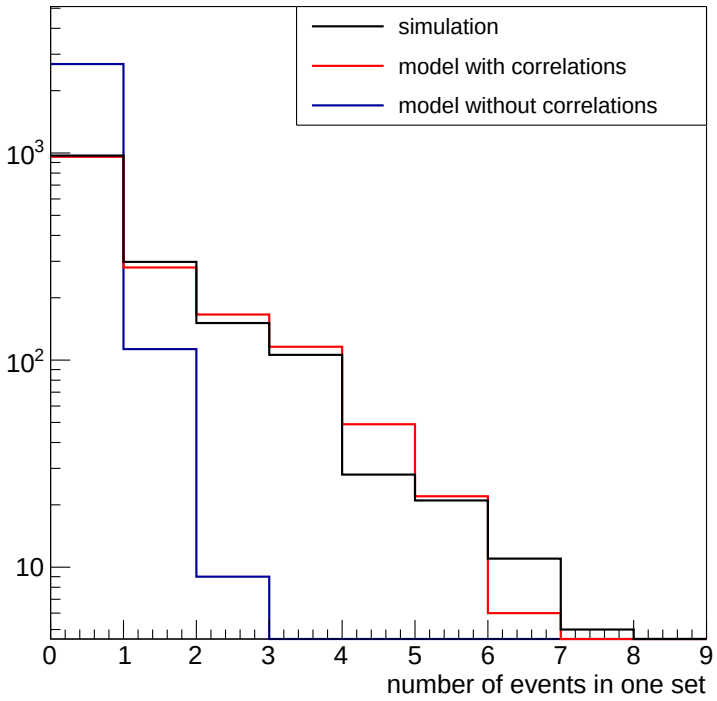

Figure 47: The distributions of the number of selected events in the redecay sets of 100 events for: simulation (black line), the distribution from the ToyMC model (red line) and the distribution without any correlation assumed (blue line). The first bin corresponds to the number of sets with single event selected, the second bin corresponds to two events selected and accordingly for the following bins.

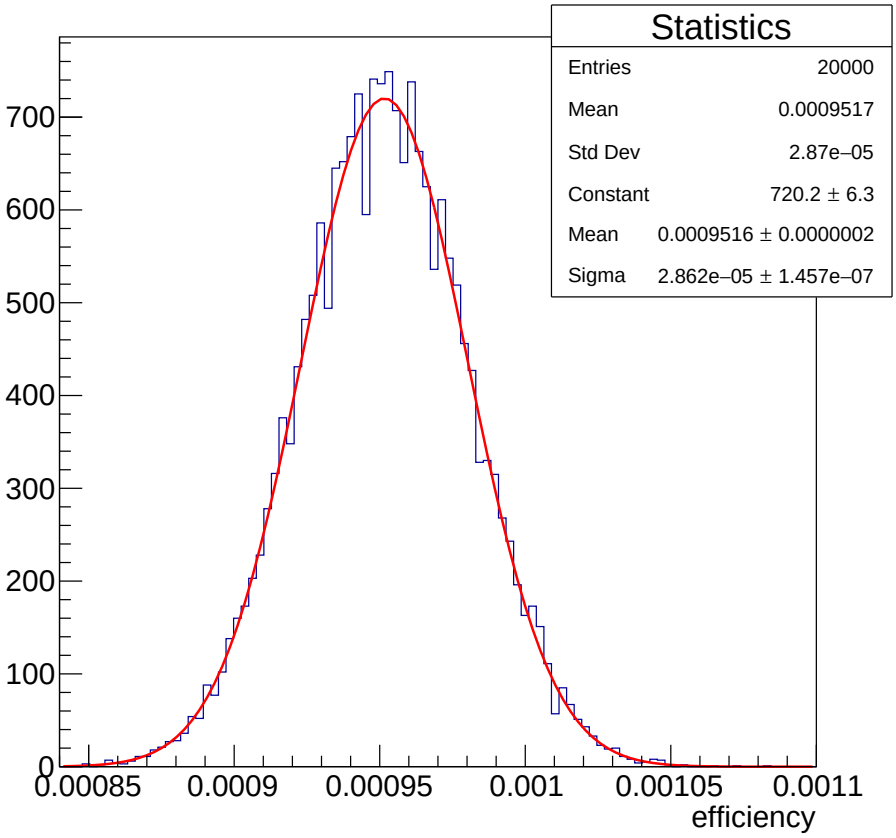

Figure 48: The distribution of efficiencies obtained from ToyMC model for 1000 pseudoexperiments.

uncertainty calculated for the case the without correlation has to be increased by a factor of 1.55. This factor is applied to all uncertainties determined from MC samples using the redecay model.

7 Background

7.1 Combinatorial background

The combinatorial background is well described by an exponential shape as can be seen in the plot showing the fit to signal sidebands in Fig. 59. The expected number of events for combinatorial background in the signal region $m_{\Lambda_c} \pm 21$ MeV/c^2 (approximately 3σ of the distribution) is 105.0 ± 4.6.

7.2 Resonant background

There are a few resonant decays possible, listed in Table 15, together with the decay BFs. As in addition to the normalization channel, one expects significant number of events for the three resonant decays via ρ, ω and η. The corresponding ranges of dimuon invarant mass are removed from the signal definition (Table 4). From this resonant regions one expects about 67 $\Lambda_c^+ \to p\omega(\mu^+\mu^-)$, 38 $\Lambda_c^+ \to p\rho(\mu^+\mu^-)$ and 7 $\Lambda_c^+ \to p\eta(\mu^+\mu^-)$ events. Only 2.8 events from resonant regions are expected to leak from the tail of $\Lambda_c^+ \to p\phi(\mu^+\mu^-)$ into *high* q^2

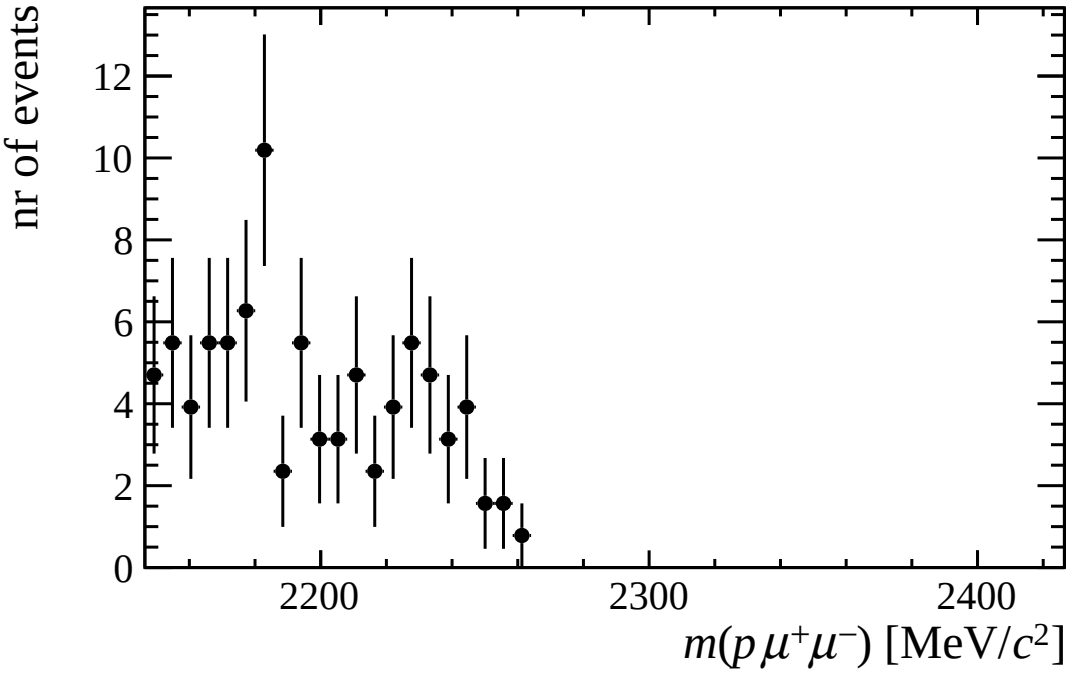

Figure 49: The distribution of $p(\mu^+\mu^-)$ invariant mass from selected $\Lambda_c^+ \to p\eta(\mu^+\mu^-\gamma)$ background decays.

region. In the case of *low* q^2 no events from the three resonant decays via ρ, ω and η are expected to contribute. The only resonant background which can affect *low* q^2 region is $\Lambda_c^+ \to p\eta(\mu^+\mu^-\gamma)$. This contribution is estimated using a simulation. The expected number of events is estimated to be 88 ± 31 events. The distribution of $p\mu^+\mu^-$ invariant mass is shown in Fig. 49. It can be seen that no contribution to the signal peak is expected.

Table 15: Summary of resonant decays of Λ_c^+. The BF($\Lambda_c^+ \to p\rho$) is not known and the corresponding BF($D^+ \to \pi^+\rho$) is quoted in red color.

Resonance X	BF($\Lambda_c^+ \to pX$)	BF($X \to \mu^+\mu^-$)	Total BF
η	$(1.24 \pm 0.30) \times 10^{-3}$	$(5.8 \pm 0.8) \times 10^{-6}$	$(7.19 \pm 2.00) \times 10^{-9}$
ρ	$(8.3 \pm 1.4) \times 10^{-4}$	$(4.55 \pm 0.28) \times 10^{-5}$	$(3.78 \pm 0.72) \times 10^{-8}$
ω	$(9 \pm 4) \times 10^{-4}$	$(7.4 \pm 1.8) \times 10^{-5}$	$(6.66 \pm 3.33) \times 10^{-8}$
ϕ	$(1.06 \pm 0.14) \times 10^{-3}$	$(2.86 \pm 0.19) \times 10^{-4}$	$(3.03 \pm 0.45) \times 10^{-7}$
Resonance	BF($\Lambda_c^+ \to pX$)	BF($X \to \mu^+\mu^-\gamma$)	Total BF
η	$(1.24 \pm 0.30) \times 10^{-3}$	$(3.1 \pm 0.4) \times 10^{-4}$	$(3.84 \pm 1.05) \times 10^{-7}$
η'	-	$(1.13 \pm 0.28) \times 10^{-4}$	-

7.3 Background due to misidentification

There are two possibilities for misidentified background: i) decays with a proton in the final state with a possible misidentification of other two decay products as muon ii) decay into $\mu^+\mu^-$ and a hadron misidentified as a proton. A few such reflections are shown in Fig. 50. It can be seen from the shape of invariant mass distributions that the only candidate for peaking background affecting the signal region is $\Lambda_c^+ \to p\pi^+\pi^-$. Other decays contribute as combinatorial background. Misidentified $\Lambda_c^+ \to p\pi^+\pi^-$ events show up as peaking background in signal region and can also affect the yield of normalization channel. This will be discussed in the following chapter.

7.4 Contribution of $\Lambda_c^+ \to p\pi^+\pi^-$ background to signal

The $\Lambda_c^+ \to p\pi^+\pi^-$ has a relatively large branching fraction and its reflection falls into the area of the signal peak. This mode is expected to be suppressed due to the double $\pi \to \mu$ misidentification ($IsMuon = 1$ required for signal muons followed by a further cut on $ProbNNmu(\mu)$). However, owing to a large branching fraction, one can expect a visible peak from $\Lambda_c^+ \to p\pi^+\pi^-$ with such double $\pi \to \mu$ misidentification.

The direct study by applying exactly the same selection chain as for the signal is not feasible, as it would require the production of very large samples. The contribution of this background will be included in the fit to the mass distribution with the yield of this background floating and its shape fixed form simulation. The shape can be determined using the available simulated samples of $\Lambda_c^+ \to p\pi^+\pi^-$ decays corrected for the decay model (Sec. 6.4) by employing the following procedure. The `Lc23MuLc2pmumuLine` stripping algorithm is modified by removing the muon identification requirement. Then the selection for $\Lambda_c^+ \to p(\mu^+\mu^-)$ is applied without the trigger and without imposing a cut on $ProbNNmu$. The resulting mass shape together with the fit to the two component model, the sum of CB function and Gaussian is shown in Fig. 52. The parameters of the model are listed in Table 16. This procedure of shape determination is verified on a signal sample. The $p(\mu^+\mu^-)$ mass shapes obtained for the standard selection and for the selections used to obtain the mass shape for $\Lambda_c^+ \to p\pi^+\pi^-$ are compared in Fig. 51. No significant difference is seen.

Table 16: The parameters of the $\Lambda_c^+ \to p\pi^+\pi^-$ backgound model, the sum of CB function and Gaussian, obtained from the fit to $\Lambda_c^+ \to p\pi^+\pi^-$ invariant mass distribution for simulated sample after dedicated selection described in the text. The correction for proper decay model from the Ref. [92] is applied to the simulation.

Parameter	Value
μ CB [MeV/c^2]	2269.63337 ± 0.06407
σ CB [MeV/c^2]	8.97445 ± 0.05549
α CB	0.94310 ± 0.01615
n CB	7.15411 ± 0.88444
μ Gauss [MeV/c^2]	2242.21477 ± 4.10993
σ Gauss [MeV/c^2]	73.77134 ± 3.56626
fraction CB/Gauss	0.95486 ± 0.00290

The expected yield of $\Lambda_c^+ \to p\pi^+\pi^-$ misidentified background in the data can be determined approximately under some assumptions. The important element is the misidentifica-

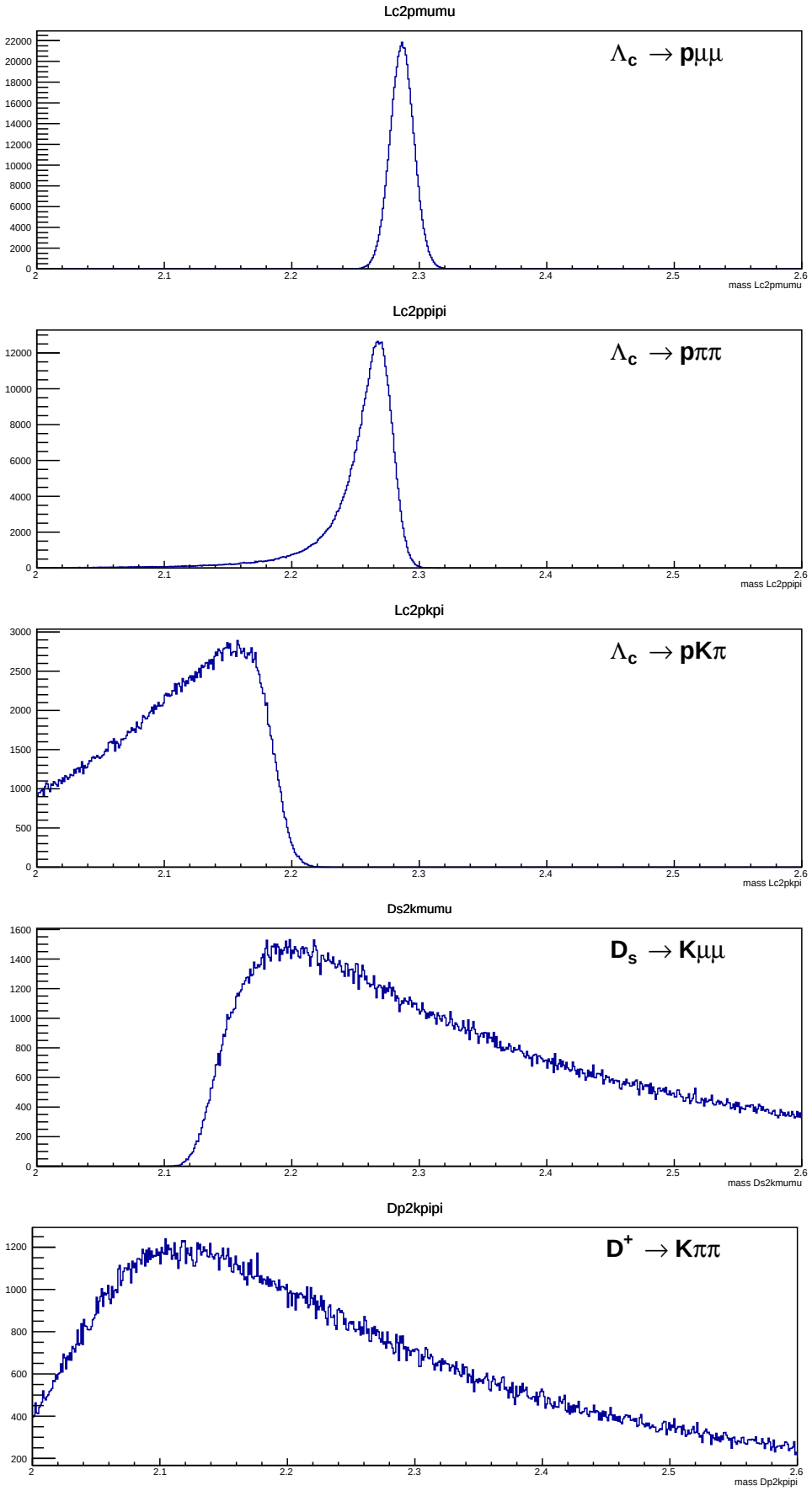

Figure 50: The possible reflections into $\Lambda_c^+ \rightarrow p(\mu^+\mu^-)$ determined by Toy MC decay model with appropriate momentum smearing. The invariant mass distributions are shown for $p\mu^+\mu^-$ hypothesis. The top plot shows the distribution for signal to indicate the location and width of signal peak.

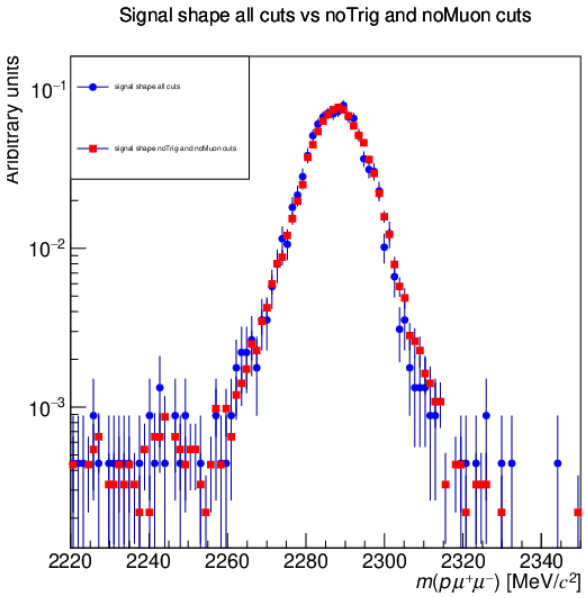

Figure 51: The comparison of $p\mu^+\mu^-$ mass shapes for the signal sample for standard selection (blue dots) and selection used to obtain mass shape for $\Lambda_c^+ \to p\pi^+\pi^-$ (red squares).

tion factor. It is determined by PIDCalib package using an unbiased sample of pions and imposing a requirement $IsMuon = 1$ and $ProbNNmu > 0.68$. The luminosity weighted $\pi \to \mu$ misidentification factor is measured to be $\epsilon_{\pi\to\mu} = 0.334\%$. A factorization for misid of two pions is assumed. The expected number of $\Lambda_c^+ \to p\pi^+\pi^-$ is determined with respect to the normalization channel using the ratios of efficiencies, branching ratio and the number of events for the normalization channel according to the following formula:

$$N_{\Lambda_c^+\to p\pi^+\pi^-} = N_{\Lambda_c^+\to p(\mu^+\mu^-)} \times \frac{B(\Lambda_c^+ \to p\pi^+\pi^-)}{B(\Lambda_c^+ \to p\phi(\mu^+\mu^-))} \times \frac{\epsilon^{SEL}_{\Lambda_c^+\to p\pi^+\pi^-}}{\epsilon^{SEL}_{\Lambda_c^+\to p\phi(\mu^+\mu^-)}} \times \frac{\epsilon^{TRIG/SEL}_{\Lambda_c^+\to p\pi^+\pi^-}}{\epsilon^{TRIG/SEL}_{\Lambda_c^+\to p\phi(\mu^+\mu^-)}} \times (\epsilon_{\pi\to\mu})^2$$

where ϵ^{SEL} indicates the total efficiency without trigger, $\epsilon^{TRIG/SEL}$ indicates the relative efficiency with respect to SEL and $(\epsilon_{\pi\to\mu})^2$ accounts for double $\pi \to \mu$ misidentification. The ratio of relative efficiencies TRIG/SEL is assumed to be equal to one, which is a kind of upper limit estimate as one expects lower trigger efficiency for misidentified channel. The expected number of $\Lambda_c^+ \to p\pi^+\pi^-$ events after selection is estimated to be 15.2 ± 2.6.

7.5 Contribution of $\Lambda_c^+ \to p\pi^+\pi^-$ background to $\Lambda_c^+ \to p\phi(\mu^+\mu^-)$

The $\Lambda_c^+ \to p\pi^+\pi^-$ background contributing to the normalization channel is estimated by the same method as for the signal described in Sec. 7.4. The expected number of misidentified $\Lambda_c^+ \to p\pi^+\pi^-$ events is estimated to be 6.4 ± 1.1. The contribution from $\Lambda_c^+ \to p\pi^+\pi^-$ to selected $\Lambda_c^+ \to p\phi(\mu^+\mu^-)$ in data is taken into account in the fit to mass distribution including a component for $\Lambda_c^+ \to p\pi^+\pi^-$ with fixed shape and free yield. The fit is described in Sec. 10.2. The fit gives a result compatible with the estimated number of $\Lambda_c^+ \to p\pi^+\pi^-$ misidentified events. Additional cross-checks are described in Sec. H.

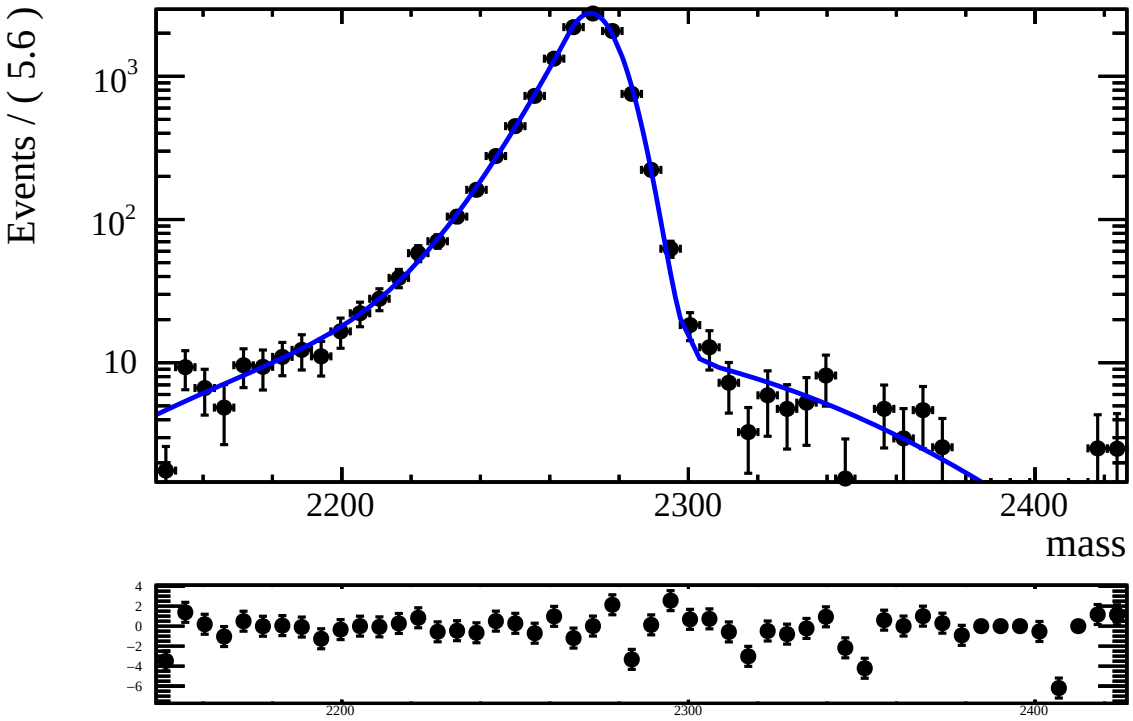

Figure 52: The $p\mu\mu$ invariant mass distribution for simulated $\Lambda_c^+ \to p\pi^+\pi^-$ events selected using the same requirements as for signal without any condition for muon PID and without applying the trigger. The solid line indicates the result of the modeling by the sum of the CB shape and Gaussian.

8 The fitter and CLs determination

The fitter is incorporated into the GammaCombo package 3.3.1 where the CLs method is implemented. The extended fit to the full range of $p(\mu^+\mu^-)$ invariant mass is used. Two PDFs are defined that corresponds to two hypotheses: one PDF containing the background plus a signal and the second containing only background. In the case of the signal plus background model, the signal is described by the CB function with fixed parameters from the simulation (Table 19). The background PDF is a sum of two components: the combinatorial background characterized by the exponential shape and $\Lambda_c^+ \to p\pi^+\pi^-$ peaking background described by the sum of CBe function and Gaussian with fixed parameters (Table 16). In the case of the background, there are three free parameters: total background yield, fraction of the two background components (combinatorial over $\Lambda_c^+ \to p\pi^+\pi^-$) and a parameter for exponential function describing the combinatorial component. In the case of the signal only the yield is allowed to float. Negative signal yields are allowed. The fitter is validated by means of ToyMC. In each pseudo-experiment the sample is generated using total PDF. The number of background events (sum of $\Lambda_c^+ \to p\pi^+\pi^-$ and combinatorial) is set according to the result from the fit. The parameter of exponential shape of combinatorial background is taken from the fit to data sidebands. The the generated mass distribution is than fitted with the PDF with floating parameters as in the fitter incorporated into GammaCombo described above. The example of fit results is shown in Fig. 53. To check for possible biases, the difference between generated and fitted value of signal events is checked. For each value of signal events one million of pseudo-experiments are performed and the difference between the average of fitted values and the generated value is calculated. The absolute difference of the number of signal events is shown in Fig. 54. One can see that the relative difference for 15

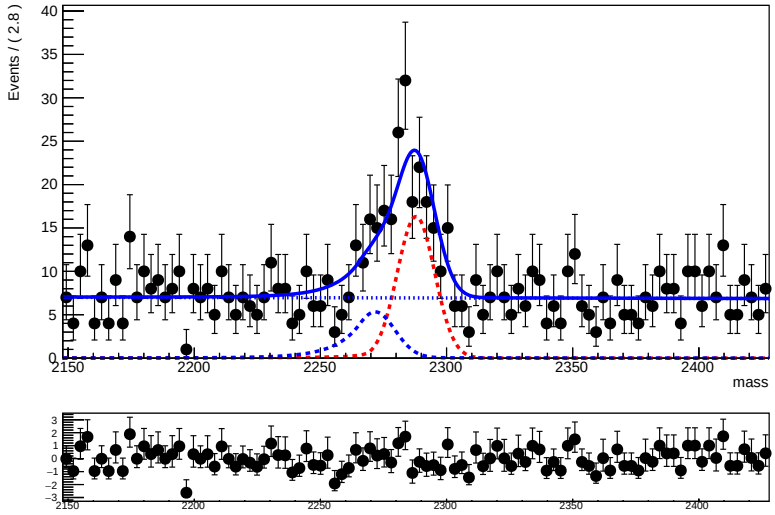

Figure 53: Example of the fit to the mass generated distribution. The mass distribution was generated for 700 events of combinatorial background, 50 $\Lambda_c^+ \to p\pi^+\pi^-$ misidentified background events and 100 signal events. The solid line corresponds to total PDF. The red and blue dashed lines correspond to signal and $\Lambda_c^+ \to p\pi^+\pi^-$ background respectively. The blue dotted line indicates the combinatorial background component.

signal events is about 0.3%. The pull distributions for free parameters in the fit are shown in Fig. 55.

9 Systematic uncertainties

The final state of signal and normalization channels is identical. Therefore most of systematic effects tend to cancel. In particular the systematics related to trigger, tracking efficiency and hadronic interactions are assumed to be small with respect to other sources and are neglected. The summary of systematic uncertainties is given in Table 17 and described in the following section.

Variation of ratio of efficiencies due to the size of MC samples.
The statistical uncertainty of the ratio of total efficiencies for the normalization channel and signal channel due to limited MC statistics has been included in the sources of systematics of the CLs method. The total efficiency is determined using MC samples of the signal and normalization channel corresponding to the mixture of prompt and secondary Λ_c^+ production. The efficiency is determined by counting candidates with a relevant background category (Sec. 6.1). The binomial errors are assigned to both efficiencies. The uncertainty of the ratio of total efficiencies is determined by adding the uncertainties of the two efficiencies in quadrature.

Variation of ratios of efficiencies due to Data/MC disagreement.
After applying the reweighting procedure the data agreed relatively well with the simulation within statistical uncertainties of the data points. Three other reweightings are checked with an additional third variable: log_Lc_IPCHI2_OWNPV, log_Lc_ENDVERTEX_CHI2, and log_Lc_FDCHI2_OWNPV. The average difference of a efficiency ratios with respect to nominal reweighting is taken as systematic uncertainty.

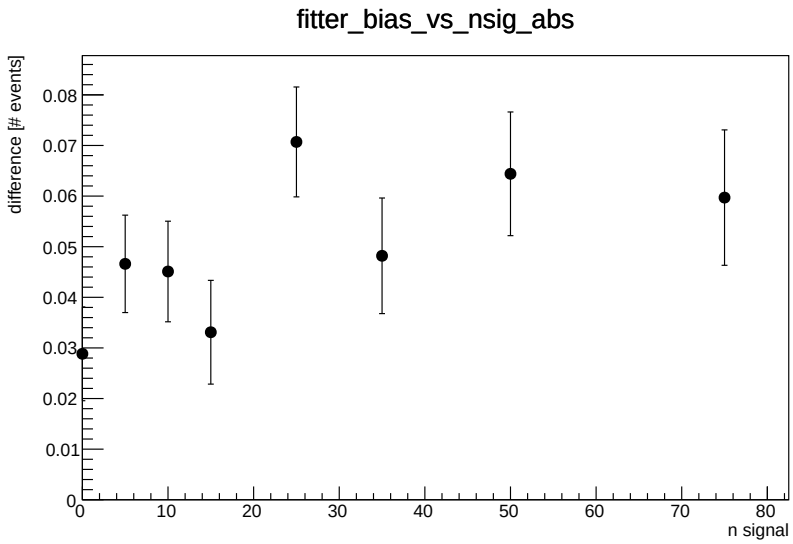

Figure 54: The dependence of the fitter bias on the number of signal events.

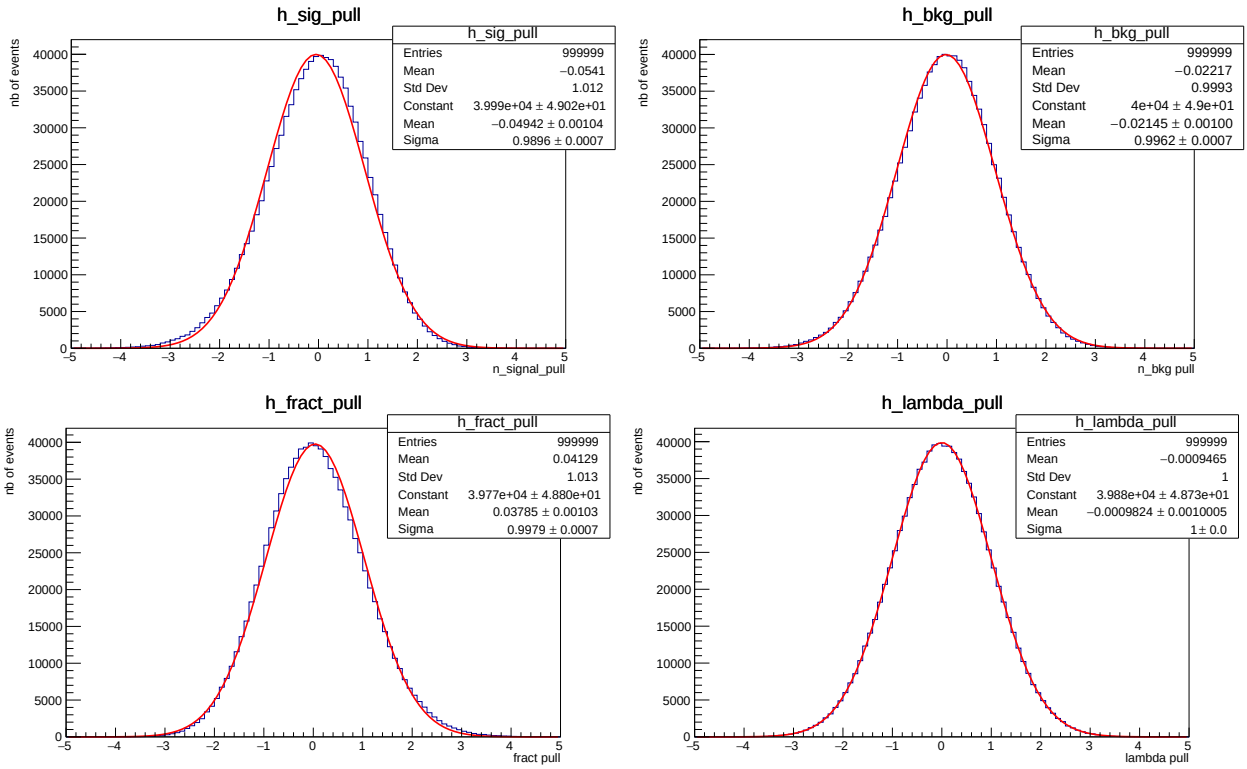

Figure 55: The pull distributions for the four free parameters in the fit obtained by ToyMC for 15 signal events, 15 $\Lambda_c^+ \to p\pi^+\pi^-$ and 700 combinatorial background events.

Table 17: The summary of systematic uncertainties.

Uncertainty source	Value [%]
Efficiency ratio (stat.)	6.41
Efficiency ratio (Data/MC disagreement)	1.64
Efficiency ratio (MC matching)	0.02
Efficiency ratio (PID resampling)	0.37
Yield of normalization channel (stat. from fit)	5.26
Yield of normalization channel ($\Lambda_c^+ \to p\pi^+\pi^-$ contribution)	1.50
Yield of normalization channel (fit variants)	0.02
Fit model for signal (CB vs Johnson)	1.05
Fit model for $\Lambda_c^+ \to p\pi^+\pi^-$ background (CB+Gaus vs Johnson+Gaus)	0.32
Mass shape of signal channel (MC parametrization)	1.88
Mass shape of $\Lambda_c^+ \to p\pi^+\pi^-$ background (MC parametrization)	0.90
Mass shape of $\Lambda_c^+ \to p\pi^+\pi^-$ background (decay model)	0.08
pure phase space vs model from Ref. [92]	
Mass shape of combinatorial background (exp vs linear)	0.09
$B(\Lambda_c^+ \to p(\mu^+\mu^-))$ uncertainty	14.78
Total (for BF upper limit)	17.26
Total without $B(\Lambda_c^+ \to p(\mu^+\mu^-))$ uncertainty (for BR)	8.92

Variation of ratios of efficiencies due to MC matching.
The change of the efficiency ratio after adding background category of 60 is included.

Variation of ratios of efficiencies due to PID resampling.
The change of the efficiency ratio between standard resampling and alternative resampling.

Yield of normalization channel (stat).
The statistical uncertainty on the number of selected events in the data for the normalization channel is assigned as a source of systematic uncertainty. The yield for the normalization channel is estimated by the fit described in Sec. 10.2.

Yield of normalization channel ($\Lambda_c^+ \to p\pi^+\pi^-$ contribution).
The yield is determined by the fit described in Sec. 10.2. The fit without $\Lambda_c^+ \to p\pi^+\pi^-$ component is checked and the difference is included in systematics.

Yield of normalization channel (fit variants).
The difference in the yield between the standard fit and the fit with all CB parameters floating is included in systematic uncertainty.

Fit model for signal (CB vs Johnson).
The difference between the nominal model (CB) and alternative model (Johnson) is included in systematic uncertainty.

Fit model for $\Lambda_c^+ \to p\pi^+\pi^-$ background (CB+Gaus vs Johnson+Gaus).
The difference between two background models for $\Lambda_c^+ \to p\pi^+\pi^-$ background, the nominal model (CB+Gaus) and the alternative model (Johnson+Gaus) is included in systematic uncertainty.

Mass shape of signal channel (MC parametrization).
The shape of the signal channel is determined from the simulation (Table 19). The systematic uncertainty related to the uncertainty of CB parameters is determined with Toy MC. In each pseudo-experiment the set of CB parameters was taking into account their correlations. The number of signal events form the fit to nominal set of CB parameters and from the fit to varied parameters is determined. The standard deviation of distribution of their differencies is taken as an uncertainty.

Mass shape of $\Lambda_c^+ \to p\pi^+\pi^-$ background (MC parametrization).
The same procedure as for the signal shape is applied to double CB parametrization of $\Lambda_c^+ \to p\pi^+\pi^-$ background.

Mass shape of $\Lambda_c^+ \to p\pi^+\pi^-$ background (decay model).
The uncertainty due to $\Lambda_c^+ \to p\pi^+\pi^-$ decay model is estimated by means of ToyMC. The difference in the mean value of signal yield for the two decay models, the phase space and the model from the Ref. [92] is taken as uncertainty. Implementation of this model is described in Sec. 6.4.

Mass shape of combinatorial background (exp vs linear).
The exponential shape is used to describe the shape of combinatorial background. The systematic uncertainty is estimated by comparing the result obtained by a linear fit. The ToyMC is used with the yields for the signal and background as described in Sec. 8.

The shape of the dimuon invariant mass for the signal.
The results presented in this note are derived assuming the phase space decay model for signal. The physics model of the signal decay is not known yet and the corresponding systematic uncertainty cannot be assigned in a reliable way. Therefore we do not assign any systematic uncertainty due to the Λ_c^+ decay model.

Fitter bias.
The expected upper limit for branching fraction at 90 % C.L. corresponds to 15 signal events. The fitter bias for a low number of signal events is determined to be at the level of 0.04 events. For 15 signal events, the relative bias is determined to be about 0.3%. In the case of the GammaCombo plugin method used in this analysis, the fitter bias is taken into account and corrected. Therefore no systematic uncertainty is assigned.

9.1 Efficiency weights for signal

The decay model for the signal is not known. The simulated samples for the signal are generated according to the phase space model. No systematic uncertainty is assigned due to the lack of knowledge of a signal decay model. Instead, a table of efficiency weights

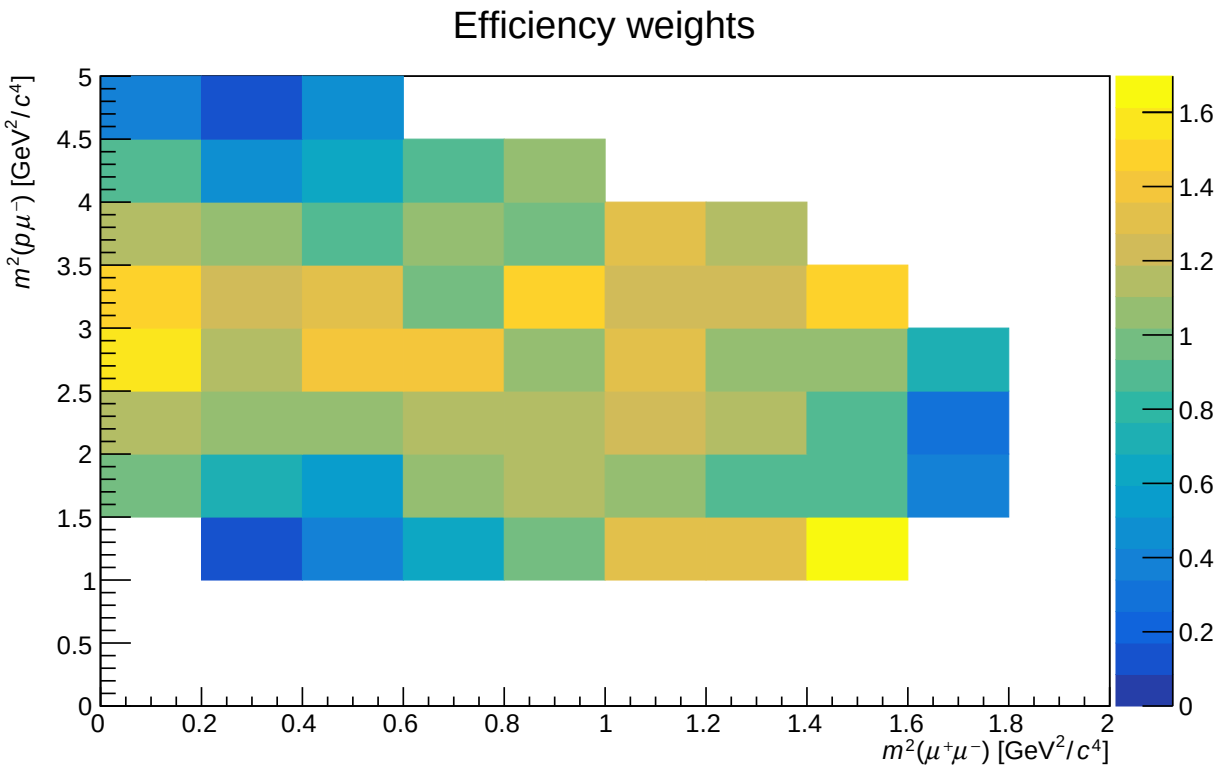

Figure 56: The graphical representation of efficiency weights as a function of: $m^2_{\mu^+\mu^-}$ and $m^2_{p\mu^-}$.

covering the phase space of decay products is provided. The weights are determined in bins of $m^2_{\mu^+\mu^-}$ and $m^2_{p\mu^-}$. They are normalized to average of unity, presented in Table 18 and shown graphically in Fig. 56. These weights are not applied in the analysis. They can be used to recalculate the relative change of signal yield for any other decay model and to rescale the results of the analysis.

Table 18: The values of efficiency weights in bins of $m^2(\mu^+\mu^-)$ and $m^2(p\mu^-)$ expressed in units of $(\,\mathrm{GeV}/c^2)^2$. The weights are normalized to average of unity.

$m(\mu^+\mu^-)\ \backslash m(p\mu^-)$	$[1, 1.5]$	$[1.5, 2]$	$[2, 2.5]$	$[2.5, 3]$	$[3, 3.5]$	$[3.5, 4]$	$[4, 4.5]$	$[4.5, 5]$
$[0.00, 0.20]$	0	1.07 ± 0.18	1.10 ± 0.15	1.37 ± 0.16	1.26 ± 0.15	1.00 ± 0.15	1.02 ± 0.18	0.56 ± 0.33
$[0.20, 0.40]$	0.28 ± 0.11	0.78 ± 0.12	1.03 ± 0.13	1.11 ± 0.13	1.24 ± 0.14	1.16 ± 0.14	0.61 ± 0.12	0.20 ± 0.14
$[0.40, 0.60]$	0.45 ± 0.11	0.55 ± 0.10	1.06 ± 0.13	1.30 ± 0.14	1.31 ± 0.14	0.87 ± 0.12	0.90 ± 0.15	0.80 ± 0.58
$[0.60, 0.80]$	0.66 ± 0.13	1.12 ± 0.14	1.07 ± 0.13	1.27 ± 0.14	0.91 ± 0.12	1.21 ± 0.14	1.12 ± 0.20	0
$[0.80, 1.00]$	0.99 ± 0.17	1.11 ± 0.13	1.00 ± 0.12	1.02 ± 0.13	1.42 ± 0.15	1.12 ± 0.14	1.10 ± 0.39	0
$[1.00, 1.20]$	1.22 ± 0.20	0.98 ± 0.12	1.15 ± 0.13	1.27 ± 0.14	1.21 ± 0.14	1.33 ± 0.20	0	0
$[1.20, 1.40]$	1.23 ± 0.25	0.82 ± 0.11	1.08 ± 0.13	0.99 ± 0.12	1.26 ± 0.15	1.12 ± 0.57	0	0
$[1.40, 1.60]$	1.83 ± 0.77	0.82 ± 0.11	0.82 ± 0.11	1.02 ± 0.13	1.42 ± 0.28	0	0	0
$[1.60, 1.80]$	0	0.34 ± 0.10	0.24 ± 0.06	0.68 ± 0.16	0	0	0	0

10 Analysis results

10.1 Invariant mass shapes for signal and normalization channel

The mass shapes for the signal and normalization channels are fitted using simulated samples after the full selection chain as in the case of data samples. The results of the fit to the CB shape are presented in Fig. 57 and listed in Table 19. It can be noted that the left tail of the CB shape is a bit shorter for the normalization channel. This is a result of the mass window cut for the dimuon invariant mass around the ϕ mass which reduces the final state radiation effect (see Fig. 39 right).

Table 19: The results of the fit to invariant mass distribution for the simulated signal and normalization channels. The CB parametrization is used for both channels.

Parameter	$\Lambda_c^+ \to p(\mu^+\mu^-)$	$\Lambda_c^+ \to p\phi(\mu^+\mu^-)$
μ [MeV/c^2]	2287.90191 ± 0.22328	2287.97425 ± 0.13788
σ [MeV/c^2]	7.39911 ± 0.16406	7.36610 ± 0.10132
α	2.45590 ± 0.15672	2.24082 ± 0.10285
n	0.98989 ± 0.25454	2.15870 ± 0.37390

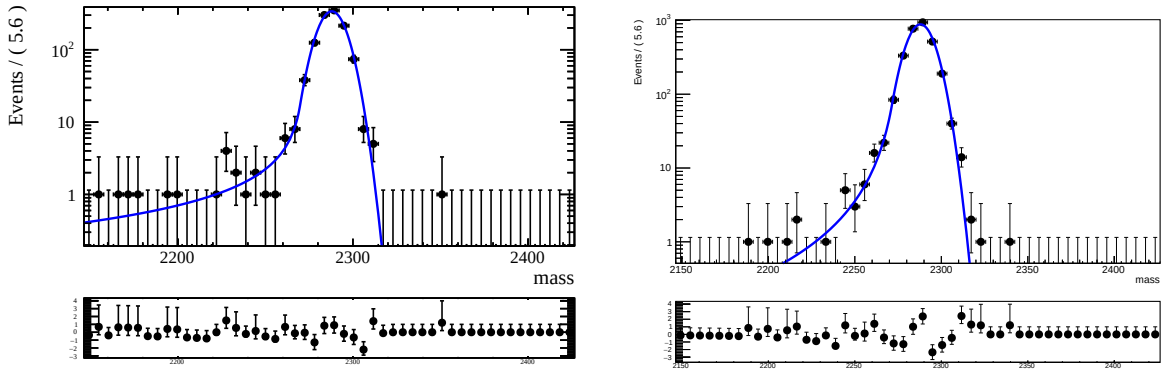

Figure 57: The fits to invariant mass distributions for MC $\Lambda_c^+ \to p(\mu^+\mu^-)$ (left) and MC $\Lambda_c^+ \to p\phi(\mu^+\mu^-)$ (right). The solid line shows the result of the fit to CB shape.

10.2 Yield of normalization channel

The yield of the normalization channel is determined by the three component fit. The full PDF is the sum of shapes for the normalization channel, the exponential background and mass shape of $\Lambda_c^+ \to p\pi^+\pi^-$ background. Only the shape of the exponential background component is allowed to float. The other two shapes are fixed from the simulation. The result of the fit is presented in Fig. 58. The yield of the normalization channel is found to be 417.8 ± 22.0 events. The contribution from $\Lambda_c^+ \to p\pi^+\pi^-$ is determined to be 11.5 ± 10.2 events, the value compatible within a relatively large uncertainty with the estimation described in Sec. 7.5. The yields for individual years are given in Table 33 in Sec. G.2. They are compatible taking into account the efficiencies and integrated luminosities.

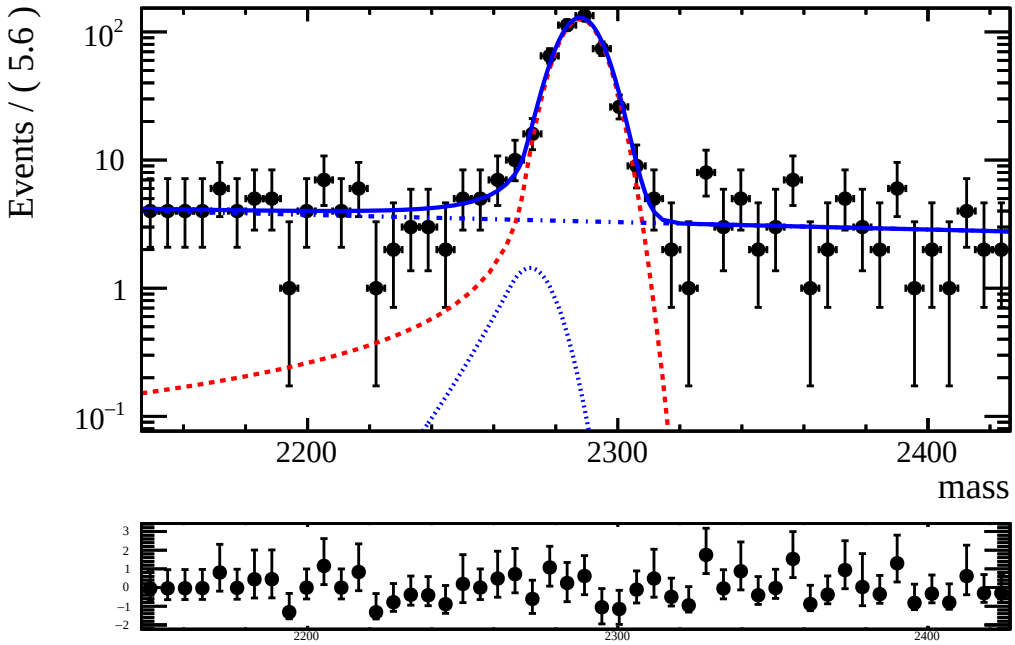

Figure 58: The results of the fit to $\Lambda_c^+ \to p\phi(\mu^+\mu^-)$ mass distribution selected in data. The mass shape consists of three components as described in the text. The solid line represents the sum of the three components, the red dashed line represents $\Lambda_c^+ \to p\phi(\mu^+\mu^-)$, the blue dash-dotted line represents exponential background, the blue dotted line represents the $\Lambda_c^+ \to p\pi^+\pi^-$ component.

10.3 Observed upper limits

In this section the results are quoted for the full signal region (the sum of the *low* q^2 and *high* q^2 regions) extrapolated to the entire dimuon mass range. The upper limit for the signal without the extrapolation as well as the results for *low* q^2 and *high* q^2 regions are given in Sec 10.4.

The fit to Λ_c mass distributions for various q^2 ranges is the same as described in Sec. 10.2 for the determination of the normalization channel yield. The shape of the $\Lambda_c^+ \to p\pi^+\pi^-$ background is determined individually for each q^2 range. The invariant mass distribution and the result of the fit for optimal cuts for the data is shown in Fig. 59. A total of 18.9 ± 9.7 signal events have been determined. In the full $p\mu^+\mu^-$ mass range considered, 683.3 ± 27.5 events of combinatorial background have been observed. The $\Lambda_c^+ \to p\pi^+\pi^-$ background component is determined to be consistent with zero, i.e. 0.0 ± 4.4 events. The significance of the signal determined by the Wilk's theorem taking into account statistical uncertainty only is 2.1σ. As significance is below a 3σ threshold needed for claiming the evidence, only an upper limit is determined. The UL for $B(\Lambda_c^+ \to p(\mu^+\mu^-))$ signal is calculated for the sum of 2016, 2017 and 2018 data samples using CLs method as described in Sec. 8. The upper limit of BR is found to be:

$$\frac{B(\Lambda_c^+ \to p(\mu^+\mu^-))}{B(\Lambda_c^+ \to p\phi(\mu^+\mu^-))} < 0.224 \quad \text{at} \quad 90\% \text{ CL}$$

$$\frac{B(\Lambda_c^+ \to p(\mu^+\mu^-))}{B(\Lambda_c^+ \to p\phi(\mu^+\mu^-)} < 0.250 \quad \text{at} \quad 95\% \text{ CL}$$

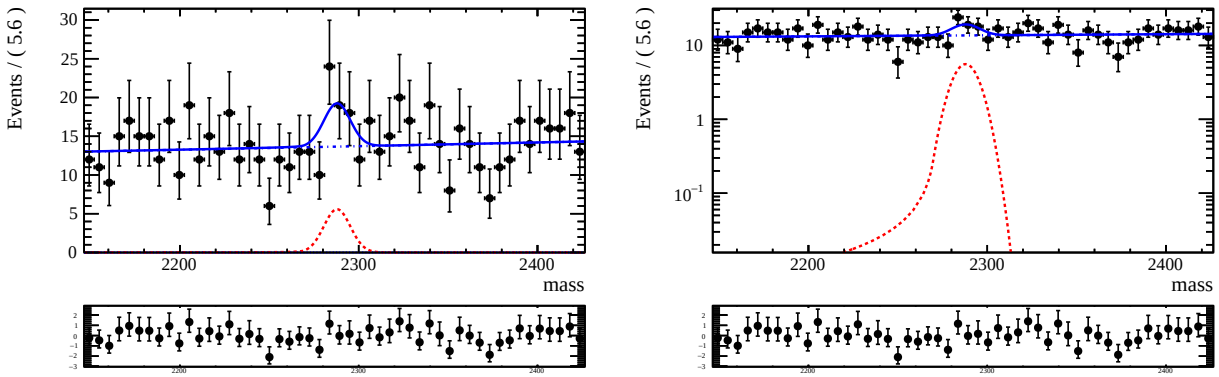

Figure 59: The invariant mass distribution after selection for optimized cuts for the data for linear (left) and logarithmic (right) scale. The fit components are described in Sec. 10.2.

The corresponding results on BF are:

$$B(\Lambda_c^+ \to p(\mu^+\mu^-)) < 7.3 \times 10^{-8} \quad \text{at} \quad 90\% \text{ CL}$$
$$B(\Lambda_c^+ \to p(\mu^+\mu^-)) < 8.1 \times 10^{-8} \quad \text{at} \quad 95\% \text{ CL}$$

The CLs dependence on BR and BF is shown in Fig. 60. The results are taken from the full range of dimuon mass. The efficiency is determined using a simulation of decays with a pure phase space model. All systematic uncertainties are taken into account when calculating the upper limit on the branching ratio. For the determination of the branching fraction, the uncertainty of $B(\Lambda_c^+ \to p\phi(\mu^+\mu^-)$ is excluded. The observed upper limits are higher than expected, assuming a null signal. One can notice that the observed upper limits are comparable to the ones determined for Run1 [38], while the expected upper limits are more than two times better for Run2. The reason for this is an excess of events in the *high* q^2 region. The contributions from the *low* q^2 and *high* q^2 regions are presented in the next section.

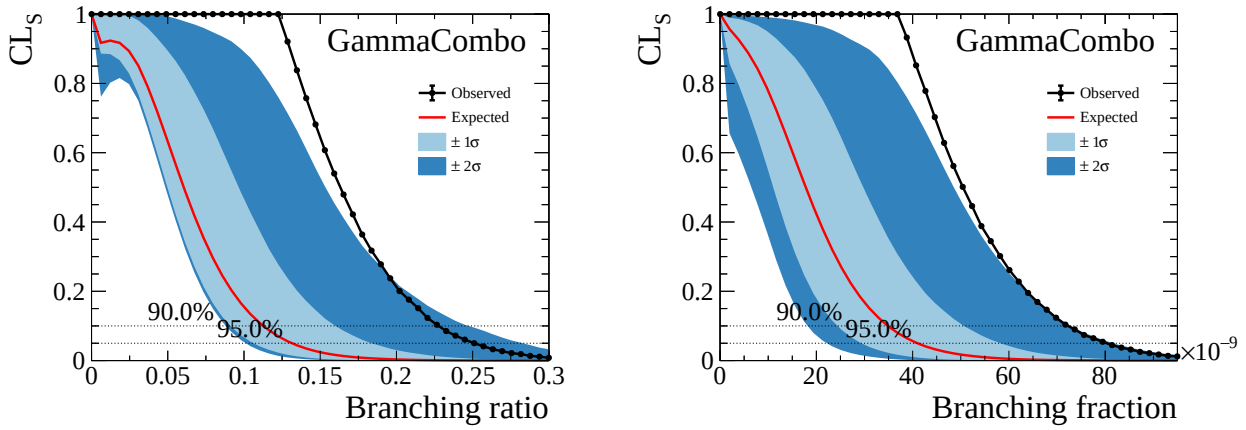

Figure 60: The CLs dependence on branching ratio with respect to normalization channel (left) and on branching fraction of signal channel (right).

Table 20: The total selection efficiency for the three ranges in the signal region and corresponding ratios of normalization channel efficiency to signal channel efficiency. The uncertainties of efficiency are statistical only.

Region	Signal efficiency in region [%]	Fraction of all generated events	Efficiency ratio normalization/signal
signal	$1.402 \times 10^{-2} \pm 7.494 \times 10^{-4}$	0.39633	1.024 ± 0.0655
low q^2	$1.466 \times 10^{-2} \pm 1.255 \times 10^{-3}$	0.14289	0.9794 ± 0.0906
high q^2	$1.366 \times 10^{-2} \pm 9.144 \times 10^{-4}$	0.25344	1.051 ± 0.0795

10.4 Observed upper limits in signal regions

The upper limits are determined in three signal regions as defined in Table 4: *signal*, *low* q^2 and *high* q^2. The results in this section are given without extrapolation to the full dimuon mass range. The corresponding efficiencies and fractions of generated events are specified in Table 20. The efficiency is defined as a ratio of the number of selected events in a given range divided by the number of generated events in this range. The efficiencies include Gauss factor listed in Table 2. The fraction with respect to all generated events corresponds to the pure phase space distribution, i.e. it is a fraction of generated events in a given range with respect to events generated in a full phase space. Therefore, to get efficiency with respect to the number of all generated events in the full phase space, one has to multiply the efficiency in column two by the fraction in column three of Table 20. The total efficiency for normalization channel is determined to be $(1.436245 \times 10^{-2} \pm 5.055394 \times 10^{-4})$ %, where the uncertainty is statistical only.

The *high* q^2 range is almost free from resonant decays neglecting the right tail of the ϕ Breit-Wigner distribution leaking from the $|m_{\mu^+\mu^-} - m_\phi| < 40$ MeV/c^2 window. In the case of *low* q^2 a possible contribution can come from the $\Lambda_c^+ \to p\eta(\mu^+\mu^-\gamma)$ decay as discussed in Sec. 7. The distributions of $p\mu^+\mu^-$ invariant mass for the *low* q^2 and *high* q^2 ranges are shown in Fig. 61. The results of the fit are presented in Table. 21.

Table 21: The results of the fit for the three signal regions.

Region	Signal events	$\Lambda_c^+ \to p\pi^+\pi^-$	Comb.	Significance
signal	18.9 ± 9.7	0.0 ± 4.4	683.3 ± 27.5	2.11σ
lowq	2.1 ± 5.0	0.0 ± 25.3	243.9 ± 16.3	0.45σ
highq	21.9 ± 8.4	0.0 ± 6.0	433.9 ± 22.0	2.96σ

As the significance for all signal regions is below 3σ, the upper limits are determined. The CLs dependence on the branching ratio and branching fraction for the three ranges of $m(\mu^+\mu^-)$ is shown in Fig. 62. The values of ULs are listed in Table 22. One can see that the dominant contribution to the total significance comes from the *high* q^2 region with the significance approaching 3σ. The effect close to 3σ needs to be further investigated. With the available statistics, an interpretation of this result other than the occurrence of statistical fluctuation is not justified.

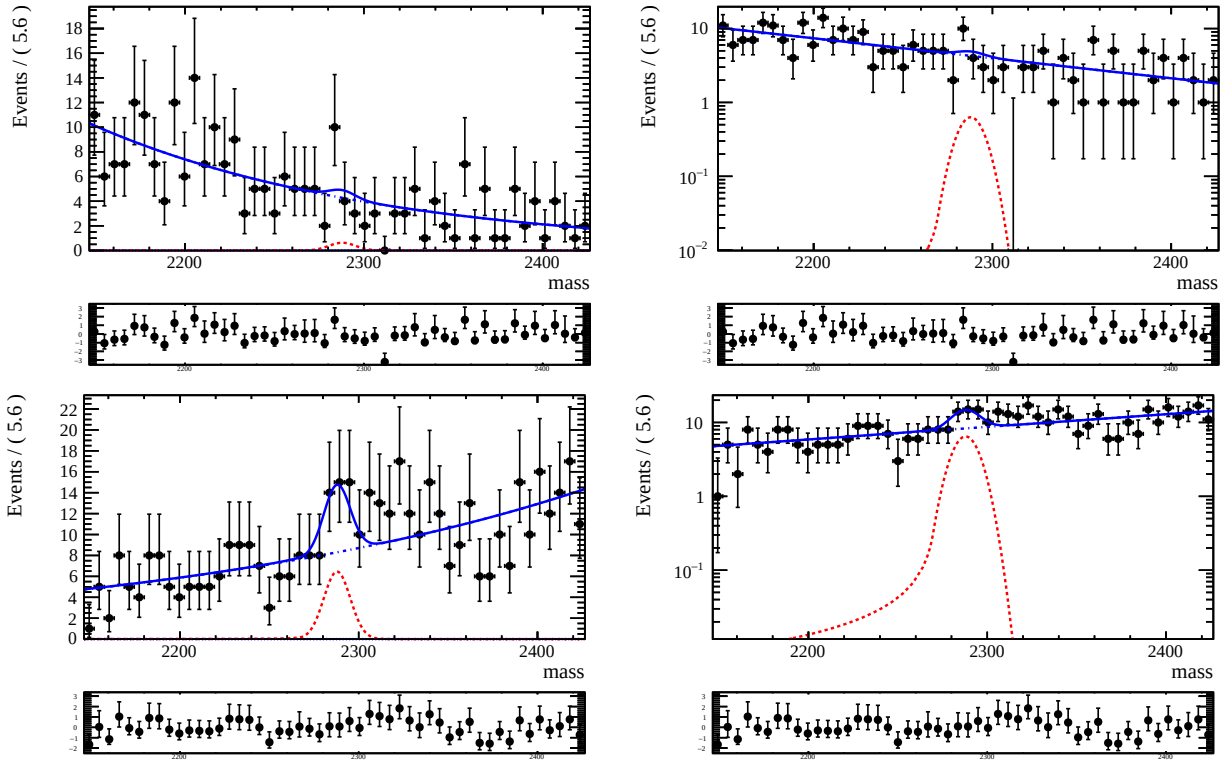

Figure 61: The $p\mu^+\mu^-$ invariant mass distributions after selection for optimized cuts for data for two subranges *low* q^2 (top) and *high* q^2 (bottom). The plots shown are in linear (left) and logarithmic (right) scale. The fit components are described in Sec. 10.2.

Table 22: The values of UL for the three ranges of $m(\mu^+\mu^-)$.

	signal	*low* q^2	*high* q^2
BR at 90% CL	0.090	0.0305	0.094
BR at 95% CL	0.099	0.0354	0.103
BF at 90% CL	2.9×10^{-8}	0.97×10^{-8}	3.0×10^{-8}
BF at 95% CL	3.2×10^{-8}	1.13×10^{-8}	3.3×10^{-8}

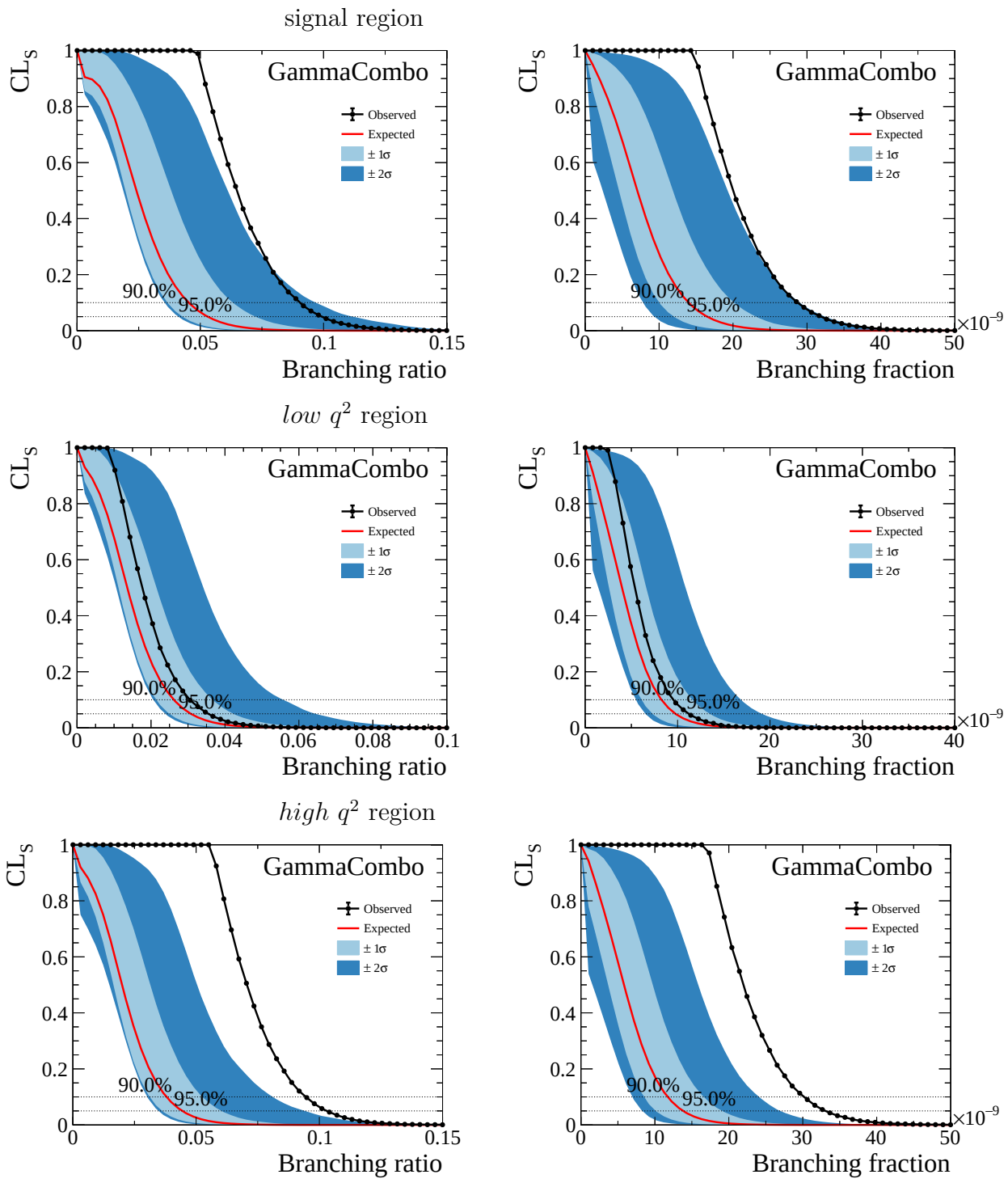

Figure 62: The CLs dependence on branching ratio with respect to normalization channel (left) and on branching fraction (right). Top plots correspond to signal range, middle plots to *low* q^2 range and bottom plots to *high* q^2 range.

10.5 Results for resonant regions

The resonant decays $\Lambda_c^+ \to p\omega(\mu^+\mu^-)$, $\Lambda_c^+ \to p\rho(\mu^+\mu^-)$ and $\Lambda_c^+ \to p\eta(\mu^+\mu^-)$ are selected using the same selection criteria as for the signal with additional change that replaces the veto condition with an appropriate requirement on dimuon mass to fall into the window around the resonance mass (Table 5). The shape of each resonant decay is determined from the simulation by the fit to CB function. The parameters of the CB function are listed in Table 23.

The distribution of $p\mu^+\mu^-$ invariant mass for resonant decays candidates selected from the data in the dimuon mass window around the ω, ρ and η mass is shown in Fig. 63.

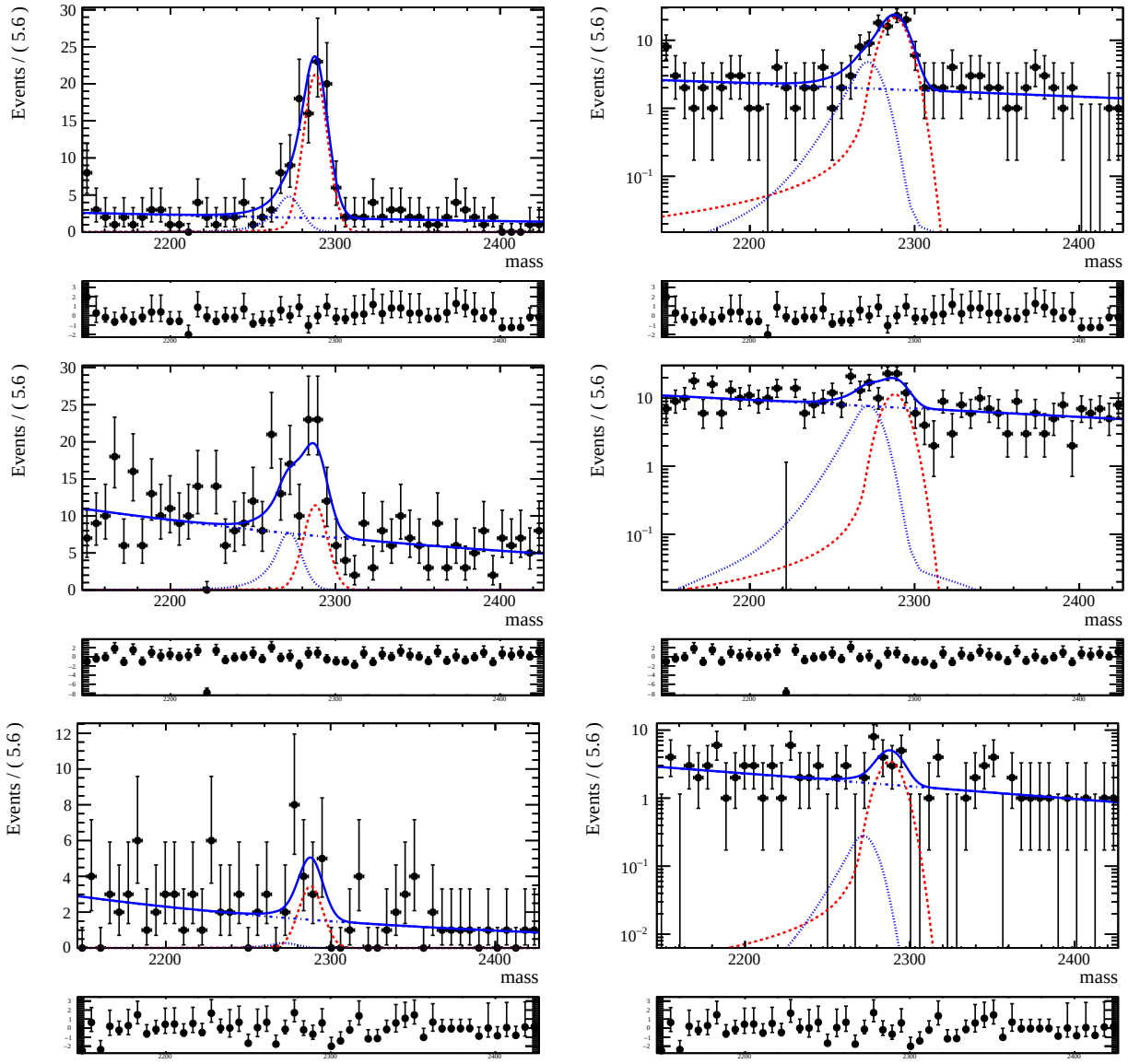

Figure 63: The $p\mu^+\mu^-$ invariant mass distribution of $\Lambda_c^+ \to p\omega(\mu^+\mu^-)$(top), $\Lambda_c^+ \to p\rho(\mu^+\mu^-)$ (middle) and $\Lambda_c^+ \to p\eta(\mu^+\mu^-)$ (bottom). The plots shown are in linear (left) and logarithmic (right) scale.

The results of the three component fit is also shown. The shape of mass distribution for resonant decays is fixed according to the simulation (Table 23). The background consists of two components: the combinatorial background described by the exponential function and

Table 23: The CB parameters of $p\mu^+\mu^-$ invariant mass from the fit to different resonant regions for simulated sample after selection.

Parameter	ω/ρ	ρ	η
mean [MeV/c^2]	2288.29 ± 0.16	2287.85 ± 0.20	2288.97 ± 0.55
σ [MeV/c^2]	8.11 ± 0.12	7.56 ± 0.15	6.55 ± 0.41
α	2.17 ± 0.11	2.20 ± 0.12	1.80 ± 0.29
n	2.18 ± 0.40	1.22 ± 0.22	2.14 ± 0.98

the $\Lambda_c^+ \to p\pi^+\pi^-$ background with the shape determined from the simulation and fixed. The yields of three components and the parameter of exponential background are floating in the fit. The results of the fit are presented in Table. 24. To calculate the significance of the

Table 24: The results for the three resonant regions.

Region	Signal events	$\Lambda_c^+ \to p\pi^+\pi^-$	Comb.	Significance
ω/ρ	72.0 ± 10.1	19.9 ± 7.6	96.1 ± 11.1	11.56σ
ρ	38.7 ± 9.5	32.2 ± 11.0	377.0 ± 21.8	5.17σ
η	11.7 ± 5.2	1.2 ± 5.4	84.2 ± 10.1	3.05σ

peaks, the Wilk's theorem is employed using statistical uncertainty only. In the case of ρ the significance treshold for observation is reached, which is the first observation of this decay.

The ratio of the branching fractions is determined similarly to the signal using formula 12 and replacing signal parameters with their resonant equivalent. The systematic uncertainties taken into account for the branching ratio determination are taken from Table 17 apart from uncertainities related to the ratios of efficiencies which are listed in Table 25. Branching ratios

Table 25: The ratios of efficiencies with respect to normalization channel.

Region	Efficiency ratio
ω/ρ	0.7862 ± 0.0194
ρ	0.4366 ± 0.0094
η	0.7785 ± 0.0424

with respect to normalization channel are determined for ω/ρ and ρ regions:

$$\frac{B(\Lambda_c^+ \to p\omega(\mu^+\mu^-))}{B(\Lambda_c^+ \to p\phi(\mu^+\mu^-))} = 0.222 \pm 0.031(stat.) \pm 0.015(syst)$$
$$\frac{B(\Lambda_c^+ \to p\rho(\mu^+\mu^-))}{B(\Lambda_c^+ \to p\phi(\mu^+\mu^-))} = 0.203 \pm 0.052\ (stat) \pm 0.013\ (syst)$$

The corresponding branching fractions are determined to be:

$$B(\Lambda_c^+ \to p\omega) = (9.08 \pm 1.26\ (stat) \pm 2.73\ (syst1) \pm 2.59\ (syst2))\ \times 10^{-4}$$
$$B(\Lambda_c^+ \to p\rho) = (1.35 \pm 0.34\ (stat) \pm 0.44\ (syst1) \pm 0.22\ (syst2))\ \times 10^{-3}$$

where the first systematic uncertainty (syst1) corresponds to systematic uncertainities of their branching ratios and the second systematic uncertainty (syst2) corresponds to uncertainties of $B(\Lambda_c \to p\phi)$, $B(\phi \to \mu^+\mu^-)$ and resonant decays, $B(\omega \to \mu^+\mu^-)$, $B(\rho \to \mu^+\mu^-)$ (Table 15).

10.6 Fit to dimuon mass spectrum

The exact disentanglement of the resonant contributions is not possible because of the interference effects. However, an approximate insight assuming no interference can be done. The dimuon mass spectrum for the $p\mu^+\mu^-$ mass window around Λ_c^+, $|m(p\mu^+\mu^-) - m_{\Lambda_c^+}| < 25$ MeV/c^2 is presented in Fig. 64. The result of the fit is also shown. The combinatorial background is described by the exponential function with a free parameter in the fit. The four peaks corresponding to η, ρ, ω and ϕ are parametrized by the voigtian function i.e. a convolution of Breit-Wigner shape and a Gaussian shape. The yields of the four components

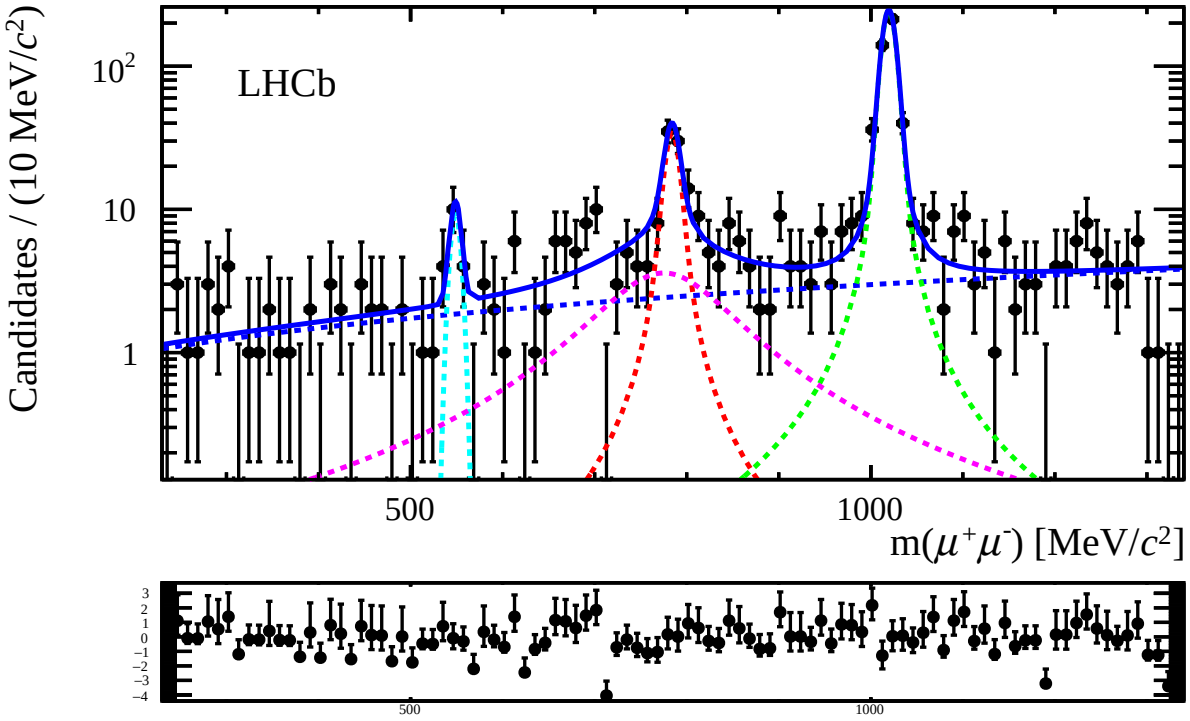

Figure 64: The result of the fit to dimuon invariant mass in the Λ_c^+ window, $|m(p\mu^+\mu^-) - m_{\Lambda_c^+}| < 25$ MeV/c^2. The four resonant decays are marked with different colors: ϕ - light green, ω - red, ρ - magenta, η - light blue.

are listed in Table 26. The data suggests that the branching fractions of $\Lambda_c^+ \to p\omega(\mu^+\mu^-)$ and $\Lambda_c^+ \to p\rho(\mu^+\mu^-)$ are comparable. The dominat contribution comes from the $\Lambda_c^+ \to p\phi(\mu^+\mu^-)$ decay, while the $\Lambda_c^+ \to p\eta(\mu^+\mu^-)$ mode has the smallest branching fraction.

Table 26: The yields from the fit to dimuon mass spectrum.

Decay	Yield
$\Lambda_c^+ \to p\phi(\mu^+\mu^-)$	445.9 ± 22.1
$\Lambda_c^+ \to p\omega(\mu^+\mu^-)$	71.8 ± 11.2
$\Lambda_c^+ \to p\rho(\mu^+\mu^-)$	69.5 ± 20.9
$\Lambda_c^+ \to p\eta(\mu^+\mu^-)$	11.3 ± 4.0

11 Summary and outlook

A search for the rare $\Lambda_c^+ \to p(\mu^+\mu^-)$ decay was presented. This FCNC decay is expected to be heavily suppressed in the Standard Model by the Glashow-Iliopoulos-Maiani mechanism. The branching fractions for short-distance contributions to the $c \to u\mu^+\mu^-$ transition are expected to be of $O(10^{-9})$ in the Standard Model, but can be enhanced by New Physics effects. Long-distance contributions proceeding via a tree-level amplitude, with an intermediate meson resonance decaying into a dimuon pair, can increase the branching fraction up to $O(10^{-6})$. Rare charm processes are complementary to the ones in strange and beauty sectors as they arise from FCNCs with different quantum loops. They provide a unique area for the New Physics searches as the influence of hypothetical massive particles can cause significant deviations from the SM prediction.

This study was based on a dataset recorded by the LHCb experiment during 2016-2018, corresponding to an integrated luminosity of 5.4 fb^{-1}. To separate the short- and long-distance processes, the whole dimuon mass range was divided into signal and resonant regions. The signal region covered low and high parts, $211.32 < m_{\mu^+\mu^-} < 507.86$ MeV/c^2 and $1059.45 < m_{\mu^+\mu^-} < 1348.13$ MeV/c^2 respectively. The resonant region, $507.86 < m_{\mu^+\mu^-} < 1059.46$ MeV/c^2, was analysed in four parts corresponding to ϕ, ρ, ω and η resonances. The branching ratios or their upper limits were determined with respect to the normalization channel $\Lambda_c^+ \to p\phi(\mu^+\mu^-)$. Choosing the same final state for the signal and normalization channels resulted in cancellation of systematic effects in the ratios.

A multivariate analysis was used to select signal events. The BDT method was trained on the simulated signal and background from data sidebands. The final selection was optimized in three variables: the BDT discriminant and particle identification probabilities for the proton and muon. No significant signal was observed above the background events in the signal region. The upper limit for branching ratio was set for the total signal region:

$$\frac{B(\Lambda_c^+ \to p\mu^+\mu^-)}{B(\Lambda_c^+ \to p\phi(\mu^+\mu^-))} < 0.224 \quad \text{at} \ \ 90\% \ \text{CL}$$
$$\frac{B(\Lambda_c^+ \to p\mu^+\mu^-)}{B(\Lambda_c^+ \to p\phi(\mu^+\mu^-)} < 0.250 \quad \text{at} \ \ 95\% \ \text{CL}$$

Compared to the Run1 result, the observed upper limit was lower by 15% only, while the expected upper limit was almost twice smaller. The effect can be linked to the high dimuon mass range, where the significance of the signal determined by the Wilk's theorem (statistical uncertainty only) approached 3σ. The interpretation of this effect which was close to the threshold of the evidence criterion is difficult with the available statistics. It could be a sign of the SM contribution or just a fluctuation, or both.

The results for resonant regions confirmed the observation of $\Lambda_c^+ \to p\omega(\mu^+\mu^-)$ reported by LHCb for Run1 with the branching ratio relative to the normalization channel: $0.231 \pm 0.078\,(stat) \pm 0.026\,(syst)$. The compatible branching ratio for $\Lambda_c^+ \to p\omega(\mu^+\mu^-)$ with respect to the normalization channel was measured in this analysis for Run2:

$$\frac{B(\Lambda_c^+ \to p\omega(\mu^+\mu^-))}{B(\Lambda_c^+ \to p\phi(\mu^+\mu^-))} = 0.222 \pm 0.031(stat.) \pm 0.015(syst)$$

The branching fraction of $\Lambda_c^+ \to p\omega$, was determined to be:

$$B(\Lambda_c^+ \to p\omega) = (9.08 \pm 1.26\ (stat) \pm 2.73\ (syst1) \pm 2.59\ (syst2)) \ \times 10^{-4}$$

For the first time the $\Lambda_c^+ \to p\rho(\mu^+\mu^-)$ was observed with the branching ratio close to the one for $\Lambda_c^+ \to p\omega(\mu^+\mu^-)$:

$$\frac{B(\Lambda_c^+ \to p\rho(\mu^+\mu^-))}{B(\Lambda_c^+ \to p\phi(\mu^+\mu^-))} = 0.203 \pm 0.052\ (stat) \pm 0.013\ (syst)$$

The corresponding branching fraction is determined to be:

$$B(\Lambda_c^+ \to p\rho) = (1.35 \pm 0.34\ (stat) \pm 0.44\ (syst1) \pm 0.22\ (syst2))\ \times 10^{-3}$$

A factor of five more collected data is expected from Run3 data which have been being collected since 2022. With more statistics one can explore the decay with more details including the analysis of angular distributions.

Appendices

A Trigger optimization

The procedure of the trigger optimization is described in Sec. 5.1.1. The efficiencies for individual years are listed in Tables 27, 28 and 29 for 2016, 2017 and 2018 respectively. The choice of common L0 and BDT1 lines for all years is straightforward. In the case of HLT2, the composition of the best lines is similar for 2017 and 2018. It turned out that although there were other high efficient lines for 2016, the choice of the same lines as for 2017/2018 did not reduce the total efficiency of the HLT2 step. The use of the same trigger configuration for all years makes the analysis more uniform and enables for common MVA training.

Table 27: The efficiencies of trigger lines with highest efficiencies for 2016. The efficiencies are measured on MC offline-like selected signal sample. The efficiency for a given line is determined independently of a decision of any other line. The relative efficiencies for HLT1 lines are normalized to the positive decisions of L0 lines selected for analysis. Similarly the relative efficiencies for HLT2 lines are normalized to positive decisions of L0 and HLT lines.

Trigger line	Efficiency [%] with respect to offline	Added [%] contribution
L0MuonDecision_TOS	58.75 ± 0.74	-
L0HadronDecision_TOS	62.51 ± 0.73	3.76
L0DiMuonDecision_TOS	64.99 ± 0.72	2.48
Trigger line	Efficiency [%] wrt offline & L0	Added contribution [%]
Hlt1TwoTrackMVADecision_TOS	91.05 ± 0.43	–
Hlt1TrackMVADecision_TOS	93.38 ± 0.38	2.33
Hlt1TrackMuonDecision_TOS	93.87 ± 0.36	0.49
Trigger line	Efficiency [%] wrt offline & L0 & Hlt1	Added contribution [%]
Hlt2RareCharmD2KMuMuOSDecision_TOS	34.99 ± 0.72	–
Hlt2ExoticaDisplDiMuonNoPointDecision_TOS	54.05 ± 0.75	19.06
Hlt2SingleMuonDecision_TOS	58.89 ± 0.74	4.84
Hlt2CharmHadInclSigc2PiLc2HHXBDTDecision_TOS	62.27 ± 0.73	3.38
Hlt2SingleMuonLowPTDecision_TOS	64.62 ± 0.72	2.35
Hlt2RareCharmD02KPiDecision_TOS	66.58 ± 0.71	1.96
Hlt2TopoMuMu2BodyDecision_TOS	68.15 ± 0.71	1.57
Hlt2XcMuXForTauB2XcMuDecision_TOS	69.06 ± 0.70	0.91
Hlt2CharmHadInclDst2PiD02HHXBDTDecision_TOS	69.84 ± 0.69	0.78
Hlt2RareCharmD2PiMuMuOSDecision_TOS	70.37 ± 0.69	0.53
Hlt2ExoticaDisplDiMuonDecision_TOS	70.89 ± 0.69	0.52
Hlt2EWSingleElectronLowPtDecision_TOS	71.15 ± 0.69	0.26

Table 28: The efficiencies of trigger lines with highest efficiencies for 2017.

Trigger line	Efficiency [%] wrt offline	Added [%] contribution
L0MuonDecision_TOS	70.33 ± 0.68	-
L0HadronDecision_TOS	75.16 ± 0.64	4.83
L0DiMuonDecision_TOS	76.71 ± 0.63	1.55
Trigger line	Efficiency [%] wrt offline & L0	Added contribution [%]
Hlt1TwoTrackMVADecision_TOS	91.23 ± 0.42	–
Hlt1TrackMVADecision_TOS	93.11 ± 0.38	1.88
Hlt1TrackMuonDecision_TOS	93.74 ± 0.36	0.63
Trigger line	Efficiency [%] wrt offline & L0 & Hlt1	Added contribution [%]
Hlt2RareCharmD2KMuMuOSDecision_TOS	84.92 ± 0.53	–
Hlt2RareCharmD2PiMuMuOSDecision_TOS	89.89 ± 0.45	4.97
Hlt2ExoticaDisplDiMuonDecision_TOS	94.47 ± 0.34	4.58
Hlt2SingleMuonLowPTDecision_TOS	95.61 ± 0.30	1.14
Hlt2ExoticaDisplDiMuonNoPointDecision_TOS	96.47 ± 0.27	0.86
Hlt2SingleMuonDecision_TOS	96.76 ± 0.55	0.26

Table 29: The efficiencies of trigger lines with highest efficiencies for 2018.

Trigger line	Efficiency [%] wrt offline	Added [%] contribution
L0MuonDecision_TOS	63.09 ± 0.72	-
L0HadronDecision_TOS	67.86 ± 0.70	4.77
L0DiMuonDecision_TOS	68.99 ± 0.69	1.13
Trigger line	Efficiency [%] wrt offline & L0	Added contribution [%]
Hlt1TwoTrackMVADecision_TOS	92.16 ± 0.40	–
Hlt1TrackMVADecision_TOS	93.60 ± 0.37	1.44
Hlt1TrackMuonDecision_TOS	94.22 ± 0.35	0.62
Trigger line	Efficiency [%] wrt offline & L0 & Hlt1	Added contribution [%]
Hlt2RareCharmD2KMuMuOSDecision_TOS	81.81 ± 0.58	–
Hlt2ExoticaDisplDiMuonDecision_TOS	88.17 ± 0.48	6.36
Hlt2RareCharmD2PiMuMuOSDecision_TOS	93.10 ± 0.38	4.93
Hlt2ExoticaDisplDiMuonNoPointDecision_TOS	95.18 ± 0.32	2.08
Hlt2SingleMuonLowPTDecision_TOS	95.95 ± 0.30	0.77
Hlt2TrackEffElectronDetachedMuKTurboCalibDecision_TOS	96.39 ± 0.28	0.44
Hlt2RareCharmD02KPiDecision_TOS	96.71 ± 0.27	0.32

B Hlt2 distortion of Λ_c^+ mass

The invariant mass distributions of Λ_c^+ candidates under the hypothesis of $K\mu^+\mu^-$ and $\pi\mu\mu$ are shown in Fig. 65. The $p\mu^+\mu^-$ invariant mass distributions of Λ_c^+ candidates for the preselected data for a positive decision of Hlt2RareCharmD2PiMuMuOS and Hlt2RareCharmD2KMuMuOS are shown in Fig. 66.

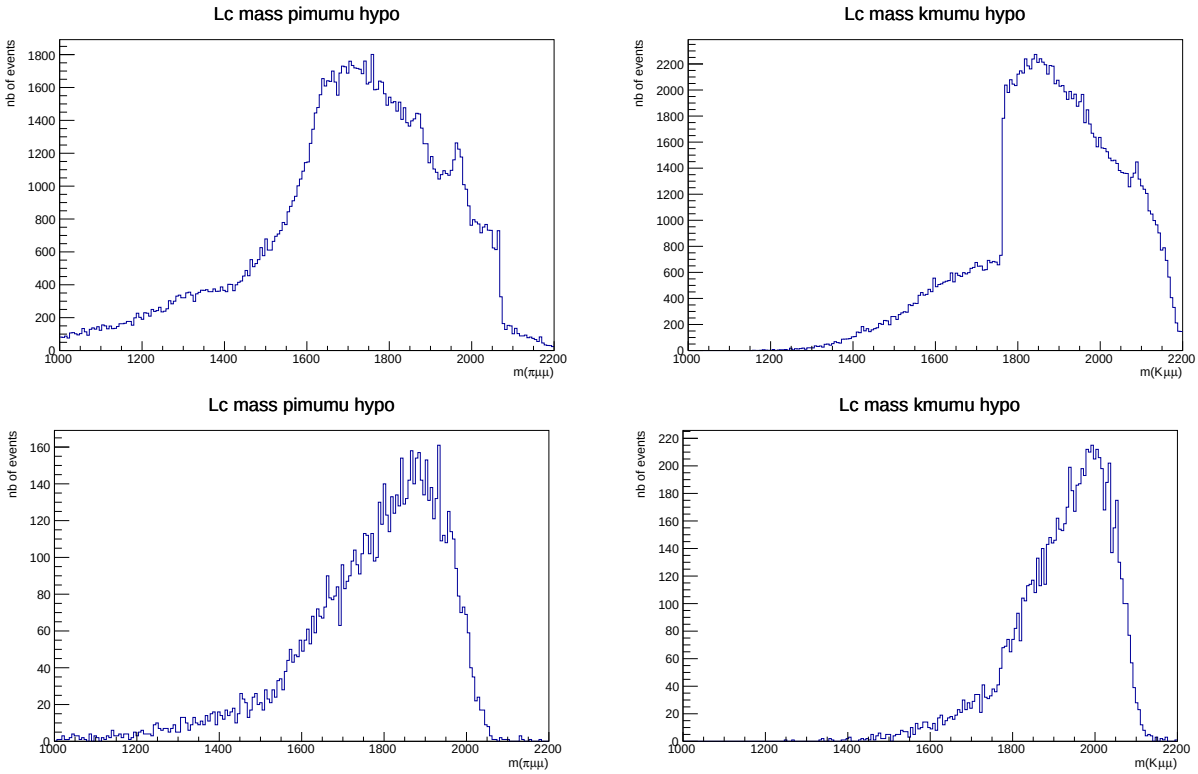

Figure 65: The invariant mass distributions of Λ_c^+ candidates under the hypothesis of $\pi\mu\mu$ (left) and $K\mu^+\mu^-$ (right) for data (top) and simulated signal (bottom). The figures are made for preselected samples.

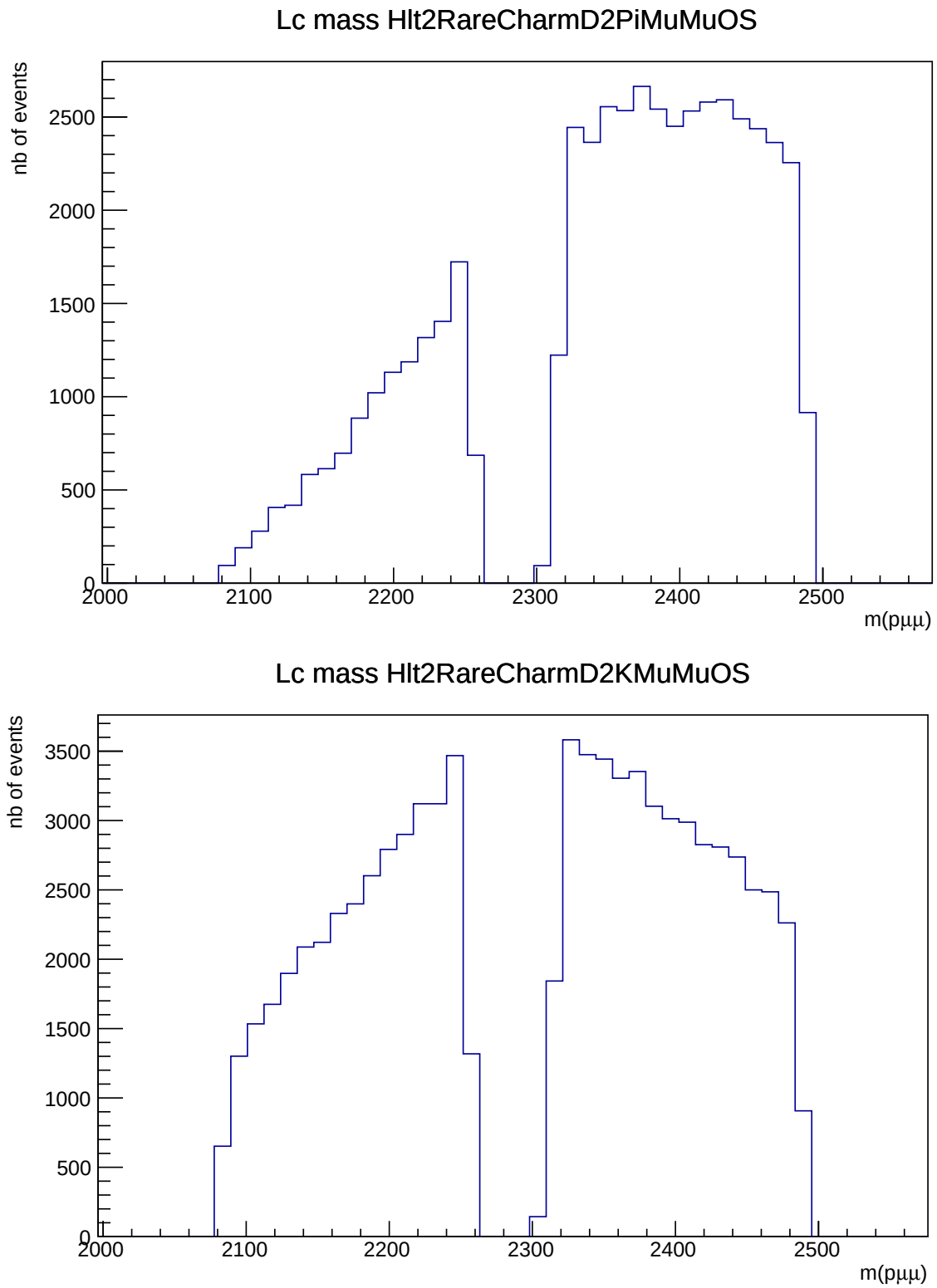

Figure 66: The $p\mu^+\mu_-$ invariant mass distributions of Λ_c^+ candidates for preselected data for positive decision of Hlt2RareCharmD2PiMuMuOS (top) and Hlt2RareCharmD2KMuMuOS (bottom).

C Prompt and secondary production

The generated MC samples consist of a mixture of prompt and secondary production $\Lambda_c^+ \to p\mu^+\mu^-$ according to the cross-sections for charm and beauty production. The rate of the secondary Λ_c^+ production is shown in Table 30 and Table 31 for the signal and normalization channel. At the generation stage, the rate is about 5%. Then the rate increases to above 24 % after the stripping where long lifetimes are preferred (large IP of secondaries without a strong requirement of Λ_c^+ to point to PV). A similar situation occurs in the trigger, where the secondary production amounts to 19%. Then the rate drops down to 3% after the final selection as BDT imposes Λ_c^+ to point to PV, thus removing the majority of Λ_c^+'s coming from b-hadron decays.

Table 30: The rate of secondary Λ_c^+ production at various analysis steps measured for signal MC sample.

	2016	2017	2018	Average
Generation	4.8%	4.27%	3.96%	4.34%
Stripping	25.35%	24.70%	22.63%	24.15%
Trigger	21.64%	18.92%	17.21%	18.98%
BDT + Prob	2.92%	3.08%	3.12%	3.05%

Table 31: The rate of secondary Λ_c^+ production at various analysis steps measured for MC sample of normalization channel.

	2016	2017	2018	Average
Generation	4.73%	4.13%	4.84%	4.57%
Stripping	25.03%	23.75%	23.76%	24.18%
Trigger	18.28%	15.57%	16.79%	16.88%
BDT + Prob	3.58%	3.36%	3.21%	3.38%

D BDT training

The distributions of fifteen variables used for BDT training are shown in Fig. 67.

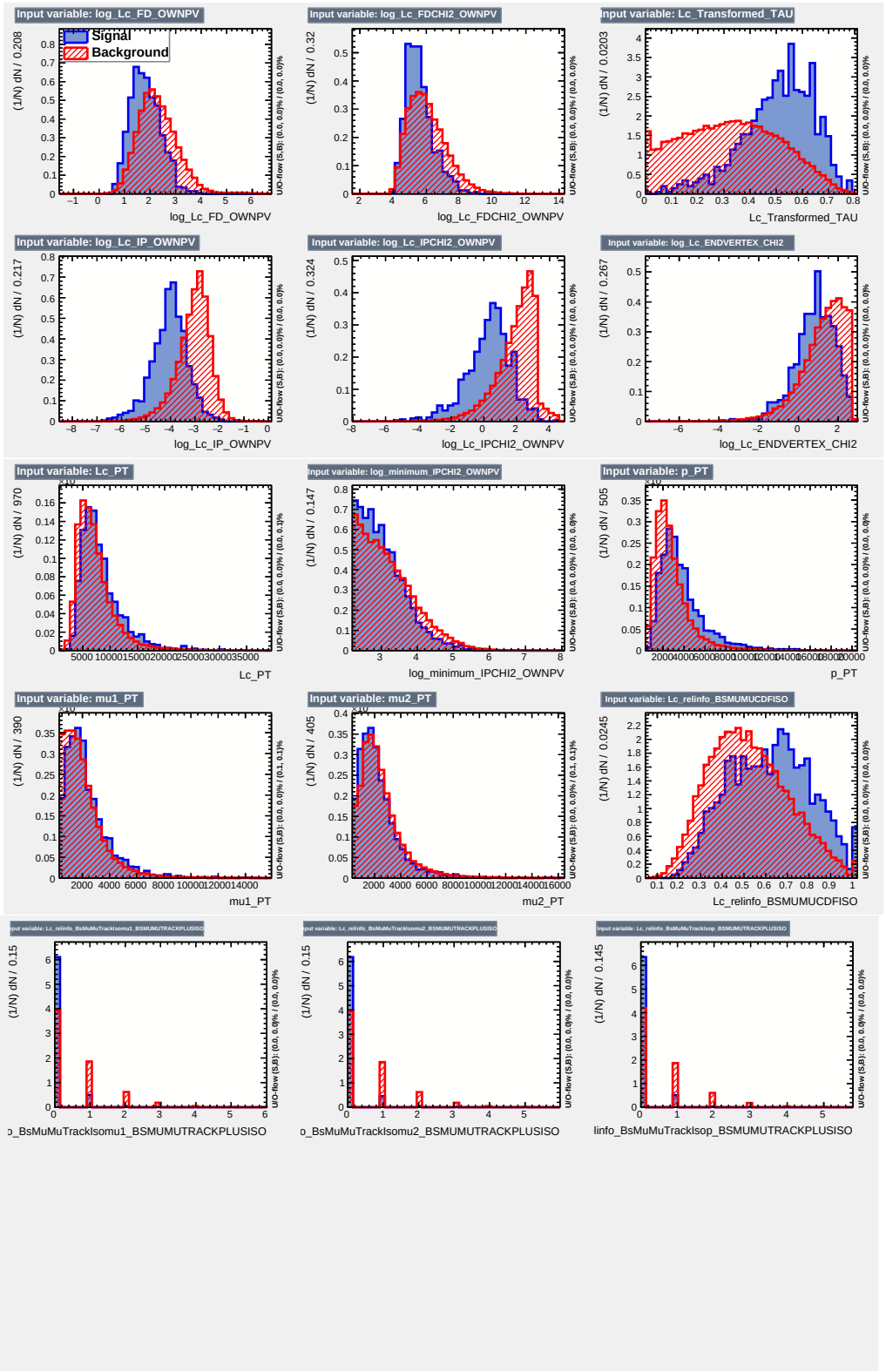

Figure 67: The distributions of BDT input variables for 2017 samples of signal prompt Λ_c^+ production (MC) and background (data sidebands).

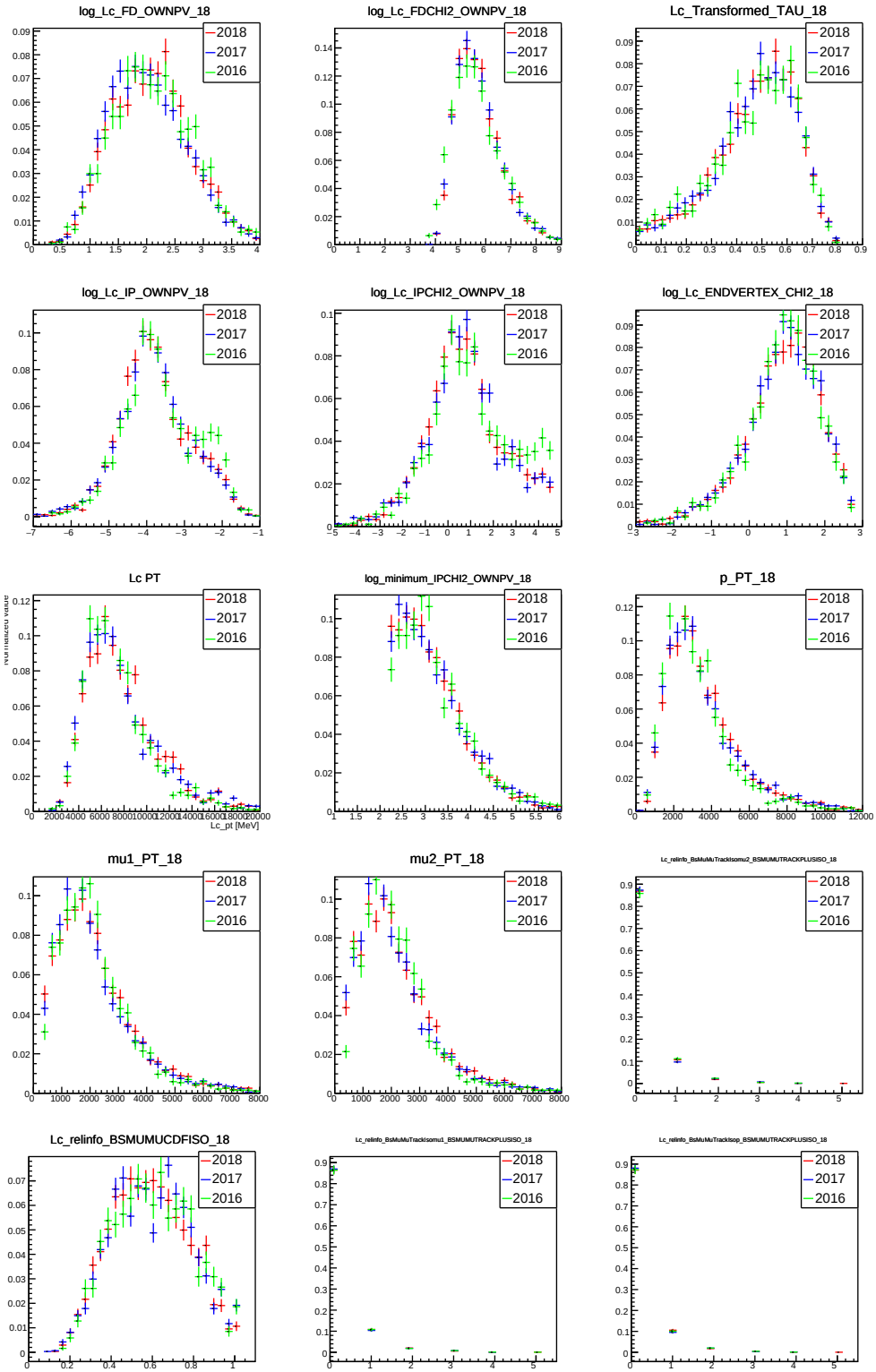

Figure 68: The comparison of distributions of BDT2 input variables for 2016, 2017 and 2018 samples for the MC signal after stripping and trigger.

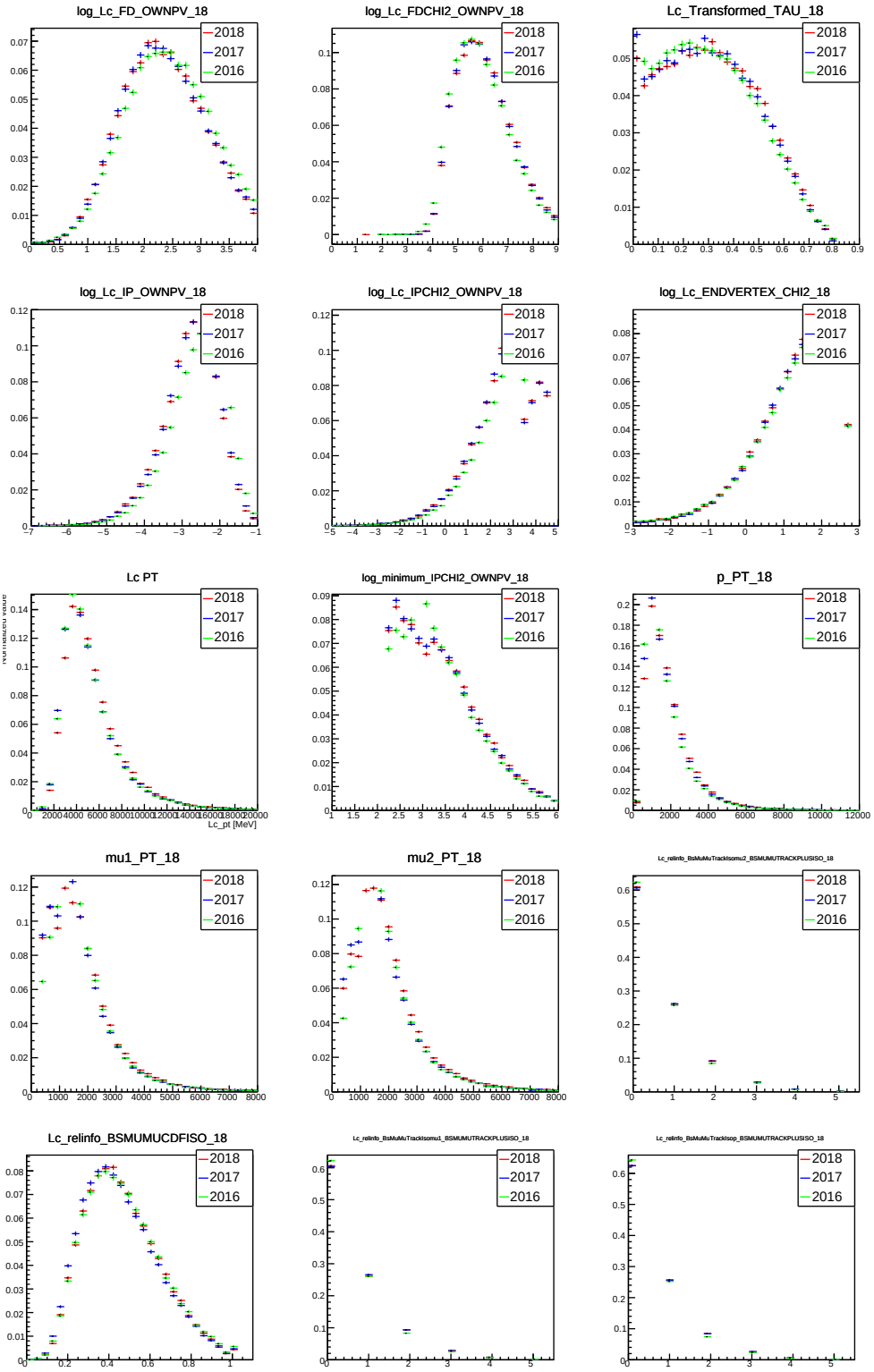

Figure 69: The comparison of distributions of BDT2 input variables for 2016, 2017 and 2018 samples for the data sidebands after stripping and trigger.

E Comparison between data and simulation

Some of the variables taken from the simulation does not match the data perfectly. As an effect, the corresponding distribution may differ. The MVA training should be maximally sensitive to real differences between the signal and background. For the training, the background is taken from the data sidebands and the signal from the simulation. Imperfect simulations may lead to suboptimal MVA training as the signal-background difference can be contaminated by differences between the simulation and data. Therefore, the simulation samples have to be reweighted to ensure satisfactory Data-MC agreement. An adaptive reweighting method has been applied. The comparison of variables used for BDT training after applying the reweighting is shown in Fig. 70. One can see that the agreement is satisfactory for all variables.

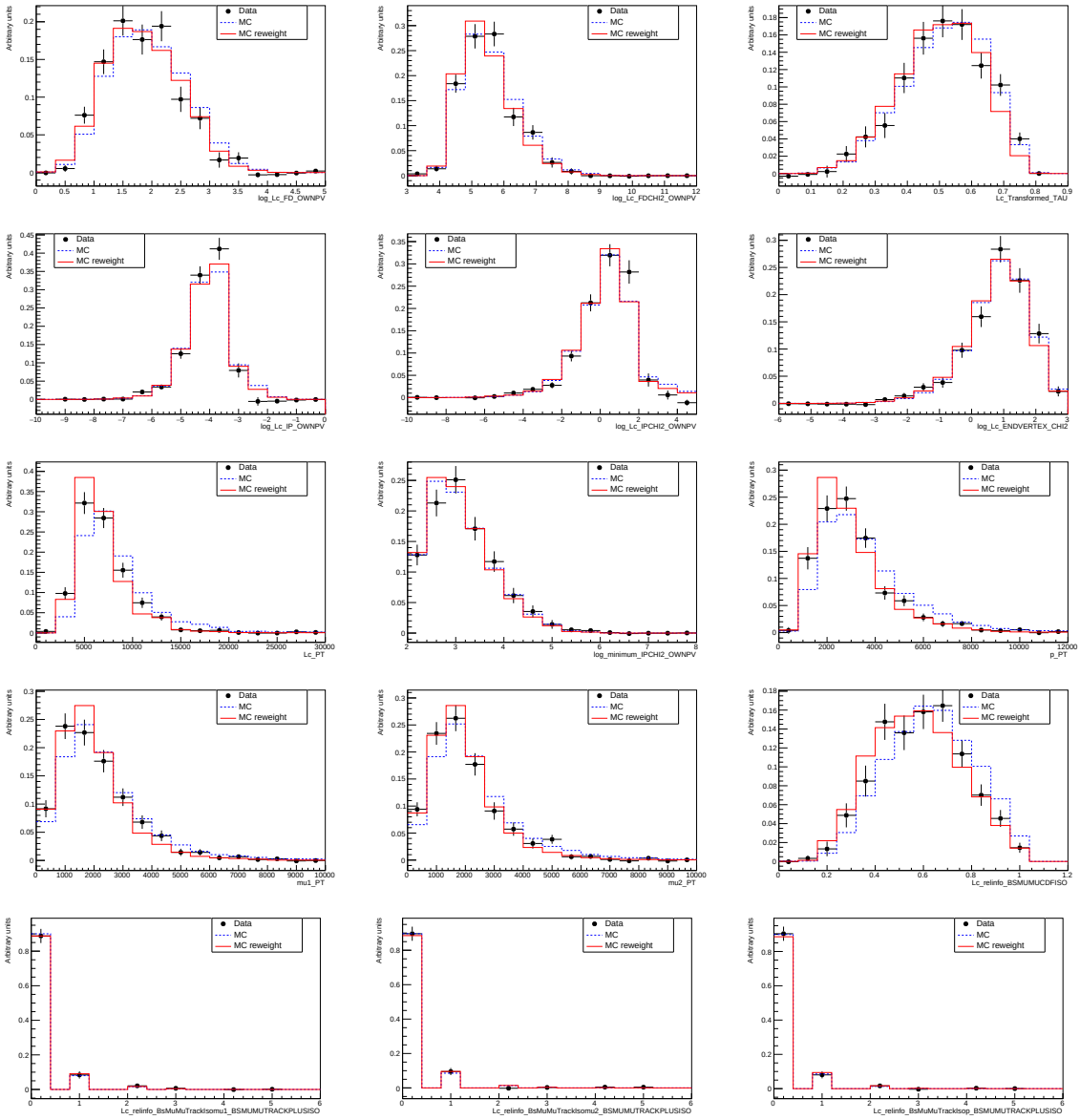

Figure 70: Comparison of distributions of BDT training variables for normalization channel between data (determined by sPlot technique) and simulation (MC reweighted by Adaptive reweighing method).

The effect of reweighting for various variables is expressed numerically in Table 32. The

table shows χ^2/ndf = $(\sum_{i=1}^{nb} \Delta_i^2/\sigma_i^2)/nb$ calculated for the histograms (Fig. 70) for data and MC before and after reweighting. One can see that most of the variables show improvement.

Table 32: The difference between histograms for data and MC before and after reweighting expressed as χ^2/ndf. The two first variables Lc_PT and nTracks are used for reweighting.

Variable	χ^2/ndf before reweighting	χ^2/ndf after reweighting
Lc_PT	4.91	1.26
nTracks	5.14	1.84
BDT2_response	5.26	1.12
p_PT	3.59	1.16
mu1_PT	1.53	1.00
mu2_PT	2.73	1.17
mu1_uniProbNNmu	1.54	0.92
mu2_uniProbNNmu	1.41	0.78
p_uniProbNNp	1.81	1.65
log_Lc_IP_OWNPV	3.34	2.62
log_Lc_IPCHI2_OWNPV	2.67	2.32
log_Lc_ENDVERTEX_CHI2	2.62	2.58
Lc_ETA	1.03	1.07
log_Lc_FD_OWNPV	2.66	2.26
log_Lc_FDCHI2_OWNPV	1.80	1.91
Lc_Transformed_TAU	1.17	1.71
log_minimum_IPCHI2_OWNPV	1.07	1.21
Lc_BSMUMUCDFISO	2.34	0.93
Lc_TrackIsomu1_BSMUMUTRACKPLUSISO	0.21	0.15
Lc_TrackIsomu2_BSMUMUTRACKPLUSISO	1.04	0.94
Lc_TrackIsop_BSMUMUTRACKPLUSISO	0.28	0.35

F Track isolation variable

The track isolation (TI) variable is constructed on the basis of the respective studies performed by the LHCb collaboration for the needs of the $B_s^0 \to \mu^+\mu^-$ analysis [93]. The TI is defined as the number of extra tracks (i.e. excluding the tracks that are attributed to the $\Lambda_c \to p\mu^+\mu^-$ candidate) that can form a vertex with a muon track. The assignment to the above SV is based on the selection criteria imposed on the following variables assuming signal track is a muon:

- minimum distance between the **track** and the PV (**pvdist**),
- minimum distance between the **track** and the $\Lambda_c \to p\mu^+\mu^-$ vertex (**svdist**),
- the distance of the closest approach between the **muon** and the **track** (DOCA),
- IP χ^2,
- angle between the **muon** and the **track** (β),
- the quantity

$$f_c = \frac{|\overrightarrow{p}_h + \overrightarrow{p}_{trk}|\alpha^{h+trk,PV}}{|\overrightarrow{p}_h + \overrightarrow{p}_{trk}|\alpha^{h+trk,PV} + p_{\mathrm{T},h} + p_{\mathrm{T},trk}}, \tag{13}$$

  where $\alpha^{h+trk,PV}$ is the angle between the **muon** and the **track** candidate, $P_{\mathrm{T},h}$ and $P_{\mathrm{T},trk}$ are the transverse momentum with respect to the beam line.

The track is considered as "isolated" if it satisfies the following requirements (imposed on the above mentioned variables):

- pvdist $\in [0.5, 40]$ mm,
- svdist $\in [-0.15, 30]$ mm,
- DOCA < 0.13 mm,
- Track IP significance > 3,
- $\beta < 0.27$ rad,
- $f_c < 0.6$.

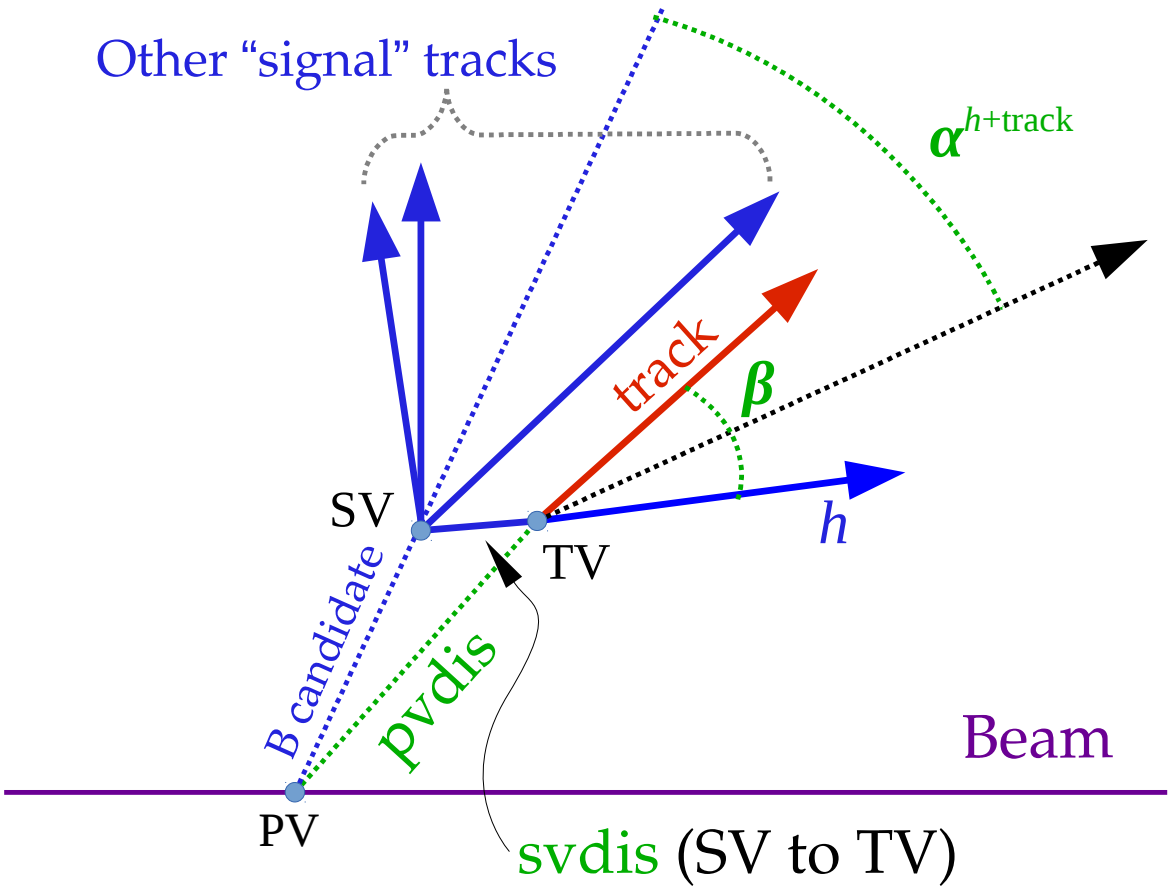

Figure 71: Diagram showing the variables used in the track isolation variable. The description of the variables marked in the plot is provided in the text.

G Additional information on efficiencies

G.1 Differential efficiencies

The relative efficiencies are presented in Fig. 72. It can be seen that the efficiency trigger&stripping/generation shows an increase for dimuon invariant around the ϕ mass. The efficiency selection/trigger&stripping is relatively flat. In the case of R^{COMM} the deviation from the unity is caused by BDT discrimination which favors kinematics of $\Lambda_c \to p\mu^+\mu^-$. The same behavior can be observed for the total efficiency dependence on dimuon invariant mass shown in Fig. 73.

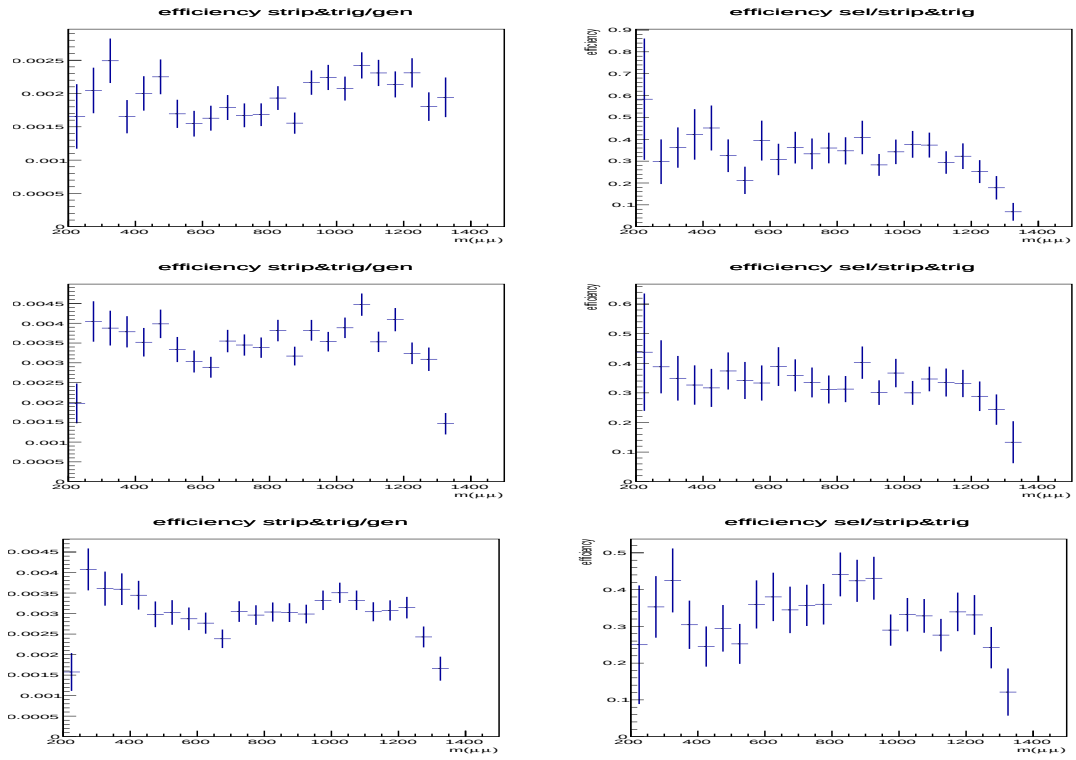

Figure 72: The relative efficiencies as function of dimuon invariant mass: trigger&stripping/generation (left) and selection/trigger&stripping (right) for 2016 (top), 2017 (middle) and 2018 (bottom).

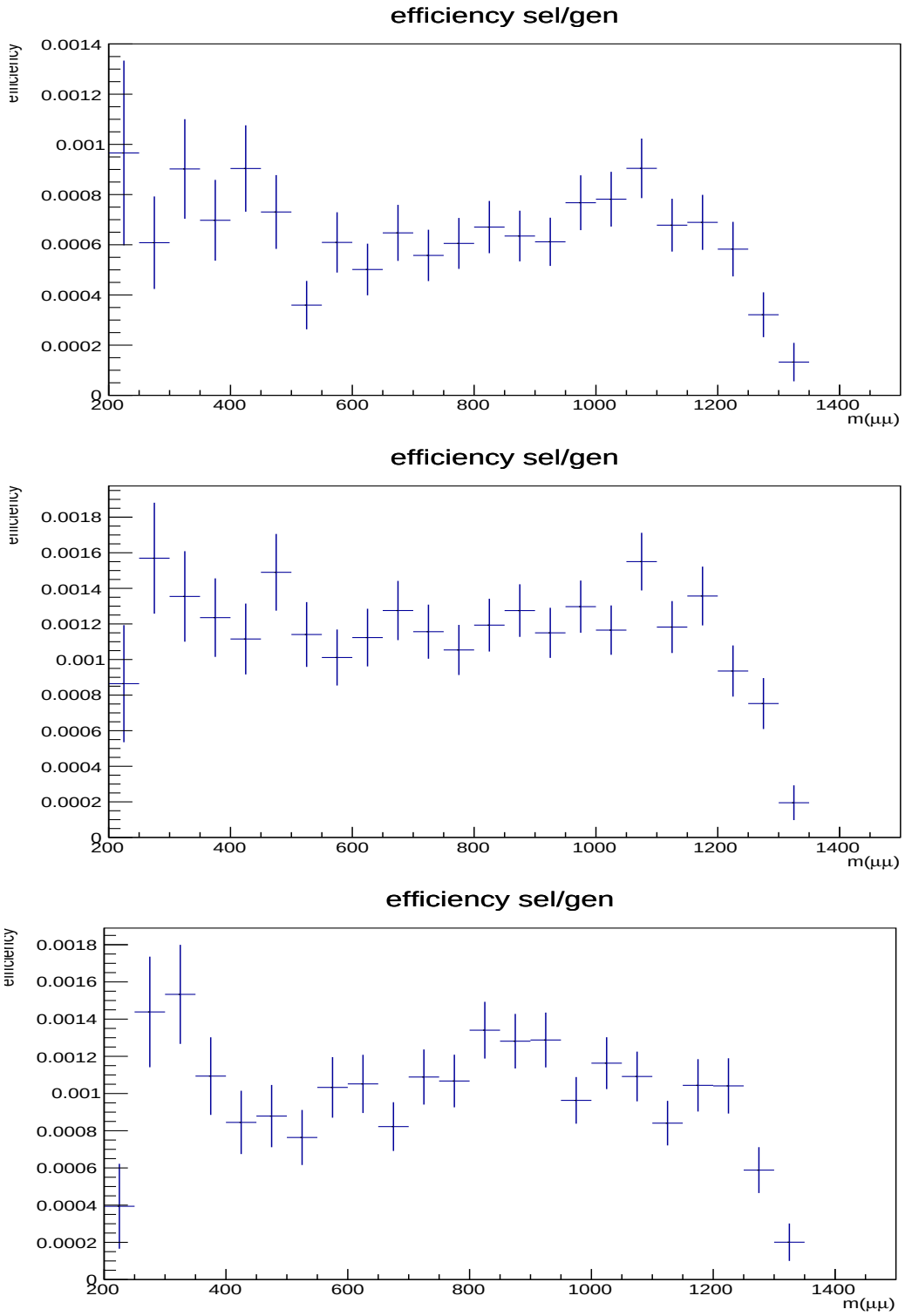

Figure 73: The relative efficiency as function of dimuon invariant mass: selection/generation.

G.2 Efficiencies and yields

The efficiencies for the normalization and for signal channels for individual year are listed in Table 33. The ratios of the efficiencies are listed in the last column of the table.

Table 33: The efficiencies (number of selected events divided by number of events in MC sample) of the normalization and signal channels and their ratios for individual years. Uncertainties for efficiency are statistical only without any correction. Last column gives the yields of normalization channel where the numbers for 2016 and 2017 are normalized to the 2018 luminosity to enable direct comparison.

year	efficiency [%] normalization	efficiency [%] signal	ratio norm/signal	yield of normalization
2016	0.0677 ± 0.0026	0.0237 ± 0.0015	2.8572 ± 0.2151	144.2 ± 15.2
2017	0.0815 ± 0.0028	0.0348 ± 0.0019	2.3444 ± 0.1497	173.3 ± 14.7
2018	0.0758 ± 0.0027	0.0314 ± 0.0018	2.4129 ± 0.1615	175.6 ± 13.8

The number of combinatorial background estimated from the fit to the sidebands and extrapolated to the full mass range (2140, 2430) MeV/c^2 is listed in Table 34.

Table 34: The number of combinatorial events selected from data for individual years.

year	nb of events	nb of events normalized to 2018
2016	171.1 ± 15.1	224.5 ± 19.8
2017	229.8 ± 17.5	283.9 ± 21.6
2018	297.0 ± 19.9	297.0 ± 19.9

H Cross-check of π to μ misidentification

The contribution of $\Lambda_c^+ \to p\pi^+\pi^-$ background to the signal is estimated in Sec. 7.4. After unblinding this contribution will be determined in the fit to invariant mass distribution of Λ_c^+ candidates. To ensure before unblinding that the rate of π to μ misidentification is consistent with the data, the cross check of the contribution to normalization channel is performed. The yield of $\Lambda_c^+ \to p\pi^+\pi^-$ contribution to the normalization channel is estimated using the method described in Sec. 7.5. This estimation can be compared with the results of the fit described in Sec. 10.2. The results of such a comparison for final selection and for the selection excluding BDT2 cut are shown in Fig. 74 and in Table 35. The estimated and fitted values are compatible although the uncertainty of the fitted values is large.

Table 35: The comparison of contribution of $\Lambda_c^+ \to p\pi^+\pi^-$ background to normalization channel for full selection and selection without BDT2 cut and without ProbNNmu cut (isMuon=1 only).

Selection	estimated	fitted
full	6.4 ± 1.1	11.5 ± 10.2
No BDT2 cut	9.3 ± 1.6	58.0 ± 23.5
No ProbNNmu cut	59.2 ± 10.1	44.3 ± 14.4

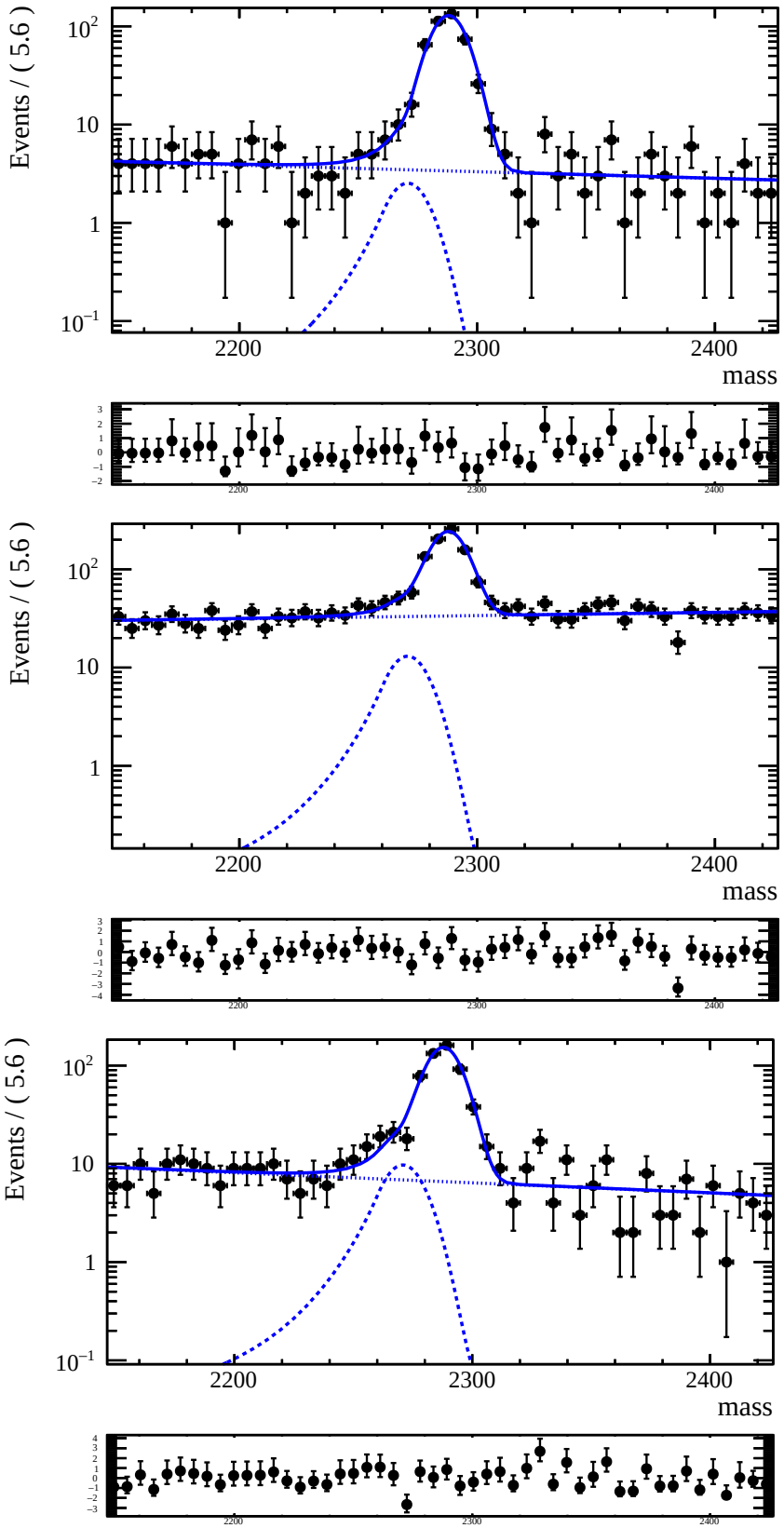

Figure 74: The results of the fit to Λ_c^+ invariant mass for normalization channel after selection (left), after selection without BDT2 cut (middle), after selection without ProbNNmu cut (right).

Bibliography

[1] Sheldon L. Glashow. Partial-symmetries of weak interactions. *Nuclear Physics*, 22(4):579–588, 1961.

[2] A. Salam and J.C. Ward. Electromagnetic and weak interactions. *Physics Letters*, 13(2):168–171, 1964.

[3] Steven Weinberg. A Model of Leptons. *Phys. Rev. Lett.*, 19:1264–1266, Nov 1967.

[4] G. Aad, et al. Observation of a new particle in the search for the Standard Model Higgs boson with the ATLAS detector at the LHC. *Physics Letters B*, 716(1):1–29, sep 2012.

[5] S. Chatrchyan, et al. Observation of a new boson at a mass of 125 GeV with the CMS experiment at the LHC. *Physics Letters B*, 716(1):30–61, sep 2012.

[6] Lyndon Evans and Philip Bryant. LHC Machine. *Journal of Instrumentation*, 3(08):S08001, aug 2008.

[7] Stephen J. Blundell. Magnetism: A Very Short Introduction. *Oxford University Press*, 06 2012.

[8] John D. Jackson. Classical Electrodynamics Third Edition. *New York: John Wiley & Sons*, 1999.

[9] The Nobel Foundation. The Nobel Prize in Physics 1979. `https://www.nobelprize.org/prizes/physics/1979/summary/`.

[10] David J Griffiths. Introduction to elementary particles; 2nd rev. version. *Wiley*, 2008.

[11] Peter W. Higgs. Broken Symmetries and the Masses of Gauge Bosons. *Phys. Rev. Lett.*, 13:508–509, Oct 1964.

[12] Peter Ware Higgs. Broken symmetries, massless particles and gauge fields. *Phys. Lett.*, 12:132–133, 1964.

[13] Steven Weinberg. The Quantum Theory of Fields. *Cambridge University Press*, 1995.

[14] Paul Langacker. The Standard Model and Beyond. *CRC Press*, 2017.

[15] Ian J. R. Aitchison and Anthony J. G. Hey. Gauge Theories in Particle Physics: A Practical Introduction. *Institute of Physics*, 2003.

[16] Takaaki Kajita. Discovery of Atmospheric Neutrino Oscillations, 2015.

[17] Rabindra N. Mohapatra and Goran Senjanović. Neutrino masses and mixings in gauge models with spontaneous parity violation. *Phys. Rev. D*, 23:165–180, Jan 1981.

[18] Andrei D Sakharov. Violation of CP invariance, C asymmetry, and baryon asymmetry of the universe. *Soviet Physics Uspekhi*, 34(5):392, may 1991.

[19] David J. Gross and Frank Wilczek. Ultraviolet Behavior of Non-Abelian Gauge Theories. *Phys. Rev. Lett.*, 30:1343–1346, Jun 1973.

[20] Edward V. Shuryak. Quantum chromodynamics and the theory of superdense matter. *Physics Reports*, 61(2):71–158, 1980.

[21] Lochlain O'Raifeartaigh and Norbert Straumann. Early History of Gauge Theories and Kaluza-Klein Theories, with a Glance at Recent Developments, 1999.

[22] Gavin P. Salam. Elements of QCD for hadron colliders, 2011. url-https://arxiv.org/abs/1011.5131.

[23] Nicola Cabibbo. Unitary Symmetry and Leptonic Decays. *Phys. Rev. Lett. 10, 531*, 1963.

[24] Makoto Kobayashi and Toshihide Maskawa. Progress of Theoretical Physics. *Prog. Theor. Phys. 49, 652*, 1973.

[25] Lincoln Wolfenstein. Parametrization of the Kobayashi-Maskawa Matrix. *Phys. Rev. Lett. 51, 1945*, 1983.

[26] Particle Data Group. Review of Particle Physics CKM Quark-Mixing Matrix. *PTEP*, 2022:083C01, 2022.

[27] S. L. Glashow, J. Iliopoulos, and L. Maiani. Weak Interactions with Lepton-Hadron Symmetry. *Phys. Rev. D*, 2:1285–1292, Oct 1970.

[28] J. J. Aubert, et al. Experimental Observation of a Heavy Particle J. *Phys. Rev. Lett.*, 33:1404–1406, Dec 1974.

[29] J. E. Augustin, et al. Discovery of a Narrow Resonance in e^+e^- Annihilation. *Phys. Rev. Lett.*, 33:1406–1408, Dec 1974.

[30] Martinus Veltman. Diagrammatica: The Path to Feynman Diagrams. *Cambridge University Press*, 1994.

[31] V. D. Hopper and S. Biswas. Evidence Concerning the Existence of the New Unstable Elementary Neutral Particle. *Phys. Rev.*, 80:1099–1100, Dec 1950.

[32] Particle Data Group. Review of Particle Physics Baryons. *PTEP*, 2022:083C01, 2022.

[33] Gustavo Burdman, Eugene Golowich, JoAnne Hewett, and Sandip Pakvasa. Rare charm decays in the standard model and beyond. *Phys. Rev. D*, 66:014009, Jul 2002.

[34] S. Fajfer., S. Prelovsek, and P. Singer. Rare charm meson decays $D \to Pl^+l^-$ and $c \to ul^+l^-$ in the standard model and the minimal supersymmetric standard model. *Phys. Rev.*, D64:114009, 2001.

[35] Marcel Golz, Gudrun Hiller, and Tom Magorsch. Probing for New Physics with Rare Charm Baryon (Λ_c, Ξ_c, Ω_c) Decays, 2021.

[36] R. Aaij et al. Angular analysis of the $B^+ \to K^{*+}\mu^+\mu^-$ decay. *Phys. Rev. Lett.*, 126:161802, 2021.

[37] BABAR Collaboration. Searches for rare or forbidden semileptonic charm decays. *Phys. Rev. D*, 84:072006, Oct 2011.

[38] R. Aaij, et al. Search for the rare decay $\Lambda_c^+ \to p\mu^+\mu^-$. *Phys. Rev. D*, 97:091101, May 2018.

[39] Cern research center. `http://www.cern.ch`, Access:11-05-2023.

[40] Peter M. Watkins. Discovery of the W and Z bosons. *Contemp. Phys. 27.* (1986) 291–324.

[41] Tim Berners-Lee, World Wide Web inventor. https://cds.cern.ch/record/39437/.

[42] Brüning Oliver Sim et al. LHC Design Report. 2004. http://cds.cern.ch/record/782076.

[43] Stephen Myers. The LEP Collider, from design to approval and commissioning. *CERN*, 1991. Delivered at CERN, 26 Nov 1990.

[44] The CERN accelerator complex, layout in 2022. https://cds.cern.ch/record/39437/.

[45] The Linac 4. `https://home.cern/science/accelerators/linear-accelerator-4`, Access:11-05-2023.

[46] The Proton Synchrotron Booster. `https://home.cern/science/accelerators/proton-synchrotron-booster`, Access:11-05-2023.

[47] Accelerator upgrades during LS2. `https://home.cern/press/2022/accelerator-upgrades-during-ls2`.

[48] The ALICE Collaboration et al. The ALICE experiment at the CERN LHC. *JINST 3 S08002*, 2008.

[49] The ATLAS Collaboration et al. The ATLAS Experiment at the CERN Large Hadron Collider. *JINST 3 S08003*, 2008.

[50] The CMS Collaboration et al. The CMS experiment at the CERN LHC. *JINST 3 S08004*, 2008.

[51] The LHCb Collaboration et al. The LHCb Detector at the LHC. *JINST 3 S08005*, 2008.

[52] ATLAS Collaboration et al. Observation of a new particle in the search for the Standard Model Higgs boson with the ATLAS detector at the LHC. *Physics Letters B*, 716(1):1–29, 2012.

[53] CMS Collaboration et al. Observation of a new boson at a mass of 125 GeV with the CMS experiment at the LHC. *Physics Letters B*, 716(1):30–61, 2012.

[54] The TOTEM Collaboration, et al. The TOTEM Experiment at the CERN Large Hadron Collider. *Journal of Instrumentation*, 3(08):S08007, aug 2008.

[55] The LHCf Collaboration, et al. The LHCf detector at the CERN Large Hadron Collider. *Journal of Instrumentation*, 3(08):S08006, aug 2008.

[56] B. Acharya, et al. The physics programme of the MoEDAL experiment at the LHC. *International Journal of Modern Physics A*, 29(23):1430050, 2014.

[57] First Results from the Search for Dark Photons with the FASER Detector at the LHC. Technical report, CERN, Geneva, 2023.

[58] SND@LHC: The Scattering and Neutrino Detector at the LHC. Technical report, CERN, Geneva, 2022.

[59] LHCb Collaboration et al. LHCb magnet : Technical Design Report. 2000. CERN-LHCC-2000-007 ; LHCb-TDR-1.

[60] LHCb Collaboration et al. LHCb VELO (VErtex LOcator) : Technical Design Report. 2001. CERN-LHCC-2001-011 ; LHCb-TDR-5.

[61] LHCb Collaboration et al. LHCb inner tracker : Technical Design Report. 2002. CERN-LHCC-2002-029 ; LHCb-TDR-8.

[62] LHCb Collaboration et al. LHCb outer tracker : Technical Design Report. 2001. CERN-LHCC-2001-024 ; LHCb-TDR-6.

[63] Marian Stahl. Machine learning and parallelism in the reconstruction of LHCb and its upgrade. *Journal of Physics: Conference Series*, 898, 10 2017.

[64] LHCb Collaboration et al. LHCb RICH : Technical Design Report. 2000. CERN-LHCC-2000-037 ; LHCb-TDR-3.

[65] P. A. Čerenkov. Visible Radiation Produced by Electrons Moving in a Medium with Velocities Exceeding that of Light. *Phys. Rev.*, 52:378–379, Aug 1937.

[66] LHCb Collaboration et al. LHCb calorimeters : Technical Design Report. 2000. CERN-LHCC-2000-036 ; LHCb-TDR-2.

[67] LHCb Collaboration et al. LHCb muon system : Technical Design Report. 2001. CERN-LHCC-2001-010 ; LHCb-TDR-4.

[68] A A Alves et al. Performance of the LHCb muon system. *Journal of Instrumentation*, 8(02):P02022–P02022, feb 2013.

[69] Denis Derkach, Mikhail Hushchyn, and Nikita Kazeev. Machine Learning based Global Particle Identification Algorithms at the LHCb Experiment. *EPJ Web of Conferences*, 214:06011, 01 2019.

[70] LHCb Collaboration et al. LHCb detector performance. *International Journal of Modern Physics A*, 30(07):1530022, mar 2015.

[71] LHCb collaboration. Trigger schemes, 2022. `http://lhcb.web.cern.ch/lhcb/speakersbureau/html/TriggerScheme.html`.

[72] LHCb collaboration. Design and performance of the LHCb trigger and full real-time reconstruction in Run 2 of the LHC. *Journal of Instrumentation*, 14(04):P04013–P04013, apr 2019.

[73] R. Frühwirth. Application of Kalman filtering to track and vertex fitting. *Nuclear Instruments and Methods in Physics Research Section A: Accelerators, Spectrometers, Detectors and Associated Equipment*, 262(2):444–450, 1987.

[74] M Clemencic ed al. The LHCb Simulation Application, Gauss: Design, Evolution and Experience. *J. Phys.: Conf. Ser. 331 032023*, 2011.

[75] The BRUNEL Project. `http://lhcbdoc.web.cern.ch/lhcbdoc/brunel/`.

[76] The Worldwide LHC Computing Grid. `https://www.home.cern/science/computing/grid`.

[77] The DAVINCI Project. `http://lhcbdoc.web.cern.ch/lhcbdoc/davinci/`.

[78] LHCbDIRAC Documentation. `https://lhcb-dirac.readthedocs.io/en/latest/`.

[79] Root. https://root.cern/about/ 2022.

[80] The LHCb Collaboration, CERN. Upgrade Software and Computing. Technical report, Geneva, 2018.

[81] Torbjörn Sjöstrand, Stephen Mrenna, and Peter Skands. PYTHIA 6.4 physics and manual. *Journal of High Energy Physics*, 2006(05):026–026, may 2006.

[82] David J. Lange. The EvtGen particle decay simulation package. *Nuclear Instruments and Methods in Physics Research Section A: Accelerators, Spectrometers, Detectors and Associated Equipment*, 462(1):152–155, 2001. BEAUTY2000, Proceedings of the 7th Int. Conf. on B-Physics at Hadron Machines.

[83] S. Agostinelli ed al. Geant4—a simulation toolkit. *Nuclear Instruments and Methods in Physics Research Section A: Accelerators, Spectrometers, Detectors and Associated Equipment*, 506(3):250–303, 2003.

[84] The BOOLE Project. http://lhcbdoc.web.cern.ch/lhcbdoc/boole/ 2022.

[85] Lucio Anderlini et al. The PIDCalib package. Technical report, CERN, Geneva, 2016.

[86] Gammacombo. https://gammacombo.github.io/ 2022.

[87] R. L. Workman et al. Review of particle physics. *Prog. Theor. Exp. Phys.*, 2022(8):083C01, 2022.

[88] Andreas Hoecker, Peter Speckmayer, Joerg Stelzer, Jan Therhaag, Eckhard von Toerne, and Helge Voss. TMVA: Toolkit for Multivariate Data Analysis. *PoS*, ACAT:040, 2007.

[89] Avrim Blum, Adam Kalai, and John Langford. Beating the Hold-Out: Bounds for K-fold and Progressive Cross-Validation. *COLT '99 Proceedings of the twelfth annual conference on Computational learning theory*, pages 203–208, 1999.

[90] A. Abulencia, et al. Search for $B_s^0 \to \mu^+\mu^-$ and $B_d^0 \to \mu^+\mu^-$ Decays in $p\overline{p}$ Collisions with CDF II. *Physical Review Letters*, 95(22), nov 2005.

[91] M. Pivk and F.R. Le Diberder. A statistical tool to unfold data distributions. *Nuclear Instruments and Methods in Physics Research Section A: Accelerators, Spectrometers, Detectors and Associated Equipment*, 555(1-2):356–369, dec 2005.

[92] R. Aaij et al. A measurement of the CP asymmetry difference in $\Lambda_c^+ \to pK^-K^+$ and $p\pi^-\pi^+$ decays. *JHEP*, 03:182, 2018.

[93] R Aaij et al. First Evidence for the Decay $B_s^0 \to \mu^+\mu^-$. *Phys. Rev. Lett.*, 110:021801, 2013.

[94] Andrzej J. Buras, Markus E. Lautenbacher, and Gaby Ostermaier. Waiting for the top quark mass, $K^+ \to \pi^+ vv^-, B_s^0 - B_s^{-0}$ mixing, and CP asymmetries in B decays. *Phys. Rev. D*, 50:3433–3446, Sep 1994.

[95] J. Charles, A. Höcker, H. Lacker, S. Laplace, F. R. Le Diberder, J. Malclés, J. Ocariz, M. Pivk, and L. Roos. CP violation and the CKM matrix: assessing the impact of the asymmetric B factories. *The European Physical Journal C*, 41(1):1–131, May 2005.

[96] CDF collaboration T. Aaltonen et al. High-precision measurement of the W boson mass with the CDF II detector. *Science*, 376(6589):170–176, 2022.

[97] LHCb collaboration. Test of lepton universality in beauty-quark decays. *Nature Physics*, 18(3):277–282, Mar 2022.

[98] S. Fajfer, A. Prapotnik, S. Prelovšek, P. Singer, and J. Zupan. The rare decays of D mesons. *Nuclear Physics B - Proceedings Supplements*, 115:93–97, 2003. Hyperons, Charm and Beauty Hadrons.

[99] Bernat Capdevila, Andreas Crivellin, Sébastien Descotes-Genon, Joaquim Matias, and Javier Virto. Patterns of New Physics in $b \to sl^+l^-$ transitions in the light of recent data. *Journal of High Energy Physics*, 2018(1), Jan 2018.

[100] LHCb Collaboration et al. Measurement of the b-Quark Production Cross Section in 7 and 13 TeV pp Collisions. *Phys. Rev. Lett.*, 118:052002, Feb 2017.

[101] LHCb Collaboration et al. Measurements of prompt charm production cross-sections in pp collisions at $\sqrt{s}$=13 TeV. *J. High Energ. Phys. 2016, 159*, 2016.